Towards nuclear imaging with polynuclear radiotracers: the development of monomeric and dendritic scaffolds for radiometals

by

Siphelele Malaza

A dissertation submitted as part of the requirements for the

M.Sc. degree in Chemistry

University of Cape Town, Department of Chemistry, December 2015

Supervisor: Associate Professor Gregory Smith

Co-supervisor: Associate Professor Hendrik G. Visser

Acknowledgements

I would like to thank the Nuclear Technologies in Medicine and the Biosciences Initiative (NTeMBI), South African Nuclear Energy Corporation (Necsa p1600, Pretoria), the Carnegie scholarship for women in science and engineering, Cyclotron Réunion Océan Indien (CYROI, Réunion Island), the University of the Free State (Bloemfontein), the University of Cape Town chemistry department, and my supervisor Assoc. Prof. Gregory Smith, for making this project a success.

To the Malaza family, once again Mom, Dad, Nhlo, S'ne and Andile, I thank you for the love and support you have afforded me throughout my education. I will continue to make you proud.

Declaration

I declare that, "**Towards nuclear imaging with polynuclear radiotracers: the development of monomeric and dendritic scaffolds for radiometals**" is my own work and to the best of my knowledge has never been reported or submitted for any degree or examination in any university. All sources of information used are cited, acknowledged and completely referenced at the end of each chapter.

Signed by candidate

Siphelele Malaza

09/11/2015

Date

Table of contents

Table of Contents

Table of Contents

Table of Contents

Chapter 4

Substitution kinetic investigations

Chapter 5

Technetium-99m and gallium-68 radiolabeling studies

Abstract

A series of 1,4-diaminobutane poly(propylene amine) (DAB-PPI) dendrimer-based ligands were prepared with the aim of developing ligands that will permit the synthesis of multinuclear technetium-99m (^{99m}Tc) radiolabeled complexes. The ligands were synthesized by incorporating *N,N*-donor atom functionalities, at the periphery of DAB-PPI dendrimers, as potential ^{99m}Tc chelates. Monomeric ligands were also synthesized as model compounds to aid with the characterization of macromolecular structures.

The first (DAB-G1dendr-$(NH_2)_4$) and second (DAB-G2dendr-$(NH_2)_8$) generation DAB-PPI peripheral amine end-groups were functionalized using appropriate aldehydes, bearing either 2,2'-bipyridyl or 2-picolylamino entities, *via* a single step reductive amination reaction. The monomeric and new dendritic ligands were comprehensively characterized using spectroscopic (^{1}H NMR, ^{13}C{^{1}H} NMR, infrared) and analytical techniques (mass spectrometry and elemental analysis). Furthermore, the 2-picolylamino-functionalized ligands were found to be water-soluble, $\boldsymbol{S_{25\,°C}}$ = 0.01 mg/µL.

A series of non-radioactive ('cold') neutral mononuclear and novel multinuclear dendritic rhenium(I) complexes of the form *fac*-[$Re_n(CO)_3$(*N,N*-bidentate)X_n] (n = 1, 4 and 8 for monomer, G1 and G2, respectively. X = Cl^- or Br^-) were prepared and characterized. The complexes with the *fac*-[$Re(CO)_3Br$] core were synthesized at room temperature using the $(Et_4N)[Re(CO)_3Br_3]$. One of the 2-picolylamino monomeric complexes, *fac*-[$Re(CO)_3$(*N,N*-bidentate)Br], was additionally characterized by X-ray crystallography and the crystallographic structure confirms the *facial* arrangement of the three CO ligands together with the *pseudo* octahedral geometry around the metal centre.

Abstract

The *fac*-$[Re(CO)_3(OH_2)_3]^+$ precursor was used to synthesize a range of cationic monomeric and new multivalent dendritic complexes of the type *fac*-$[Re_n(CO)_3(N,N\text{-bidentate})OH_2]^{n+}$ (n = 1, 4 and 8 for monomer, G1 and G2, respectively) as ^{99m}Tc surrogates. The Re(I)-aqua complexes were characterized by spectroscopic and analytical methods.

In order to evaluate the stability and reactivity of the known labile aqua ligand in *fac*-$[Re_n(CO)_3(N,N\text{-bidentate})OH_2]^{n+}$ (n = 1, 4 and 8 for monomer, G1 and G2, respectively) systems, the 2-picolylamino complexes with the *fac*-$[Re(CO)_3OH_2]^+$ core were dissolved in methanol and the substitution of the water/methanol ligand at the sixth coordination site by a range of neutral and cationic monodentate ligands was monitored by stopped-flow spectrophotometry. The dendritic *fac*-$[Re_n(CO)_3(N,N\text{-bidentate})MeOH]^{n+}$ (n = 4 and 8 for G1 and G2, respectively) complexes, containing more than one Re(I) metal centre, were found to labilise the *fac*-$[Re(CO)_3MeOH]^+$ core effectively than the monomeric analogue. This was supported by an increase in forward second-order rate constants (k_n) obtained for the substitution of MeOH, by monodentate nucleophiles at 25.0 ˚C, in the dendritic complexes compared to the monomeric analogue.

The water-soluble first generation 2-picolylamino DAB-PPI dendritic ligand was radiolabeled with generator-eluted radioactive sodium pertechnetate ($Na^{99m}TcO_4$). The direct labeling approach under acidic conditions, afforded satisfactory labeling efficiency at pH 5.5, as confirmed by iTLC-SG and Whatmann cellulose paper using a gamma-detector.

Metalation of the first generation dendritic ligands with *fac*-$[^{99m}Tc(CO)_3OH_2]^+$ core was accomplished using *fac*-$[^{99m}Tc(CO)_3(OH_2)_3]^+$. The regioselective radiolabeling of the dendrimers was evaluated using the first generation ‘cold’ *fac*-$[Re_n(CO)_3(N,N\text{-bidentate})OH_2]^{n+}$ (n = 4) surrogates. The similarity in the UHPLC-UV/vis and UHPLC-Gamma detector chromatogram retention times for the *fac*-$[M_n(CO)_3(N,N\text{-}2\text{-}$

picolylamino)OH_2]$^{n+}$ (n = 4, M = Re(I) or ^{99m}Tc(I)) dendritic complexes confirmed a similar mode of complexation of the metal centres (Re(I) and ^{99m}Tc(I)) at the DAB-PPI periphery.

Symbols and abbreviations

α	Alpha
Å	Angstrom(s)
β	Beta
δ	Chemical shift
˚C	Degrees Celsius
γ	Gamma
β^+	Positron
β^-	Electron
λ	Wavelength
2D	Two-dimensional
3D	Three-dimensional
ACN	Acetonitrile
ATR	Attenuated total reflectance
APT	Attached proton test
Bpy	Bipyridyl
br	Broad
Br^-	Bromide
COSY	Correlation spectroscopy
$^{13}C\{^1H\}$	Proton decoupled carbon-13
d	Doublet
dd	Doublet of doublets
ddd	Doublet doublet of doublets
DAB	1,4-Diaminobutane
DMAP	4-Dimethylaminopyridine
EA	Elemental analysis
EI	Electron impact
EPR	Enhanced permeation and retention
ESI	Electrospray ionization
EtOH	Ethanol
FT-IR	Fourier transform-infrared
GBq	Gigabecquerel
^{68}Ga	Gallium-68
HR	Higher resolution
HSQC	Heteronuclear single quantum coherence
Hz	Hertz
IR	Infrared
J	Joule(s)
K	Kelvin
KeV	Kiloelectronvolt(s)
K_n	Stability constant (n = integer)
k_n	Second-order rate constant (n = integer)
Lit.	Literature
m	Multiplet
mCi	Millicurie
MeOH	Methanol

MBq	Megabecquerel
MHz	Megahertz
MP	Melting point
MS	Mass spectrometry
NMR	Nuclear magnetic resonance
PPI	Poly(propylene amine)
ppm	Parts per million
Py	Pyridyl
rt	Room temperature
s	Singlet
t_R	Retention time
t	Triplet
td	Triplet of doublets
^{99m}Tc	Technetium-99m
TOF	Time of flight

Chapter 1

Literature review

1.1. General introduction

According to the International Agency for Research in Cancer (IARC) under the World Health Organization (WHO), in 2012 there was an estimate of 14.1 million cancer cases, 8.2 million cancer deaths and 32.6 million people living with cancer (within 5 years of diagnosis) worldwide.[1,2] Breast cancer is the most common cause of death among women (522 000 deaths in 2012).[1,2] Colorectal and lung cancers are most notable in less developed countries of sub-Saharan Africa. The fourth most common cancer affecting women is cervical cancer (528 000 cases every new year).[1,2]

Overall, the most recent estimates for leading types of cancer dating from 2012, in both sexes, worldwide are:

- Lung (1.59 million deaths),
- Liver (745 000 deaths),
- Stomach (723 000 deaths),
- Colorectal (694 000 deaths),
- Breast (521 000 deaths),
- Oesophageal cancer (400 000 deaths).[2]

Based on statistical data, the WHO has postulated a substantive increase to 19.3 million new cancer cases per year by 2025.[1] Therefore, effective screening tools and technologies for cancer diagnosis and therapy are an increasing demand.

1.2. Cancer treatments

There are different medical procedures/therapies that a cancer patient may undergo to counteract the effect(s) of the disease. Depending on the state of the cancer upon diagnosis, there are prominent tools towards treating cancer, to mention a few: surgery, chemotherapy and radiation therapy. Surgery is used to remove or diagnose cancerous cells in an invasive manner, whereas, chemotherapy involves the use of synthetic drugs to treat cancerous cells.

1.2.1. Radiation therapy (Radiotherapy)

Radiotherapy involves the use of energy waves or energy particles to target cancer including non-cancerous diseases.[3] The types of radiation therapy include: external radiation therapy, 3D-conformal radiation therapy, intensity modulated radiotherapy (IMRT), stereotactic radiation therapy or radiosurgery, and internal radiation therapy or brachytherapy (implant radiation) where a high dose of radiation is given inside the body within a close proximity to the oncogene.[3] For years radioisotopes (radioactive isotopes) have been known as causative agents of cancer and now they have found routine applications in medical procedures.

1.3. Radioactivity

During a radioactive process, electromagnetic radiation or particles are emitted from an atom's nucleus and this can either occur naturally or be induced. Atoms are termed radioactive if their nuclei are unstable and randomly emit stray particles or energy waves namely: alpha (α), beta (β), and gamma (γ) radiation.[4-7] Approximately 270 of the existing isotopes are stable and 50 are naturally occurring radioisotopes. Artificial radioisotopes can be produced *via* nuclear bombardment reactions in a cyclotron, nuclear reactors, and/or nuclear generator.[6] Chemical reactions exploit the electron cloud (electron orbitals and hybridization) around the nucleus of an atom to form a stable compound, in contrast to nuclear reactions. Nuclear reactions focus on the features of the nucleus (*i.e.* protons and

neutrons: nucleons) to form a new isotope. The nucleus is held together by a strong nuclear binding force stronger than the repulsive force.[7] Thus, competition between the binding force and the repulsive electrostatic force determines the stability of an atom.

1.3.1. Alpha (α) particle emission

Alpha (α) decay is the emission of an α-particle (a helium atom) which consists of a two protons and two neutrons as shown in **Figure 1.1**.[4,7]

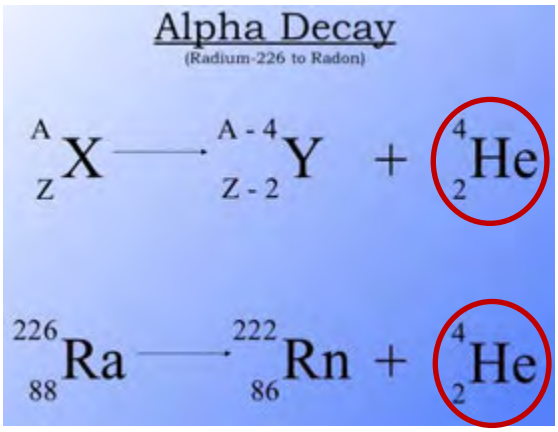

Figure 1.1: The emission of alpha particle (a helium atom, red encirclement) consists of two protons and two neutrons.

Figure 1.2 shows the alpha (α) decay scheme of the radioactive isotope [^{226}Ra]radium-226—derived from uranium—leading to the stable chemical element lead-206 (^{206}Pb).[7] The radioactive decay pathway can be a protracted process (up to years) or take up to seconds for completion, explaining that most naturally occurring chemical elements are regenerated with time.

Figure 1.2: The emission of an alpha particle from radium-226 nucleus leads to cascading events of radioactive decay to form lead-206. The radioactive decay may last for a protracted period or a short-period of time dependant on the nature of a radionuclide.[13] **y** = years, **d** = days, **m** = minutes and **ms** = milliseconds.

1.3.2. Beta (β) particle emission

Beta (β) decay involves the emission of an electron (β^-) or a positron (β^+) from the nucleus.[7] The former is not the same as the emission of an orbiting electron. An example of electron emission is the decay of carbon-14 to nitrogen-14 (such as neutron turning into a proton).[7,8] The decay of carbon-11 to boron-11 defines positron emission (such as proton turning into a neutron within the nucleus with the positron carrying off the positive charge).[7,8]

1.3.3. Gamma (γ) photon emission

Cobalt-60 decays to nickel-60 by β^- decay, however the nickel nucleus is formed in an excited state that subsequently emits two gamma (γ)-ray photons (very high energy photons, approximately 10^5 as energetic as visible light), known as γ-decay.[7,8] The nuclei that emit gamma-rays are the daughter nuclei of another radioactive decay. The difference between X-rays and gamma-rays, is that X-rays typically result from certain transitions of electrons surrounding the nucleus in the atom; whilst gamma rays are emitted from the nucleus itself.[8]

Rutherford discovered that the energies of the emitted particles and photons can penetrate tissue and can be halted by certain physical objects as shown in **Figure 1.3**.[7] The radionuclides that emit γ-photons and positron (β^+) particles are used in diagnostic nuclear medicine, whereas α-emitting and electron (β^-)-emitting isotopes confer therapeutic properties.[6,9]

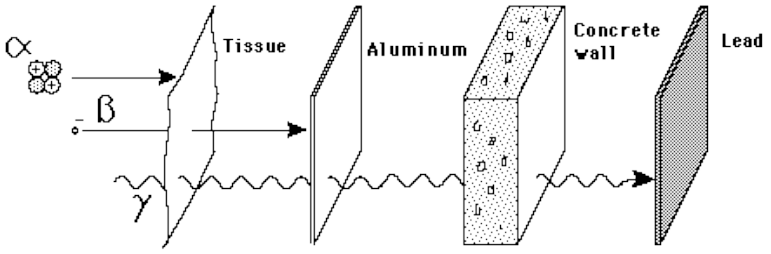

Figure 1.3: Schematic representation of three kinds of ionizing radiation. The α- particles include two electrons and two protons, they can be shielded by a piece of paper or human skin. The β^- particles involve high energy speed electrons and can be shielded by aluminium foil or wood. The γ-rays are essentially pure energy and are the most penetrating and can be shielded by a thick concrete or lead wall.

Currently in nuclear medicine, the design of tumour-targeting carriers to deliver radioactive metals (radioisotopes or radionuclides) selectively at target site *in vivo* is being exploited for both cancer therapy and diagnosis.

1.4. Metals in medicine

In the 1930s, the first experimental use of phosphorus-32 (β-emitting cyclotron produced radionuclide) for treatment of haematological disease, expanded the use of radionuclides in targeted therapy and for diagnostic imaging.[6] Radioisotopes of elements from the periodic table, when properly harnessed, find both clinical and research applications in radionuclide molecular imaging and therapy.[6] Radioisotopes are characterized into two classes: (i) therapeutics (*e.g.* ^{223}Ra, ^{90}Y, ^{47}Sc, ^{212}Pb, ^{225}Ac, $^{186/188}$Re, $^{212/213}$Bi, ^{114m}In, ^{177}Lu) which are β^- and α-emitters used in radionuclide-based therapy, and (ii) diagnostics (*e.g.* ^{99m}Tc,$^{67/68}$ Ga,

^{111}In, ^{86}Y, ^{89}Zr, ^{44}Sc, ^{64}Cu, ^{117}Lu) which are β^+ and γ-emitters used in nuclear imaging.[9]

Figure 1.4 highlights elements (shaded) with radioisotopes applied in clinic and research.[6]

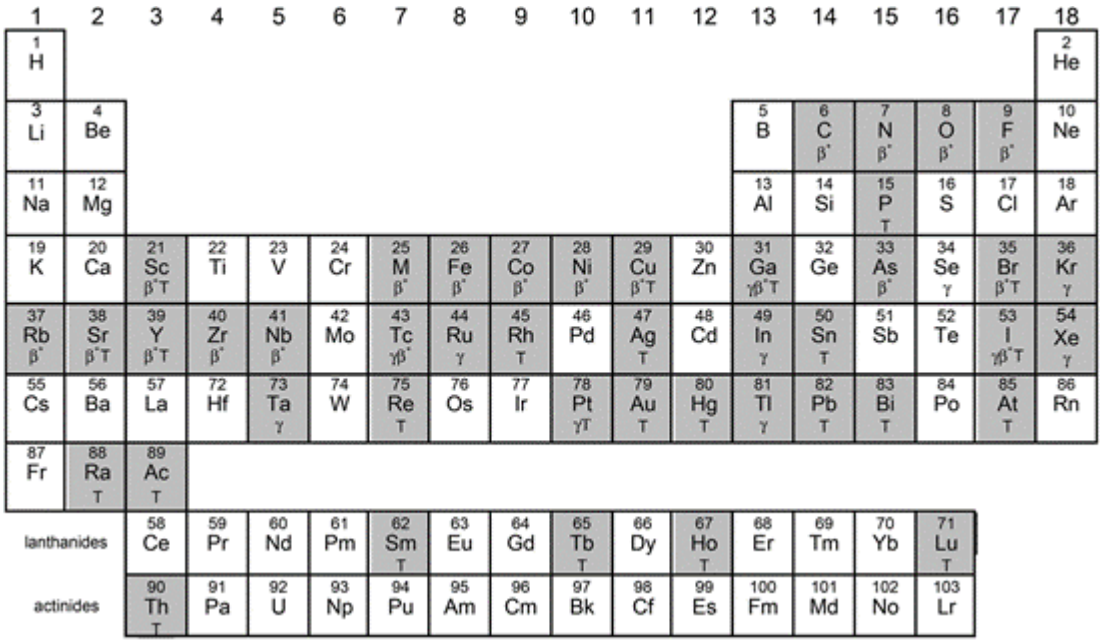

Figure 1.4: Chemical elements (shaded) with radioisotopes used in radiotherapy are shown with a letter T (therapy, using beta/β^-, alpha/α- or Auger-emitting radioisotopes). Radioisotopes used in nuclear imaging are identified by symbols γ (gamma) and β^+ (positron).[6]

The availability of radiometals makes it possible to select desired specific nuclear properties like emission types, half-lives, energies and coordination ratios, for nuclear medicine application.[6,10,11] For instance, a radionuclide's half-life should be long enough (for maximized biodistribution) to reach the target site after patient injection, but short enough to minimize radiation dose to the patient. Furthermore, the half-life should be long enough to allow transportation of the radionuclide between production site and examination room, but short enough to prevent long-term waste-handling issues for the hospital.[11] A selection of radionuclides (shaded in **Figure 1.4**) with eminent and imminent clinical and research applications will be discussed.

1.4.1. Organometallic (radio)pharmaceuticals

Organometallic drugs (carbon containing inorganic drugs) derived from stable (non-radioactive) isotopes have paved a way for radiometals in medicine. In 1910, Paul Ehrlich discovered arsphenamine (Salvarsan®, proposed structures shown in **Figure 1.5**) an arsenic-based antimicrobial compound, which demonstrated curative properties against syphilis (a sexually transmitted bacterial infection).[12]

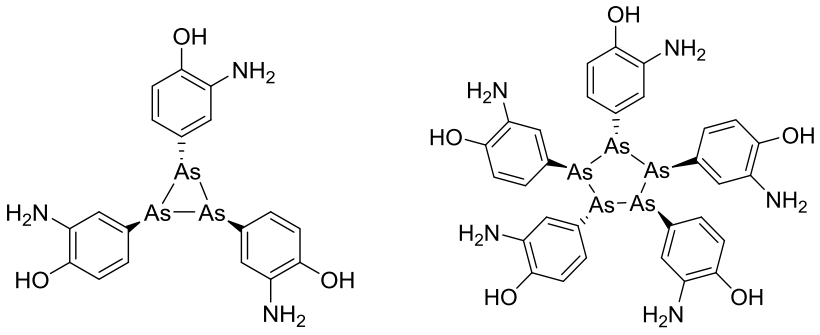

Figure 1.5: The proposed model of arsphenamine, a mixture of cyclic species.[12]

Therapeutic radiopharmaceuticals (drugs containing a therapeutic radioisotope coupled with a targeting biomolecule) are carriers designed to deliver a quantum of therapeutic ionization radiation (α-, β^- particles and/or secondary electrons) to specific diseased sites.[4-6] Ideally, they should be localized in diseased sites in sufficient concentration to deliver the cytotoxic radiation dose, while minimizing radiation damage by rapidly clearing from the blood stream, organs and tissues.[6]

1.4.2. Therapeutic radiopharmaceuticals

1.4.2.1. Rhenium-186/188

Elemental rhenium is polymeric and exists as rhenium-186/188 and these isotopes are therapeutic analogues of technetium-99m (a diagnostic radionuclide).[6,13] The precise isolation of these isotopes is based on their half-lives differing. The beta-emitting nuclear properties of

rhenium-186 (^{186}Re, β^-, 92.5% abundance, half-life = 90 hours) and rhenium-188 (^{188}Re, β^-, 100% abundance, half-life = 17 hours) affords prominent therapeutic properties.[6]

Though $^{186/188}$Re over time converts to perrhenate, $[ReO_4]^-$—which is taken up in the thyroid and is excreted renally—biodistribution studies, using indium-131 as a control, have shown the radiation characteristics of rhenium to confer a high dose deposition at the tumour site, and lower whole body radiation dose burden, making it a prominent therapeutic radionuclide.[13,14] Studies by Blower *et al*. accentuated the ^{188}Re-dimercaptosuccinic acid complex [^{188}Re(V)DMSA] (an analogue of [^{99m}Tc(V)DMSA] used for tumour imaging) as a potential palliative radionuclide treatment for bone metastases, in patients with prostate cancer.[15] Furthermore, the study of bisphosphonate ligands as prominent rhenium chelates to treat osteoblastic bone metastasis, with minimum bone marrow toxicity, has afforded $^{186/188}$Re-HEDP (HEDP = hydroxyethylidinedisphosphonate) and ^{188}Re-Dipicolylamine (DPA)-Alendronate (**Figure 1.6**) utility in management of pain palliation and disorders related to metastatic prostate cancer.[16] The bisphosphonate groups have a multimodal effect which is targeting the bone and binding the radioisotope.[13,16]

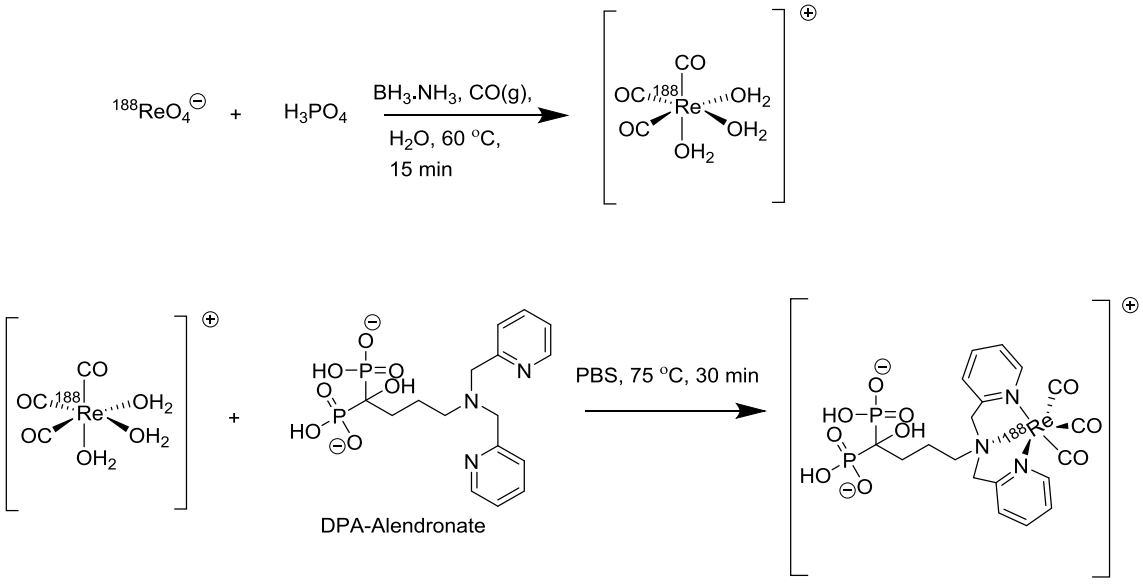

Figure 1.6: Radiolabeling protocol of the bone targeting rhenium-188 bisphosphonate complex [^{188}Re]Re(CO)$_3$-DPA-Alendronate.[16]

The high prospect to exploit a potential cost-effective $^{188}W/^{188}Re$ generator through the development of ^{188}Re radiopharmaceuticals will be subjected to the identification of an appropriate business model.[6]

1.4.3. Diagnostic radioisotopes

Diagnostic radioisotopes (emit gamma photons or positrons) are used for exploiting the tissue penetration depth of the gamma rays derived from either nuclear decay or during positron annihilation.[6] Diagnostic radiopharmaceuticals are compounds labeled with γ or β^+-emitting radioisotopes and their clinical applications include diagnosing, staging, and detecting the progression or recurrence of a disease.[5,6]

1.4.3.1. Technetium-99m

Stable technetium has not been reported to confer any biological significance like its radioactive counterpart technetium-99m (^{99m}Tc, γ-emitter, half-life = 6.01 hours).[6] The chemistry of ^{99m}Tc developed significantly in the 1970s and today ^{99m}Tc is the 'workhorse' of diagnostic nuclear medicine and is routinely used in hospitals.[6] **Table 1.1** lists selected FDA approved diagnostic radiopharmaceuticals.[17] The importance of ^{99m}Tc in nuclear medicine is attributed to its low cost production, $^{99}Mo/^{99m}Tc$ generator availability (as cyclotron production has distribution problems) and a 6 hour half-life. The single gamma photopeak at 141 keV with 89% abundance offers a close to ideal balance of attenuation and gamma camera sensitivity including resolution in the imaging of tissue.[6,18,19] Imaging agents like ^{99m}Tc-sestamibi, used for myocardial perfusion and breast cancer imaging, have found routine clinical application.[17]

Table 1.1: Selected FDA approved technetium-99m radiopharmaceuicals[17]

radioisotope	radiation	active ingredient	trade name	diagnostic imaging
^{67}Ga	γ	Ga-67 citrate		Hodgkin's disease, lymphoma, bronchogen
^{82}Rb	β^+	Rb-82 chloride	Cardiogen-82	myocardium
^{99m}Tc	γ	Tc-99m bicisate	Neurolite	stroke
^{99m}Tc	γ	Tc-99m disofenin	Hepatolite	cholecystitis
^{99m}Tc	γ	Tc-99m exametazime	Ceretec	stroke, abdominal infection
^{99m}Tc	γ	Tc-99m macroaggregated albumin		pulmonary perfusion, shunt patency
^{99m}Tc	γ	Tc-99m mebrofenin	Choletec	hepatobiliary system
^{99m}Tc	γ	Tc-99m medronate	MDP-Bracco	bone
^{99m}Tc	γ	Tc-99m mertiatide	Technescan MAG3	kidney
^{99m}Tc	γ	Tc-99m oxidronate	Technescan HDP	bone
^{99m}Tc	γ	Tc-99m pentetate		brain, kidney
^{99m}Tc	γ	Tc-99m pyrophosphate	Technescan, PYP	bone, myocardium, blood pool
^{99m}Tc	γ	Tc-99m red blood cells	UltraTag	blood pool
^{99m}Tc	γ	Tc-99m sestamibi	Cardiolite	myocardium, breast
^{99m}Tc	γ	Tc-99m sodium pertechnetate	Technelite	brain, thyroid, blood pool, urinary tract, nasolacrimal drainage system
^{99m}Tc	γ	Tc-99m succimer		kidney
^{99m}Tc	γ	Tc-99m sulfur colloid		lymphatic system, liver
^{99m}Tc	γ	Tc-99m tetrofosmin	Myoview	myocardium
^{99m}Tc	γ	Tc-99m tilmanocept	Lymphoseek	lymphatic system
^{111}In	γ	In-111 capromab pendetide	ProstaScint	prostate cancer
^{111}In	γ	In-111 chloride	Indidor	radiolabeling of ProstaScint
^{111}In	γ	In-111 oxyquinoline		leukocytes, inflammation
^{111}In	γ	In-111 pentetate		brain, spinal canal
^{111}In	γ	In-111 pentetreotide	Ocetreoscan	neuroendocrine tumors
^{201}Tl	γ	Tl-201 chloride		myocardium, thyroid

Synthetic advances in organometallic chemistry have enabled a simple one-step 'kit' process (*e.g.* isoLink® kit) towards the preparation of ^{99m}Tc radiopharmaceuticals. Several oxidation states exist for technetium with different chemical features.[6] The isoLink® kit offers the tricarbonyl core, *fac*-$[^{99m}Tc(CO)_3]^+$ isomer (present as *fac*-$[^{99m}Tc(OH_2)_3(CO)_3]^+$), which has been found to be: (i) a low spin d^6 inert complex and is a 'soft' acid, (ii) lipophilic—which may possess affinity to myocardial tissue—and organometallic in nature, (iii) chemically robust and maintains its integrity under harsh conditions, and (iv) the *fac*-$[^{99m}Tc(OH_2)_3(CO)_3]^+$ complex is obtainable under reducing conditions, in aqueous media from pertechnetate ($[^{99m}TcO_4]^-$), with the aqua ligands susceptible to nucleophilic substitution

by entering ligands (allowing for facile coordination to biomolecules and efficient radiolabeling).[20-24]

Since technetium is a rhenium congener, non-radioactive ('cold') Re(I) analogues are used in characterization of radioactive ('hot') ^{99m}Tc(I) adducts.[6] Technetium and rhenium complexes with tricarbonyl ligands, nitride-dithiocarbamate ligands or oxo-ligands (*e.g.* MAG3 and tetraamines) are relatively similar in chemical reactivity (although they require different reaction conditions) and chemical structures.[6] The latter can be confirmed, using chromatographic techniques, by comparing retention times of the 'cold' and 'hot' complexes. The major difference between 'cold' and 'hot' metal ion chemistry is that radiochemistry is performed under extremely dilute conditions, with the radiotracer present in nanoMolar to picoMolar concentrations.[9]

1.5. Non-invasive nuclear imaging modalities

The year 2000 represents an important milestone in nuclear imaging.[11] In the US, the number of PET procedures increased from 0.2 million to 1.85 million in 2012.[11] Between year 2005 – 2012, a 21% increase was observed in Europe.[11] The popularity of PET scan over SPECT scan can be attributed to the way the isotopes are produced (*i.e.* in a reactor or cyclotron), packaged (*i.e.* radiolabeled molecules or generators) and distributed.[11] PET scans may offer increased accuracy and sensitivity by two to three orders of magnitude compared to SPECT, and can give a resolution of approximately 4 millimetres or more in a 3D output.[25]

1.5.1. Single Photon Emission Computed Tomography (SPECT) scans

Gamma-ray emitting radionuclides (*i.e.* heavy isotopes) are used in SPECT. The radiation is measured directly by gamma cameras during radioactive decay.[25] SPECT offers a prolonged observation window owing to prolonged half-lives of single photo emitters.[26] This allows for

observation, at about 1 cm resolution, of biological processes (e.g. blood flow to the brain) *in vivo*, several hours or days after introduction of an appropriate nuclear imaging compound.[26]

Recent innovations in SPECT procedures include combined modality imaging by incorporating a radioisotope and a magnetic resonance contrast (most common are SPECT/CT procedures).[6] This has created interest in developing contrast agents that support both imaging modalities (SPECT/MRI-magnetic resonance imaging) for clinical applications. One clinical application of this combined approach includes sentinel lymph node imaging (SPECT used to identify a location *in vivo* and MRI to provide soft tissue contrast and structural elucidation) to identify lymph nodes draining tumours prior to surgery, and a fluorescent contrast as a guide during surgery.[6] **Table 1.2** lists some physical properties of SPECT radiometals.

Table 1.2: Physical Properties of Some Common SPECT Radiometals[27]

isotope	half-life/h	source	production reaction	decay mode (% branching ratio)	E_γ/keV	abundance, I_γ/%	relevant oxidation states	common coordination numbers
^{67}Ga	78.2	cyclotron	^{nat}Zn(p,x)^{67}Ga ^{68}Zn(p,2n)^{67}Ga	ε (100)	91.265(5) 93.310(5) 184.576(10) 208.950(10) 300.217(10) 393.527(10)	3.11(4) 38.81(3) 21.410(10) 2.460(10) 16.64(12) 4.56(24)	3+	4, 5, 6
^{99m}Tc	6.0	generator	^{99}Mo/^{99m}Tc	β^- (0.0037) IT (99.9963)	140.511(1)	89.06	1− to 7+	4, 5, 6
^{111}In	67.3	cyclotron	^{111}Cd(p,n)^{111}In	ε (100)	171.28(3) 245.35(4)	90.7(9) 94.1(10)	3+	5, 6, 7, 8

1.5.2. Positron Emission Tomography (PET) scans

PET is similar to SPECT as both imaging modalities require the use of radioactive nuclides and detection of γ-rays. Short-half-life radionuclides are used in PET. **Table 1.3** lists some physical properties of PET radiometals.

Table 1.3: Physical Properties of Some Common PET Radiometals[27]

isotope	half-life/h	source	production reaction	decay mode (% branching ratio)	E_{β^+}/keV	abundance, I_{β^+}/%	E_γ/keV (intensity, I_γ/%)	relevant oxidation states	common coordination numbers
^{64}Cu	12.7	cyclotron	^{64}Ni(p,n)^{64}Cu	$\varepsilon + \beta^+$ (61.5) β^+ (17.6) β^- (38.5)	278.2(9)	17.60(22)	511.0 (35.2)	1+, 2+	4, 5, 6
^{68}Ga	1.1	generator	^{68}Ge/^{68}Ga	$\varepsilon + \beta^+$ (100) β^+ (89.1)	836.02(56)	87.94(12)	511.0 (178.3)	3+	4, 5, 6
^{86}Y	14.7	cyclotron	^{86}Sr(p,n)^{86}Y	$\varepsilon + \beta^+$ (100) β^+ (31.9)	535(7)	11.9(5)	443.1 (16.9) 511.0 (64) 627.7 (36.2) 703.3 (15) 777.4 (22.4) 1076.6 (82.5) 1153.0 (30.5) 1854.4 (17.2) 1920.7 (20.8)	3+	8, 9
^{89}Zr	78.4	cyclotron	^{89}Y(p,n)^{89}Zr	$\varepsilon + \beta^+$ (100) β^+ (22.7)	395.5(11)	22.74(24)	511.0 (45.5) 909.2 (99.0)	4+	8

When a positron is ejected from the nucleus it travels a distance (termed positron range), finds an electron and the pair annihilate.[11,28] Prior to the annihilation, the radioisotope loses energy by emitting ionizing radiation.[11] Depending on the isotope, the positrons that represent a fraction of the total amount of decays (branching ratios) are emitted in a continuous kinetic energy spectrum defined by the maximum energy available.[11] *In vivo*, the positron loses its initial energy by colliding with the atoms in the surrounding tissue. Once the positron becomes sufficiently small, the particle instantaneously finds a free electron and the pair collide producing mass energy which is converted into two gamma photons (511 keV).[11] These photons contain momentum and the conservation of momentum requires that they travel in opposite directions (180 °C opposed) as illustrated in **Figure 1.7 top**.[25,28]

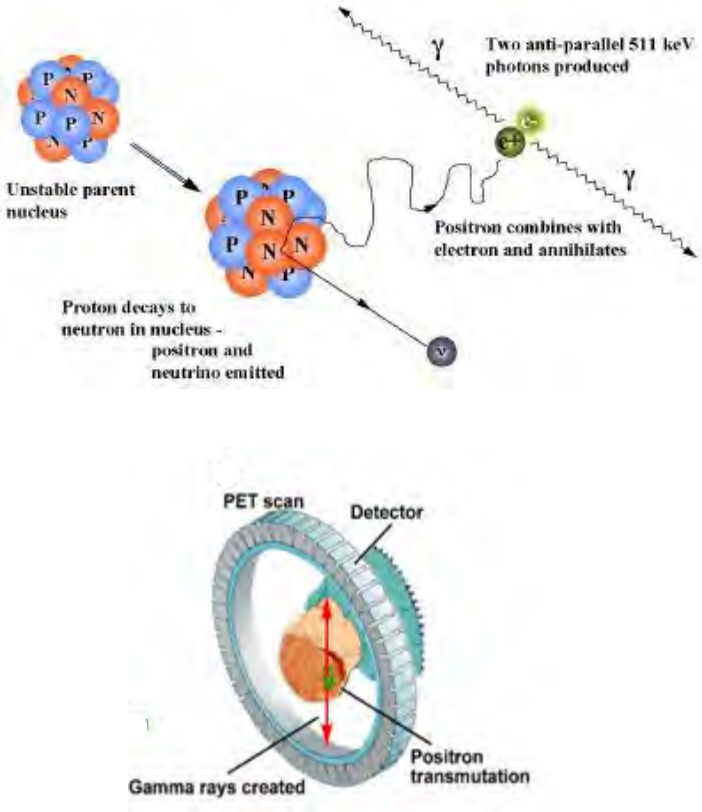

Figure 1.7: Schematic representation (**Top)** of a positron and an electron annihilate producing two back-to-back photons of equal energy to be detected (**Bottom)** by a circular gamma ray detector in the PET scan shown.

These photons are then detected by detectors on a PET camera, **Figure 1.7 bottom**.[25] PET scans can have approximately 2048 detecting crystals in the ring of the dome of the camera, making these scans costly and possess higher resolution images than SPECT scans.

1.5.3. Advancements in nuclear imaging scans

Radionuclides like ^{34m}Cl, ^{44m}Sc, ^{52}Mn, ^{86}Y, ^{94}Tc and ^{152}Tb give a gamma-photon emission accompanying the positron emission which results in a total of 3 gamma – rays.[11] The two back-to-back γ-rays at 511 keV (due to annihilation, **Figure 1.7**) are detected by classical PET methods giving a line of response (the line along the photons' path, **Figure 1.7**). The third γ-ray is then detected and located by an additional camera (currently under development).[11,28] This additional emission increases radiation burden to the patient. Thus, dedicated cameras are under development to simultaneously measure the lines of response

generated by the annihilation and the third photons.[28,29] The intersection of the two lines will decrease the uncertainty on the annihilation position, increase signal-to-noise ratio and provide a decreased overall radiation exposure of the patient.[11]

1.6. Coordination compounds

Radiotracers are sequestered from aqueous media by coordinating Lewis bases. Chelating ligands encapsulate a radiotracer and insulate it from the surrounding environment.[9] In addition, the chelator must effectively transport the radiotracer to selective biological target sites.[9]

1.6.1. Ligand design

A diagnostic radiopharmaceutical may comprise a radiotracer of specific emission type (γ for SPECT and β^+ for PET) and a chelator that gives optimal complex stability.[9] H_2dedpa (a member of the 'pa family' due to the central picolinic acid 'pa' binding moieties, **Table 1.4**) is one of the common ligands frequently reported in literature as a prominent chelate to form kinetically inert complexes with certain radioisotopes.[9] Radiolabeling of the acyclic hexadentate scaffold of H_2dedpa with $^{67/68}$Ga can be performed at room temperature in less than 10 minutes, with no decomposition observed after 2 hours post labeling, to afford products with distorted octahedron coordination geometry.[30,31] The complex stability constants (log K_{ML}) obtained from potentiometric titration studies indicate high thermodynamic stability, and affinity of H_2dedpa for $^{67/68}$Ga(III) (log K_{ML} = 28.1) over ^{64}Cu(II) (log K_{ML} = 19.2).[30]

Table 1.4: H_2dedpa and its bifunctional derivative with corresponding relevant radiotracers, radiolabeling conditions, thermodynamic stability constants ($logK_{ML}$), and coordination geometries[9,30]

✓ = best match, ~ = suitable or potential match

Chelator and common bifunctional derivatives	Radiometal ion	a	Radiolabeling conditions	$\log K_{ML}$	Proposed geometry
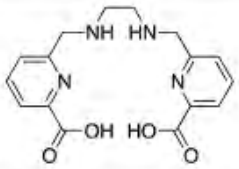 H_2dedpa, 1,2-[[6-(carboxy)-pyridin-2-yl]-methylamino]ethane, N_4O_2 CN = 6	$^{64}Cu^{2+}$	~	25 °C, 5–10 min, pH 5.5	19.2 (pM = 18.5)	Distorted octahedron
	$^{67/68}Ga^{3+}$	✓	25 °C, 5–10 min, pH 4.5	28.1 (pM = 27.4)	Distorted octahedron
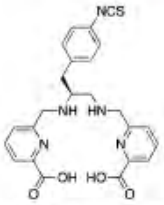 *p*-SCN-Bn-H_2dedpa					

Current progress in ligand design of tumour-targeting metal chelates involves the incorporation of hyperbranched polymeric structures, such as dendrimers, which permit multivalent attachment possibilities of metal ions.[32]

1.6.2. Dendrimers

In 1978, Vögtle *et al.* were the first to report on dendrimers (initially termed 'cascade' molecules).[32] The term 'dendrimer' (from Greek: *dendra*, tree and *meros*, part of) describes a class of tree-like structure, as shown in **Figure 1.8**, of polymeric macromolecules.[33] Dendrimers are synthetic nanosized (~10-20 nm) macromolecules that emanate from a central core (**Figure 1.8**), with covalently linked branch units that fan out in well-defined globular architectures in 3D.[33-35]

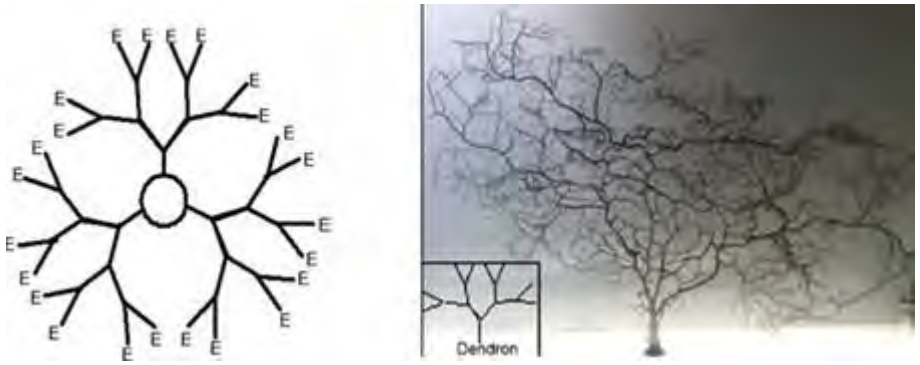

Figure 1.8: A typical dendrimer structure (left) is made of three units: a multifunctional central core (O), branched units(Y) and external capping groups (E). The branched unit, dendron, resembles the structure of a tree (right).[33]

The tree-like architecture (**Figure 1.8**) enables multifunctional modification at the periphery permitting functionalization with various drug molecules or metal ions.[34] Dendrimers have found utility in catalysis, electronics, and medicine.[34-37] They have been found to function as drug solubility enhancers (*e.g.* Conjugation of Paclitaxel® to a dendrimer moiety increased drug solubility from 8μg/100 ml to <35mg/100 ml), to release modifiers as well as platforms for drug targeting.[38,39]

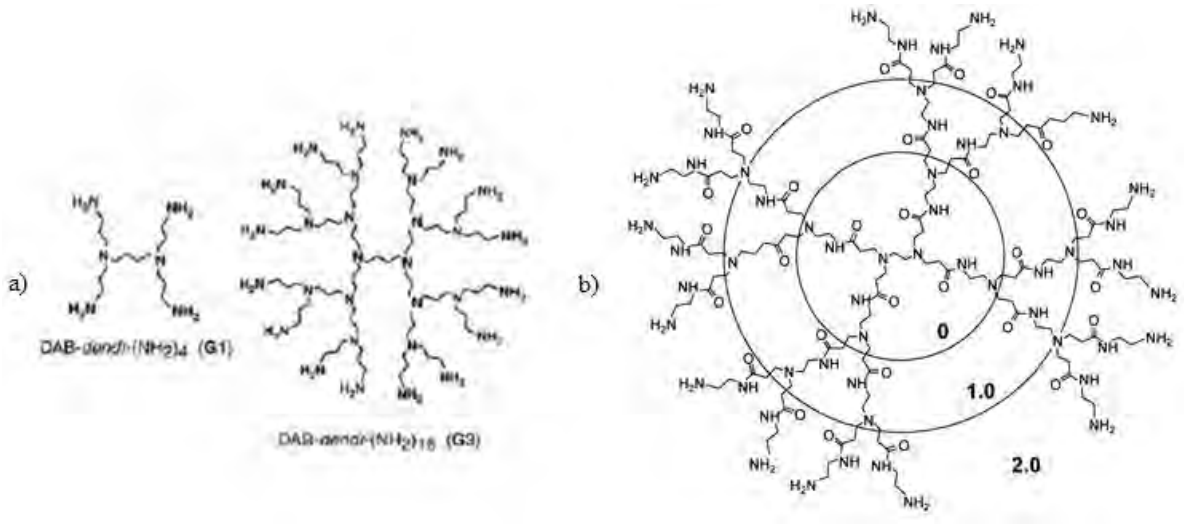

Figure 1.9: Proposed generations of monodispersed dendritic architecture. (a) Examples of commercialy available generations (G1 = generation 1, G3 = generation 3,*etc*) of monodispersed poly(propylene imine) dendrimer (PPI) where diaminobutane (DAB) is the core and (b) The polyamidoamine (PAMAM) dendrimer showing dendritic scaffolds leading to generation 2 PAMAM dendrimer. PAMAM has found application in Magnetic Resonance (MRI) imaging.[40-43]

In light of this, dendrimers can be viewed as discrete platforms of tunable and controlled size (*e.g.* to allow crossing of the capillary barrier and urinary elimination), efficient carriers, and their biodistribution and pharmacokinetic traits can be controlled with respect to surface functionalization.[4,44]

1.6.3. Biocompatibility studies on dendrimers

Macromolecules such as dendrimers have been found to accumulate at tumour sites as a result of an increase in blood vessel permeability and poor lymphatic drainage within diseased tissue than in healthy cells (also known as the 'enhanced permeability and retention' (EPR) effect), **Figure 1.10**.[42-45] Dendrimers have found application in Magnetic Resonance Imaging (MRI), they have been investigated in gene therapy, as radiation sensitizers, and carriers for therapeutic drugs.[4]

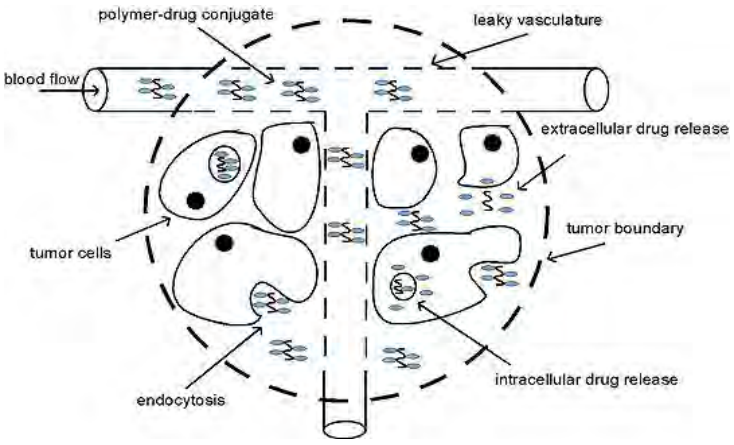

Figure 1.10: The EPR ('enhanced permeability and retention') effect of a polymer-drug conjugate in a tumour.[45]

The biocompatibility of amine-terminated dendrimers (**Figure 1.9**) has been investigated before. A study by Zinselmeyer *et al*. to evaluate poly(propylene imine) (PPI) dendrimers as gene delivery systems showed that the fifth generation (G5) PPI dendrimer DAB-dendr-$(NH_2)_{64}$ has an $IC_{50} < 5$ μg mL^{-1} when tested against A-431 (epidermoid carcinoma) cell line.[46] The second generation (G2) PPI dendrimer was found to have sufficient level DNA

binding with low level of cell cytotoxicity affording it optimum *in vitro* gene transfer activity.[46] Malik *et al*. reported haematoxicity studies on rat blood cells using protonated PAMAM and PPI dendrimers, bearing amine ($-NH_2$) termini at the periphery, to show an increased haemolytic effect with increasing dendrimer generation number.[47] In contrast, when these dendrimer generations were functionalized with carboxylate end groups at the periphery they conferred no cytotoxic and haemolytic activity up to a concentration of 2 mg/mL.[47] In general, cationic dendrimers displayed IC_{50} values ranging between 50 – 300 μg/mL dependent on dendrimer-type, cell-type and generation.[47] This suggests the overall toxicity of dendritic architectures is determined by termini functional groups and can be attributed to the charge-charge interactions between the cell membrane and the dendrimer.[43,48] In addition to the PAMAM and PPI dendrimers, the peptide-functionalized poly(lysine) dendrimers were also found to be biocompatible.[49]

1.6.4. Metallodendrimers

When dendrimers are functionalized with transition metals at the dendritic core, tether termini, dendritic branches, or at the branching point they are termed metallodendrimers (**Figure 1.11**).[42] Metallodendrimers with metal centres at different positions have been reported to have catalytic, redox activity, conductivity, luminescence and magnetism properties.[44]

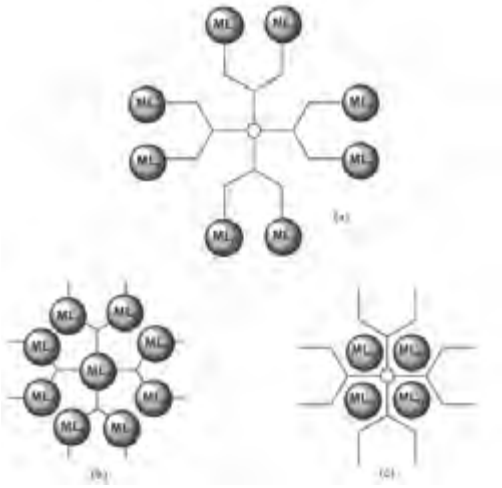

Figure 1.11: Schematic representation of metal decorated dendrimers (a) at the periphery (b) interspersed throughout the framework(c) encapsulated within the framework.[42]

The use of metallodendrimers in drug delivery is an attractive strategy. Their multivalency allows multiple copies of therapeutic metals to be attached, as shown in **Figure 1.11**, for biological recognition processes. The concept of multinuclearity to increase bioactivity has been attempted before. Jansen *et al*. synthesized and evaluated a tetranuclear dendritic platinum complex in **Figure 1.12**, DAB(PA-tPt-Cl)$_4$.[50] This compound was designed to overcome problems linked with cisplatin in the S-phase of the cell cycle. However, the compound evaluation studies showed low cytotoxic activity (associated with high charge of the complex at blood pH) against cancer cell lines and poor cell membrane diffusion.[50]

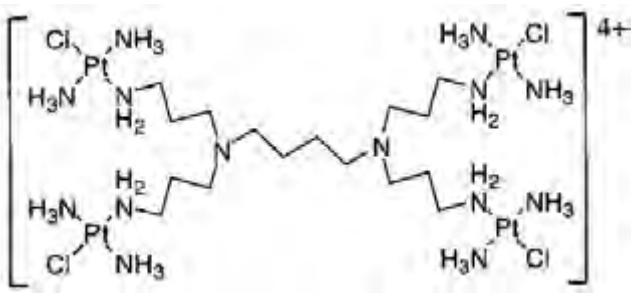

Figure 1.12: The proposed structure of DAB(PA-tPt-Cl)$_4$ a multinuclear cationic platinum complex.[50]

Another example is BBR 3464, **Figure 1.13**, a trinuclear platinum compound which completed phase I clinical trials overcoming cisplatin resistance mechanism.[51] Even though

this compound was unsuccessful in phase II clinical trials, it has paved the possibility to combine dendritic cores with various metal units at once.[51]

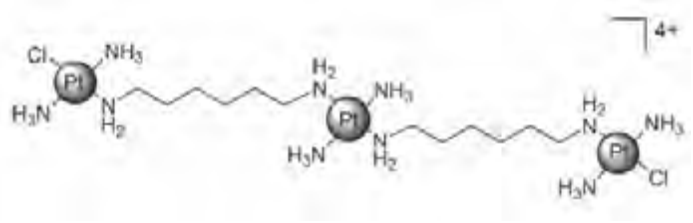

Figure 1.13: BBR 3464, a multinuclear cationic *trans*-platinum(II) compound.[51]

1.7. Metallodendrimers in nuclear imaging – the development of dendritic diagnostic radiopharmaceuticals

The enhanced sensitivity of imaging modalities permits injection of radiopharmaceuticals at very low concentrations, ~ 10^{-6} – 10^{-8} M, and they are not intended to confer any pharmacological effect.[4] Conventional nuclear imaging with radiolabeled tumour-specific probes often suffers from slow signal localization and clearance.[4] In cancer imaging and therapy, the current focus is on the development of *theranostics* - novel tumour-specific probes supplying image-guided therapy.[4] The multivalent nature of dendrimers can afford attachment possibilities of diverse metallic radionuclides to deliver radiotherapy and diagnostic imaging for efficacy treatment follow up, surgical biopsy guidance and automated pathologic analysis of cancer biopsy and surgical samples.[4]

^{99m}Tc-labeling has been proven to be an effective approach in evaluating organ distribution studies of drug carriers for therapy and diagnosis.[4] Pioneering work in demonstrating the potential of radioactive metallodendrimers as tumour imaging and diagnosis agents is by Subbarayan *et al*.[52] This group was able to radiolabel water-soluble dendritic architectures bearing porphyrin cores with terminal iminodiacetic acid groups serving as ^{99m}Tc (a diagnostic radioisotope) chelates.[52] Chromatography of the radiolabeled products showed

radiochemical purity of greater than 95% (an accepted limit by the European Pharmacopoeia for radiochemical purity of a radiopharmaceutical is ≥ 95%). Scintigraphic imaging and biodistribution studies on C_6-glioma tumour-bearing Wistar rats showed the radiolabeled dendrimers to accumulate in the tumour rather than in the surrounding muscles.[52]

Agashe *et al*. used the ^{99m}Tc-labeling technique to radiolabel mannose or lactose coated generation 5 PPI dendrimers.[53] When the carbohydrate 'free' ^{99m}Tc-dendrimers were used as standards, the biodistribution studies in mice demonstrated that they cleared from the systematic circulation slower than the ^{99m}Tc-labeled carbohydrate-coated dendrimers. The protracted retention times of the ^{99m}Tc-glycodendrimers were notable in the liver, attributed to lectin receptor-carbohydrate interactions.[53] This is a great indication of carbohydrate-coated dendrimers as potential radionuclide delivery vehicles to lectin-rich organs.[4,53]

Parrot *et al*. used ^{99m}Tc to perform core metalation of high-generation polyester dendrons covalently linked to a tridentate bis(pyridyl)amine ligand, **Figure 1.14** (synthesis of the 'cold' technetium complex).[54] Using a dynamic small-animal SPECT/Computed Tomography (SPECT/CT) scan, the distribution studies of the radiolabeled dendrons in healthy adult Copenhagen rats showed higher dendrimer generation 5 to 7 to be rapidly eliminated from the blood stream and excreted through bladder 15 minutes post-injection.[54] The rapid clearance of the dendrons is likely attributed to their molecular weights (generation 5 = 4.1 kDa, generation 6 = 7.8 kDa and generation 7 = 15.2 kDa) being below the renal filtration cut-off of 40 – 60 kDa.[4]

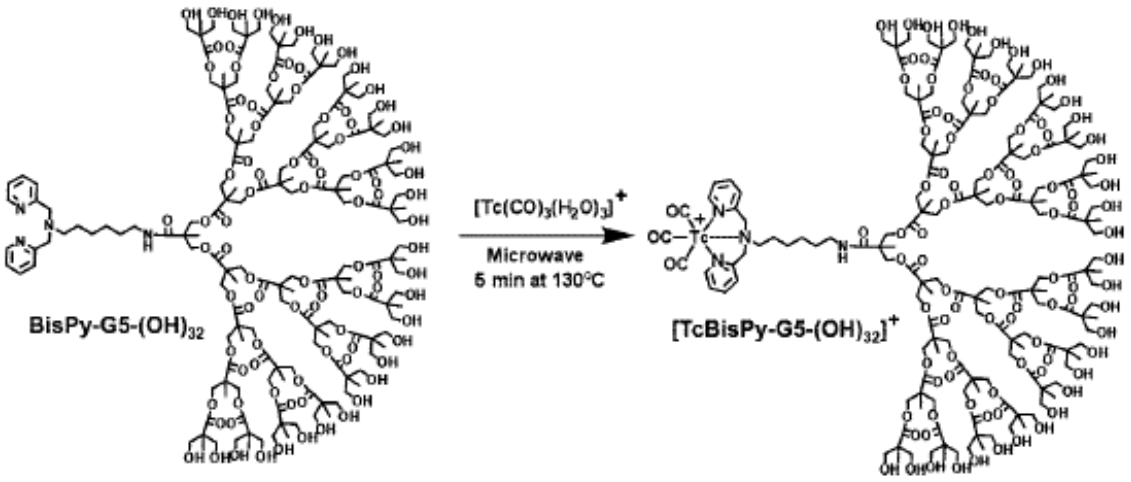

Figure 1.14: The structure of generation 5 ^{99m}Tc-labeled poly(2,2-bis(hydroxymethyl)-propionic acid) Dendron based on the HPLC of the 'cold' technetium complex shown in the scheme.[54]

This study demonstrates the possibility to prepare well-defined/site-specific diagnostic radiopharmaceuticals by radiolabeling the focal point of high generation dendrons suitable for SPECT imaging through the incorporation of a single high affinity ^{99m}Tc ligand.[4] In principle, this should assist in minimizing the impact of the radiotracer in interfering with the dendrimer periphery–receptor binding interactions during blood and tissue circulation.[55]

To target folate receptors over-expressed in cancer cells, Zhang *et al*. used generation 5 PAMAM dendrimers functionalized at the primary amines periphery with diethylenetriamine pentaacetic acid (DTPA, an aminopolycarboxylic acid) as ^{99m}Tc chelate and folic acid (FA) as the receptor binding moiety (**Figure 1.15**).[56] The radiolabeled PAMAM-FA conjugate was stable in phosphate buffer (pH 7.4) and serum over a period of 6 hours after labeling (radiochemical purity ≥ 95%), biodistribution studies in nude mice confirmed accumulation at the tumour site within 6 hours and rapid blood clearance.[56]

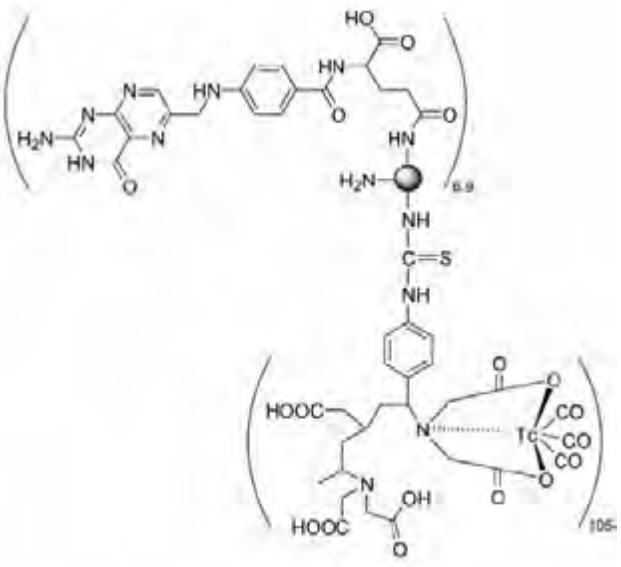

Figure 1.15: Representation of the chemical structure of [^{99m}Tc]Tc(CO)$_3$-G5-FA-DTPA.[56]

Subsequent studies on radiolabeled PAMAM-FA conjugate in the presence of a spacer group polyethylene glycol (PEG) for indirect conjugation of FA with fifth generation PAMAM resulted in increased tumour uptake.[57] PEG is structurally flexible and lipophilic in nature, potentially allowing for escape from phagocytosis by macrophage cells in the lymphatic system. Thus, FA modified with the spacer group PEG is able to trigger receptor-mediated endocytosis by selectively binding to metastatic tumour-cells.[4,57] For cancer diagnosis, such a study confirms the potential of FA-dendrimer conjugates as potential imaging radiopharmaceuticals.[4]

1.8. Perspectives

The integration of a diagnostic radionuclide with a target-specific dendrimer either modified at the periphery, covalently bonded to a spacer group or conjugated with receptor binding moieties (like folic acid) affords optimization of diagnostic efficacy in targeting diseased sites. Application of dendrimers as prominent radiopharmaceutical chelates in nuclear imaging (and therapy) is still under research and holds promising results. Based on the dendritic architectures which permit multinuclearity, the ability to tune the ratio between the

macromolecule and the radiometal for enhanced biodistribution and image quality can be exploited. Studies have shown the radiolabeling of dendrimers and dendrons with *fac*-$[^{99m}Tc(CO)_3]^+$ isomer including purification (based on radiochemical yields) as being achievable.[52-57] The nature of functional groups ('hard' or 'soft' donor atoms) at the periphery of the dendrimer is essential for the synthesis of kinetically inert radiolabeled complexes. The commercial availability of some dendrimers and accessibility to ^{99m}Tc (cheaper production) in most regions of the world will lead to the discovery of novel dendritic diagnostic radiopharmaceuticals. Thus, exploiting the diagnostic properties of the gamma-emitting radionuclide ^{99m}Tc, where labeling can be performed using kit processes, together with the 'enhanced permeability and retention' (EPR) effect of the dendrimer-based ligands will be a major contribution to research on nanoparticle based drug delivery systems and cancer diagnosis research.

1.9. Aims and Objectives

1.9.1. General aims

The general aims of this project are:

- The design and synthesis of bidentate monomeric and dendritic ligands
- Coordination of these ligands to a aquatricarbonylrhenium(I) core, the *fac*-$[Re(CO)_3H_2O]^+$ isomer, to afford 'cold' rhenium complexes as high-performance liquid chromatography (HPLC) standards
- Radiolabeling of the ligands using generator eluted technetium-99m ($[^{99m}TcO_4]^-$) and the isoLink® kit (*fac*-$[^{99m}Tc(CO)_3(H_2O)_3]^+$)
- Evaluate the radiolabeled properties of the corresponding complexes

1.9.2. Specific objectives

1.9.2.1. Synthesis

- To synthesize a series of monomeric and dendritic ligands from iminopyridyl or bipyridyl synthons (**Figure 1.16**).

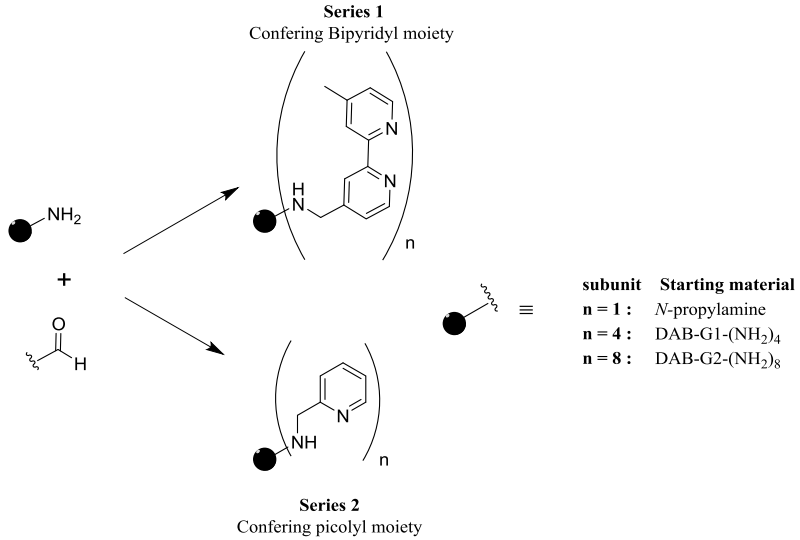

Figure 1.16: The synthetic route towards the proposed monomeric and dendritic neutral ligands of series 1 and 2.

- To use the aforementioned ligands in synthesizing 'cold' *fac*-$[Re(I)(CO)_3]^+$ complexes in **Figure 1.17** and devise a chromatographic method to compare the retention times with those of radioactive counterparts.

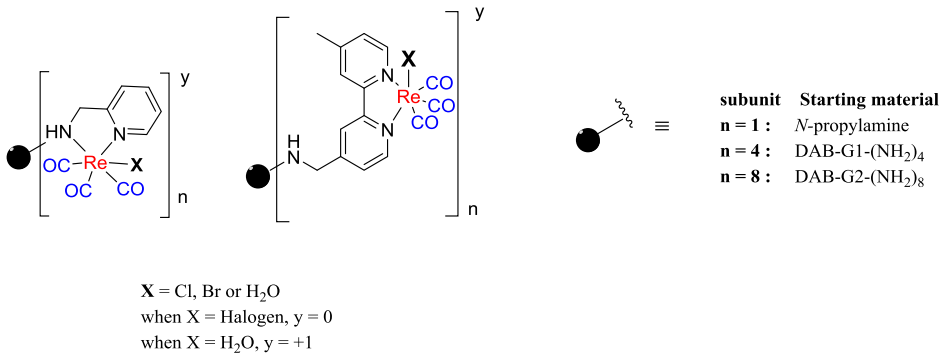

X = Cl, Br or H_2O
when X = Halogen, y = 0
when X = H_2O, y = +1

Figure 1.17: The proposed structures of the mononuclear and multinuclear Re(I) tricarbonyl cores

- To radiolabel the dendritic ligands in **Figure 1.16** with ^{99m}Tc using reduced pertechnetate by direct labeling and/or isoLink® kit method(s).

1.9.2.2. Applications

- Since the ligands are bidentate, the lability or inertness of the aqua ligand in *fac*-$[Re(CO)_3(N,N\text{-bidentate})(OH_2)]^+$ type complexes will be investigated in kinetic studies to evaluate the influence of dendritic ligand on the reactivity of the rhenium(I) centre.
- Develop suitable HPLC and instant thin layer chromatography (iTLC) methods to monitor reactions and to determine (radio)chemical purity of intermediates and final products
- Develop methods to determine radiochemical stabilities of the labeled compounds
- Perform radiobiological studies- *i.e. in vitro* cell uptake studies will be performed using radiolabelled metallodendrimers.

1.10. References

1. International Agency for Research on Cancer (IARC), World Health Organisation (WHO), *GLOBOCAN 2012: Estimated cancer incidence, mortality and prevalence worldwide in 2012*, http://globocan.iarc.fr/Pages/fact_sheets_cancer.aspx (date accessed: 28 February 2015)
2. B. W. Stewart, C. P. Wild, *World Cancer Report 2014*, IARC, ISBN: 978-98-832-0429-9.
3. Stanford Cancer Center https://stanfordhealthcare.org/medical-treatments/r/radiation-therapy/radiation-therapy-types.html. (date accessed: 07 July 2015)
4. C. Ghobril, G. Lamanna, M. Kueny-Stotz, A. Garofalo, C. Billotey, D. Felder-Flesch, *New J. Chem.,* 2012, **36**, 310 – 323.
5. E. M. Jagoda, L. Lang, V. Bhadrasetty, S. Histed, M. Williams, G. Kramer-Marek, E. Mena, L. Rosenblum, J. Marik, J. N. Tinianow, M. Merchant, L. Szajek, C. Paik, F. Cecchi, K. Raffensperger, J. M. Jose-Dizon, D. P. Bottaro, P. Choyke, *J. Nucl. Med.*, 2012, **53**, 1592 − 1600.
6. P. J. Blower, *Dalton Trans.*, 2015, **44**, 4819 – 4844.
7. E. Rutherford, *The newer Alchemy*, Cambridge University Press, Cambridge, UK, 1937, 60.
8. R. L. Reese, *University Physics,* Brooks/Cole Publishing Company, USA, 2000, 1208, 1225 – 1227.
9. E. W. Price, C. Orvig, *Chem. Soc. Rev.*, 2014, **43**, 260 – 290.

10. B. M. Zeglis, J. L. Houghton, M. J. Evans, N. Viola-Villegas, J. S. Lewis, *Inorg. Chem.*, 2014, **53**, 1880 – 1899.

11. D. Brasse, A. Notat, *Dalton Trans.*, 2015, **44**, 4845 – 4858.

12. M. D. Wissing, F. W. van Leeuwen, G. van der Pluijm, H. Gelderblom, *Clin. Cancer Res.*, 2013, **19**, 5822 – 5827.

13. J. K. Bordoloi, D. Berry, I. U. Khan, K. Sunassee, R. T. M. de Rosales, C. Shanahan, P. J. Blower, *Dalton Trans.*, 2015, **44**, 4963 – 4975.

14. U. Abram, S. Abram, R. Alberto, R. Schibli, *Inorg. Chim. Acta*, 1996, **248**, 193 – 202.

15. P. J. Blower, A. G. Kettle, M. J. O'Doherty, A. J. Coakley, F. F. Knapp, *Eur. J. Nucl. Med*., 2000, **27**, 1405 – 1409.

16. P. J. Blower, R. Torres Martin de Rosales, *UK Patent*, WO 2010116132 A3, 2011.

17. Cardinal Health. FDA-Approved Radiopharmaceuticals; Rev. 8 No. 6.5.13; http://www.cardinal.com/mps/wcm/connect/1bcdfc80447f1763b29ab77fc4070dc5/7COMPLI9958_FDA-approved_list_082412_v3.pdf?MOD=AJPERES (date accessed 07 April 2015)

18. K. D. Mjos, C. Orvig, *Chem. Rev.*, 2014, **114**, 4540 – 4563.

19. S. S. Jurisson, J. D. Lydon, *Chem. Rev.,* 1999, **99**, 2205 – 2218.

20. R. Alberto, R. Schibli, R. Waibel, U. Abram, P. A. Schubiger, *Coord. Chem. Rev.,* 1999, **192**, 901 – 919.

21. R. Alberto, R. Schibli, A. Egli, A. P. Schubiger, *J. Am. Chem. Soc.,* 1998, **120**, 7987 – 7988.

22. R. Alberto, *J. Organomet. Chem.*, 2007, **692**, 1179 – 1186.

23. R. Alberto, H. Braband, H. W. P. N'Dongo, *Curr. Radiopharm*, 2009, **2**, 254 – 267.

24. G. E. Kodina, A. O. Malysheva, O. E. Klement'eva, A. A. Inkin, N. I. Gorshkov, A. A. Lumpo, D. N. Suglobov, *J. Nucl. Radiochem. Sci.,* 2005, **6**, 183 – 185.

25. A. Rahmimand, H. Zaidi, *Nucl. Med. Commun.*, 2008, **29**, 193 – 207.

26. S. R. Meikle, P. Kench, M. Kassiou, R. B. Banati, *Phys. Med. Biol.,* 2005, **50**, R45 – 61.

27. J. P. Holland, M. J. Williamson, J. S. Lewis, *Mol. Imaging.,* 2010, **9**, 1 – 20.

28. J. Donnard, W.-T. Chen, J.-P. Cussonneau, S. Duval, J. Lamblin, O. Lemaire, A. F. Mohamad Hadi, P. Le Ray, E. Morteau, T. Oger, L. Scotto Lavina, J.-S. Stutzmann, D. Thers, *Nucl. Med. Rev.,* 2012, **15**, C64 – C67.

29. T. Oger, W.-T. Chen, J.-P. Cussonneau, J. Donnard, S. Duval, J. Lamblin, O. Lemaire, A. F. Mohamad Hadi, P. Le Ray, E. Morteau, L. Scotto Lavina, J.-S. Stutzmann, D. Thers, *Nucl. Instrum. Methods,* 2012, **695**, 125.

30. E. Boros, C. L. Ferreira, J. F. Cawthray, E. W. Price, B. O. Patrick, D. W. Wester, M. J. Adam, C. Orvig*, J. Am. Chem. Soc.,* 2010, **132**, 15726 – 15733.

31. E. Boros, C. L. Ferreira, D. T. T. Yapp, R. K. Gill, E. W. Price, M. J. Adam, C. Orvig, *Nucl. Med. Biol.,* 2012, **39**, 785 – 794.

32. F. Vögtle, E. Buhleier, W. Wehner, *Synthesis*, 1978, 155 – 158.

33. S. Jurisson, D. Berning, W. Jia, D. Ma, *Chem. Rev.*, 1993, **93**, 1137 – 1156.

34. J. M. Oliveira, A. J. Salgadoc, N. Sousac, J. F. Manoa, R. L. Reis, *Prog. Polym. Sci.,* 2010, **35**, 1163 – 1194.

35. A. I. Kassis, H. Korideck, K. Wang, P. Pospisil, S. J. Adelstein, *Molecules*, 2008, **13**, 391 – 404.

36. P. Agrawal, N. K. Mehra, U. Gupta, N. K. Jain, *J. Drug Target,* 2013, **21**, 497 – 506.

37. C. C. Lee, J. A. MacKay, J. M. Fréchet, F. C. Szoka, *Nat Biotechnol*., 2005, **23**, 1517 – 1526.

38. L. J. Twyman, A. S. H. King, I. K. Martin, *Chem. Soc. Rev.*, 2002, **31**, 69 – 82.

39. H. Ma, A. K. Y. Jen, *Adv. Mater.,* 2001, **13**, 1201 – 1205.

40. D. A. Tomalia, H. Baker, J. R. Dewald, M. Hall, G. Kallos, S. Martin, J. Roeck, J. Ryder , P. Smith, *Polym. J.*, 1985, **17**, 117 – 132.

41. J. M. J. Frèchet, C. J. Hawker, *J. Am. Chem. Soc.,* 1990, **112**, 7638 – 7647.

42. P. Govender, B. Therrien, G. S. Smith, *Eur. J. Inorg. Chem*., 2012, 2853 – 2862.

43. S. Langereis, A. Dirksen, T. M. Hackeng, M. H. P. van Genderen, E. W. Meijer, *New J. Chem.*, 2007, **31**, 1152 – 1160.

44. Z.-X. Liu, Y. Feng, Z.-Y. Zhao, Z.-C. Yan, Y.-M. He, X.-J. Luo, C.-Y. Liu, Q.-H. Fan, *Chem. Eur. J.,* 2014, **20**, 533 – 541.

45. D. F. Baban, L. W. Seymour*, Adv. Drug Delivery Rev*., 1998, **34**, 109 – 119.

46. B. H. Zinselmeyer, S. P. Mackay, A. G. Schatzlein, I. F. Uchegbu, *Pharm. Res.,* 2002, **19**, 960 – 967.

47. N. Malik, R. Wiwattanapatapee, R. Klopsch, K. Lorenz, H. Frey, J. W. Weener, E. W. Meijer, W. Paulus, R. Duncan, *J. Controlled Release,* 2000, **68**, 299 – 302.

48. K. Rittner, A. Benavente, A. Bompard-Sorlet, F. Heitz, G. Divita, R. Brasseur, E. Jacobs, *Mol. Ther.,* 2002, **5**, 104 – 114.

49. K. Sadler, J. P. Tam, *J. Biotechnol.,* 2002, **90**, 195 – 229.

50. B. A. J. Jansen, J. van der Zwan, J. Reedijk, H. Den Dulk, J. Brouwer, *Eur. J. Inorg. Chem.,* 1999, 1429 – 1433.

51. D. I. Jodrell, T. R. J. Evans, W. Steward, D. Cameron, J. Prendiville, C. Aschele, C. Noberasco, M. Lind, J. Carmichael, N. Dobbs, G. Camboni, B. Gatti, F. De Braud, *Eur. J. Cancer*, 2004, **40**, 1872 – 1877.

52. M. Subbarayan, S. J. Shetty, T. S. Srivastava, O. P. D. Noronha, A. M. Samuel, H. Mukhtar, *Biochem. Biophys. Res. Commun*., 2001, **281**, 32 – 36.

53. H. B. Agashe, A. K. Babbar, S. Jain, R. K. Sharma, A. K. Mishra, A. Asthana, M. Garg, T. Dutta, N. K. Jain, *Nanomed.:Nanotechnol., Biol. Med.,* 2007, **3**, 120 – 127.

54. M. C. Parrott, S. R. Benhabbour, C. Saab, J. A. Lemon, S. Parker, J. F. Valliant, A. Adronov, *J. Am. Chem. Soc.*, 2009, **131**, 2906 – 2917.

55. S. Hecht, J. M. J. Frèchet, *Angew. Chem., Int. Ed*., 2001, **40**, 74 – 91.

56. Y. Zhang, X. Xu, Y. Sun, Y. M. Shen, *Chin. J. Chem*., 2010, **28**, 2447 – 2450.

57. Y. Zhang, Y. Sun, X. Xu, X. Zhang, H. Zhu, L. Huang, Y. Qi, Y. M. Shen, *J. Med. Chem*., 2010, **53**, 3262 – 3272.

Chapter 2

Synthesis and characterization of monomeric and dendritic bipyridyl (bpy) and picolyl ligands

2.1. General introduction

Current research in the area of technetium-99m (^{99m}Tc) is focused towards developing diagnostic radiopharmaceuticals that preferentially localize in tumour tissues. The 'vehicle' that carries the radiotracer to the target site is normally a 'targeting biomolecule', with the ability to accumulate in neoplastic tissues with high specificity and affinity.[1] Dendrimers as 'vehicles' offer possible enhanced targeting efficiency as a result of their proposed mechanism of action *via* the 'enhanced permeability and retention' (EPR) effect, a phenomenon in which macromolecules accumulate at the tumour site by virtue of an increase in blood vessel permeability within diseased tissues compared to healthy tissue.[2] Their multivalent system of tuneable and controlled size permits complexation of diverse metallic ions often resulting in enhanced biological activity compared to their mononuclear counterparts.[3-7] Such improved activities are attributed to the lipophilicity, solubility and favourable modulation of the stability of the organometallic dendritic complexes.[7]

Since radiotracers are utilized at nanoMolar to picoMolar concentration, the multivalent nature of a dendrimer is likely to permit increased interactions between a dendrimer-radiotracer complex and a cellular target bearing multiple receptors.[8] This may result in enhanced sensitivity of an imaging modality (SPECT scan for ^{99m}Tc). Since the biocompatibility and cytotoxicity of different generations of the diaminobutane poly(propylene amine) (DAB-PPI) dendrimer have been reported before[9], herein, we report the synthesis and characterization of DAB-PPI dendritic scaffolds modified at the periphery

with *N,N'*-bidendate donor moieties. These ligands will serve as chelates to 'cold' rhenium(I), *fac*-$[Re(CO)_3]^+$ isomer , and 'hot' *fac*- $[^{99m}Tc(CO)_3]^+$ adducts for application as potential nuclear imaging agents (in the case of ^{99m}Tc).

The monomeric analogues were synthesized as mononuclear models of the larger dendritic ligands. The monomeric and dendritic ligands were characterized using various spectroscopic and analytical techniques.

2.2. Synthesis and characterization of 4'-methyl-2,2'-bipyridine-4-carboxaldehyde

Govender *et al*. reported on polypyridyl grafted DAB-PPI dendritic scaffolds chelating manganese(I) tricarbonyl moieties at the periphery, as new photoactivated CO-releasing molecules (PhotoCORMs).[10] At the periphery, their first and second generation PPI dendritic scaffolds were primarily functionalized with imino conjugated bipyridyl (bpy) moieties *via* a Schiff condensation reaction.[10] 2,2'-Bipyridyl chelates are known to form inert complexes with various transition metals and exhibit favourable photochemistry, photophysical, and chemiluminescence properties when coordinated to transition metals such as Ru, Os and Re.[11-15] In the current study, a series of 2,2'-bipyridyl functionalized dendritic scaffolds were synthesized, as potential 'cold' Re(I) and $^{99m}Tc(I)$ chelates, for application in nuclear medicine.

The synthetic strategy adopted for the preparation of amino conjugated bipyridyl moieties on PPI dendrimers involved 4'-methyl-2,2'-bipyridine-4-carboxaldehyde as the synthetic intermediate, a convenient way of introducing functionalized side chains to 2,2'-bipyridyl moieties. The functional group transformation of 4,4'-dimethyl-2,2'-bipyridine involved partial oxidation of one of the methyl group substituents on the bpy ring using selenium

dioxide, SeO_2 (**Scheme 2.1**).[16-18] This oxidation reaction inefficiently permits optimal conversion of the starting material to the desired product since more than 60% of 4,4'-dimethyl-2,2'-bipyridine is recovered after work-up. In order to isolate 4'-methyl-2,2'-bipyridine-4-carboxaldehyde from the starting material, 0.3 M $Na_2S_2O_5$ was used to protect 4'-methyl-2,2'-bipyridine-4-carboxaldehyde formyl group by converting it to a bisulfite adduct, a common industrial procedure for the storage of aldehydes. Under alkaline conditions at pH 10, the bisulfite adduct reverts to the desired deprotected formyl form.[16,17] SeO_2 is a milder oxidizing agent than potassium permanganate ($KMnO_4$), thus, over-oxidation of the methyl groups to form undesired (di)carboxylic acid side product(s) is negligible.[18]

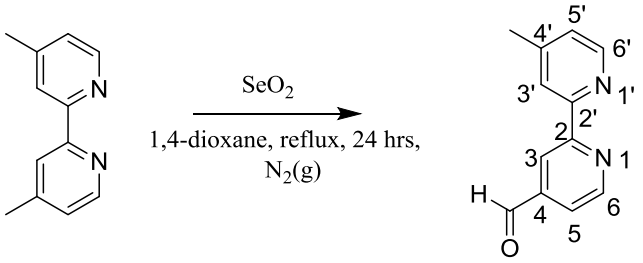

4'-Methyl-2,2'-bipyridine-4-carboxaldehyde

Scheme 2.1: Oxidation of a 4-methyl substituent using selenium dioxide to afford 4'-methyl-2,2'-bipyridine-4-carboxaldehyde in a 29% yield.[16,17]

The compound 4'-methyl-2,2'-bipyridine-4-carboxaldehyde was achieved in 29% yield. The reaction scheme is illustrated in **Scheme 2.1**. 4'-Methyl-2,2'-bipyridine-4-carboxaldehyde was isolated as a white solid and is soluble in polar organic solvents such as dichloromethane (CH_2Cl_2), acetone $(CH_3)_2CO$, chloroform ($CHCl_3$) and dimethylsulfoxide $(CH_3)_2SO$. The melting point range of 4'-methyl-2,2'-bipyridine-4-carboxaldehyde is between 130.2 – 132.0 °C and corresponds accordingly with the reported literature melting point values, 130.9 – 131.7 °C.[16]

The ^{1}H NMR spectrum of 4'-methyl-2,2'-bipyridine-4-carboxaldehyde features a singlet at 10.2 ppm integrating for one proton and is assigned to the formyl functional group at the C4 position, **Figure 2.1**. The upfield singlet resonance at 2.59 ppm integrates for three protons and corresponds to the methyl substituent at the C4' position.

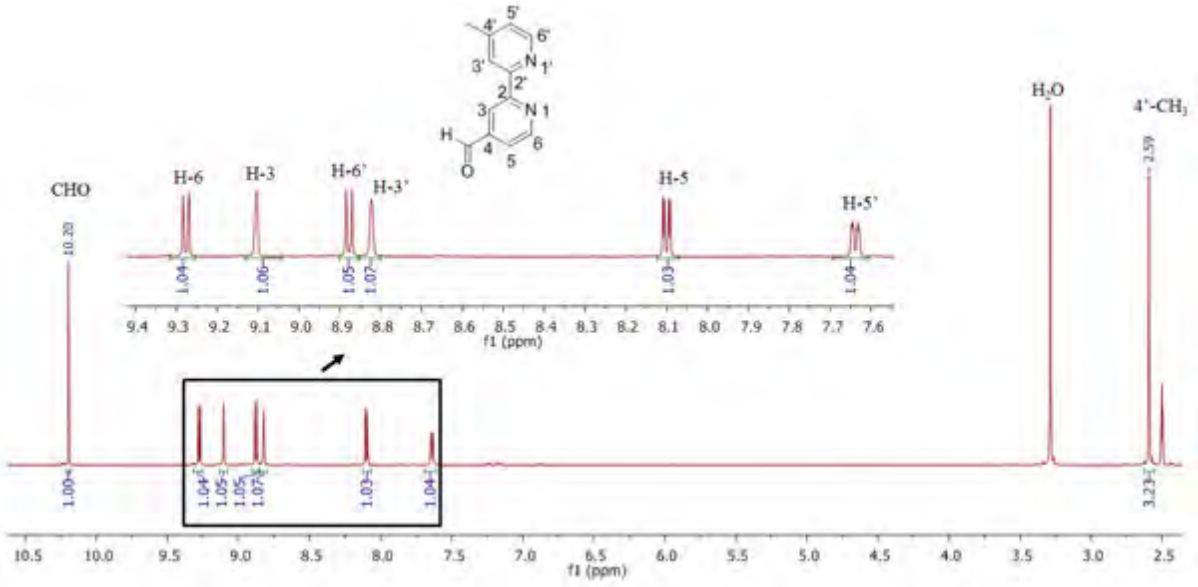

Figure 2.1: ^{1}H NMR spectrum of 4'-methyl-2,2'-bipyridine-4-carboxaldehyde in $(CD_3)_2SO$ with the expansion of the aromatic region.

The $^{13}C\{^{1}H\}$ NMR spectrum displays the formyl carbonyl carbon resonance of 4'-methyl-2,2'-bipyridine-4 at 193.4 ppm. In the IR spectrum, a sharp absorption band at 1705 cm^{-1} is observed, characteristic of α,β-unsaturated aldehyde stretching vibration which is in close proximity with the reported literature absorption band at 1709 cm^{-1}, further confirming the presence of a formyl group.[16,17] The additional IR absorption bands at 1594 and 1557 cm^{-1} are attributed to the C=N bonds present in the bpy ring.

The elemental analysis output of 4'-methyl-2,2'-bipyridine-4-carboxaldehyde gave C, N and H values as 72.1, 5.10 and 14.6%, respectively. These values are comparable to the calculated values for this compound. The structural integrity of the compound is supported by the EI-

MS spectrum featuring a molecular ion peak at *m/z* = 198.00 $[M]^+$. These results are in accordance with the reported literature values.[19]

2.3. Synthesis and characterization of *N,N'*-bipyridyl functionalized monomeric and dendritic bidentate ligands L1, L2, and L3

The generation 1 and generation 2 DAB-PPI dendritic scaffolds were functionalized at the periphery with 4'-methyl-2,2'-bipyridine-4-carboxaldehyde *via* a reductive amination reaction (the reaction mechanism is shown in **Scheme 2.2 (a)**), to afford reduced poly(pyridyl) functionalized dendritic ligands **L2** and **L3** (**Scheme 2.2 (b)**).

The pure monomeric analogue *N*-((4'-methyl-2,2'-bipyridin-4-yl)methyl)propan-1-amine (**L1**) was synthesized by condensation between *N*-propylamine and 4'-methyl-2,2'-bipyridine-4-carboxaldehyde (**Sheme 2.2 (b)**), followed by reduction with sodium borohydride ($NaBH_4$) to generate **L1**.[14,20] A similar synthetic procedure was used to synthesize the ligands **L2** and **L3** (**Scheme 2.2**).

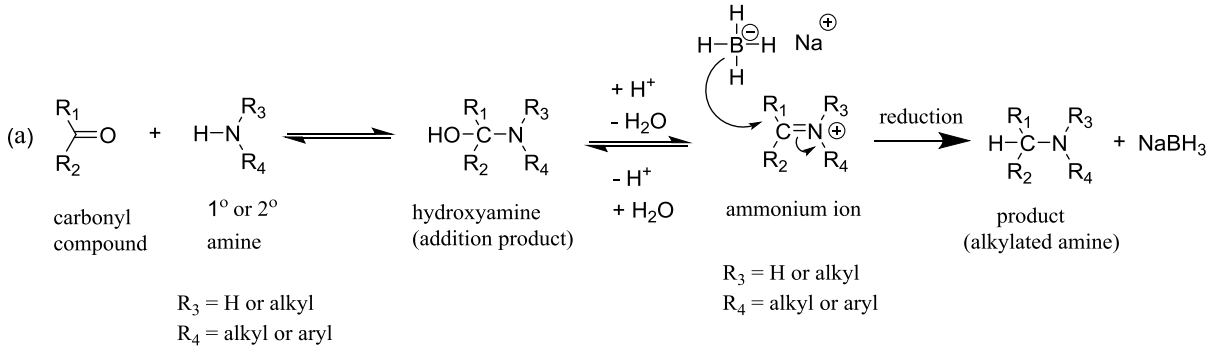

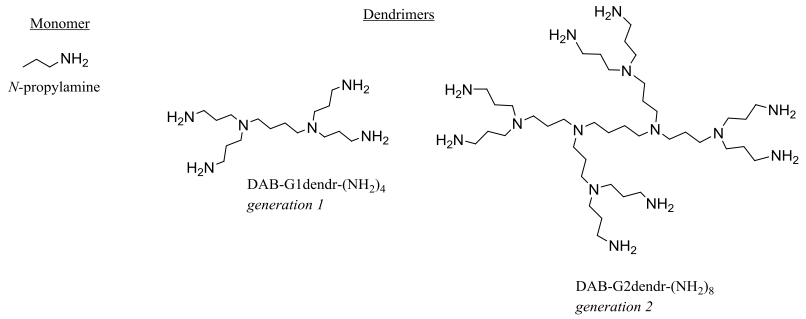

Scheme 2.2: **(a)** The proposed reductive amination reaction mechanism (of the carbonyl compound) or reductive alkylation (of the amines).[20]

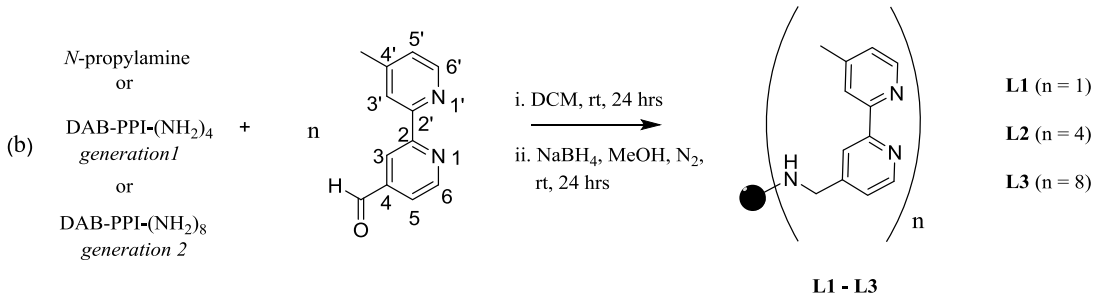

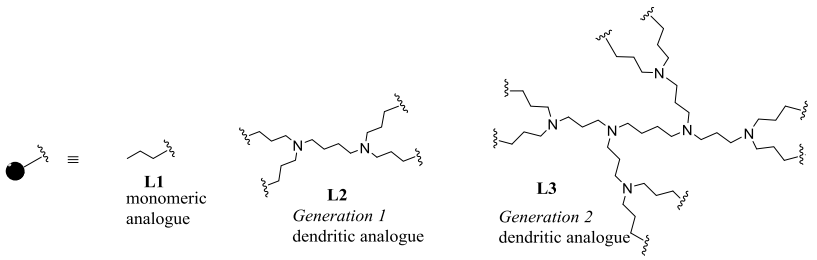

Scheme 2.2: (b) Synthesis of the monomeric and dendritic ligands **L1 – L3** *via* the reductive amination of *N*-propylamine, DAB-G1dendr-$(NH_2)_4$ and DAB-G2dendr-$(NH_2)_8$ with 4'-methyl-2,2'-bipyridine-4-carboxaldehyde in a one-pot reaction using literature method.[14,20]

The dendritic ligands **L2** and **L3** were isolated as yellow oils and were synthesized in a 54.9 and 71.4% yield, respectively. **L2** and **L3** readily dissolve in polar organic solvents such as $(CH_3)_2CO$, CH_2Cl_2, CH_3Cl, hot MeOH and $(CH_3)_2SO$. The monomeric analogue **L1** was isolated as a yellow oil in 57.2% yield and dissolves in polar organic solvents similar to **L2** and **L3**. **L1** serves as a model in characterization of the dendritic analogues. **L1 – L3** were found to be stable at room temperature and in the presence of light. The ligands were characterized by ^{1}H NMR, $^{13}C\{^{1}H\}$ NMR, FT-IR spectroscopy, elemental analysis, and mass spectrometry.

2.3.1. ^{1}H and $^{13}C\{^{1}H\}$ NMR spectroscopy

The ^{1}H and $^{13}C\{^{1}H\}$ NMR data were recorded in $(CD_3)_2SO$. **Figure 2.2** represents the ^{1}H NMR spectrum of **L1** which was easily interpreted by comparison with the work by Massing *et al.*[14] and Yao *et al.*[20] In the aliphatic region between 0.85 – 2.51 ppm, four signals are observed, which correspond to the protons of the methyl group at C4' position and to the aliphatic protons on the *N*-propyl side chain ($CH_3CH_2CH_2NH$).

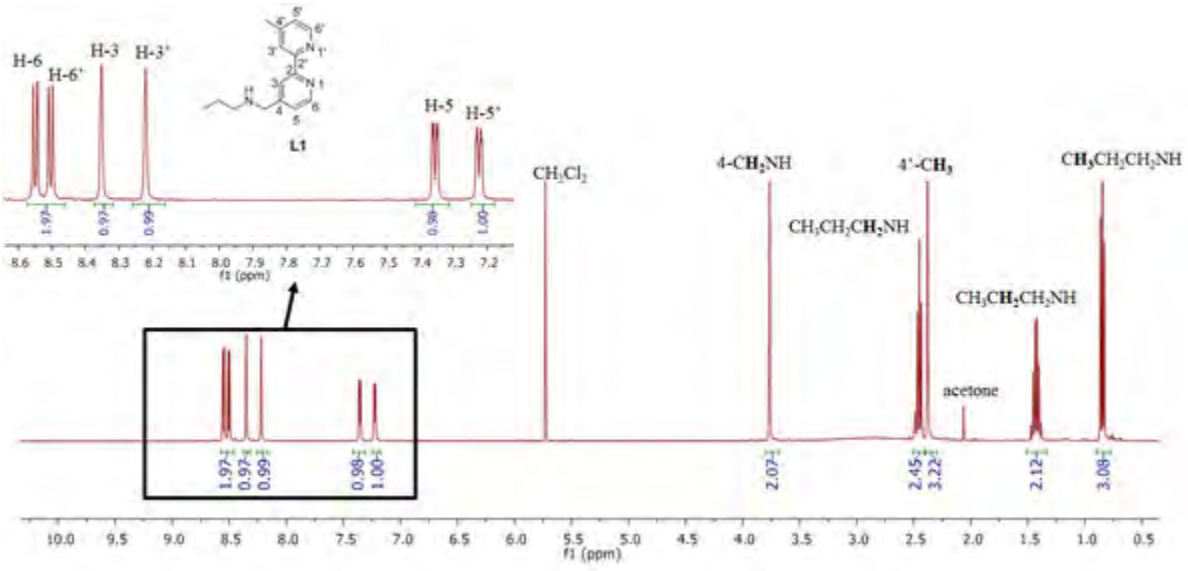

Figure 2.2: ^{1}H NMR spectrum of the monomeric ligand **L1** in $(CD_3)_2SO$. The black square accentuates the magnified aromatic region.

A singlet signal at 3.77 ppm integrating for two protons is assigned to the protons of a newly formed methyl **(**4-C**H$_2$**NH**)** group, adjacent to the quaternary carbon on the bipyridyl ring at C4 position (**Figure 2.2**). The ^{1}H NMR spectrum of 4'-methyl-2,2'-bipyridine-4-carboxaldehyde (**Figure 2.1**) illustrates the signals for the 2,2'-bipyridyl aromatic protons between 9.28 – 7.64 ppm, whereas, in the ^{1}H NMR spectrum of **L1**, the aromatic protons of the 2,2'-bipyridyl ring exist within the 8.56 – 7.24 ppm range. The upfield shift of **L1** aromatic proton signals in the aromatic region, **Figure 2.2**, may be reasoned through inductive contributions from the newly formed methyl bond at C4 position.[14] In **Figure 2.2**, the most deshielded protons at 8.51 ppm (H-6') and 8.56 ppm (H-6) are a result of the resonance effect in pyridine rings which renders 2/6 positions as electrophilic sites.

In **Figure 2.3** is the 2D HSQC ^{13}C – ^{1}H correlation spectrum of **L1** in $(CD_3)_2SO$, the peaks at the vertical axis (F1) correspond to the $^{13}C\{^1H\}$ signals of **L1**.

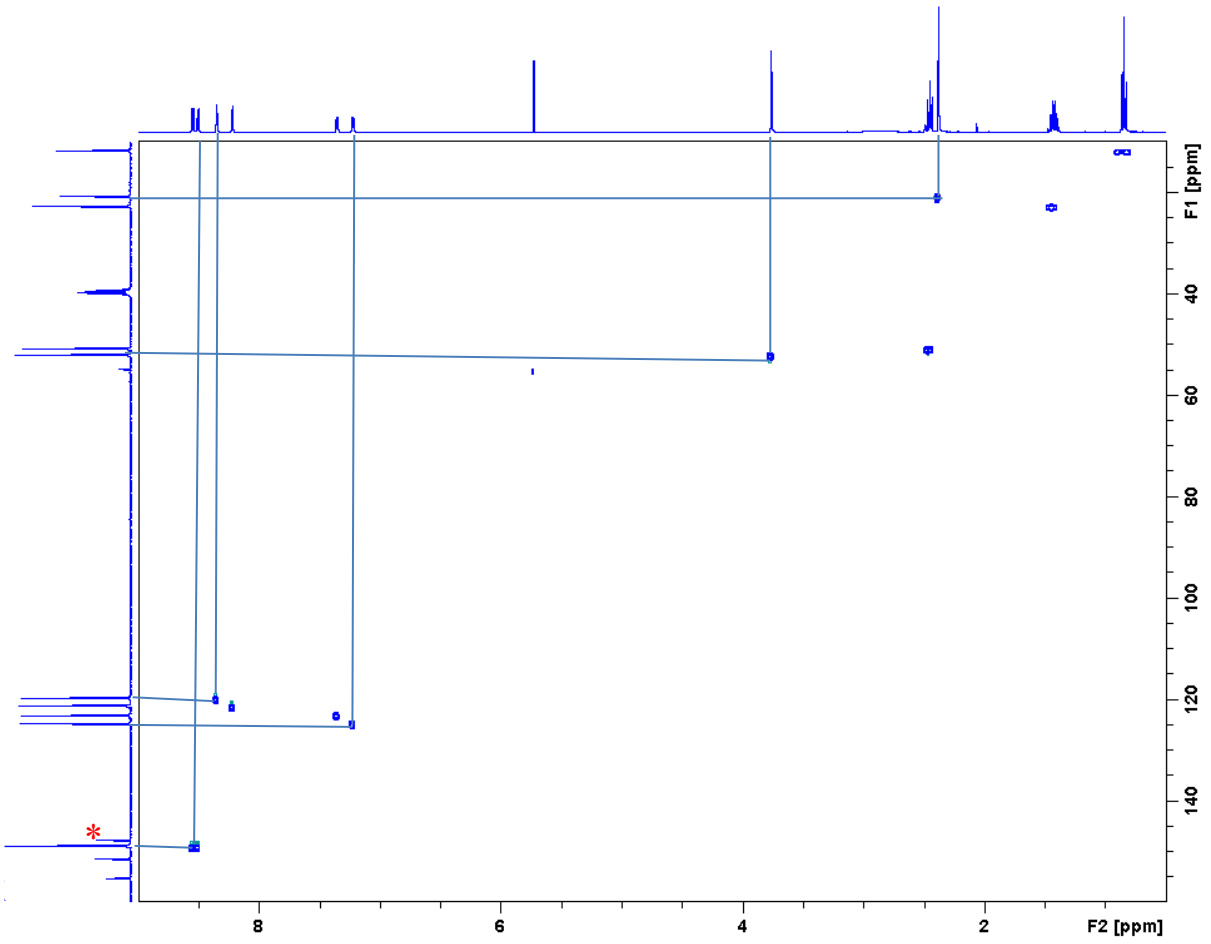

Figure 2.3: The 2D HSQC spectrum of **L1** in $(CD_3)_2SO$. The blue lines correlate the corresponding C-H nuclei. Peak assignments in F2 correspond to ***Figure 2.2***.

The 4'-**C**H_3 carbon atom adjacent to the bipyridyl ring at C4' position is at 21.0 ppm more deshielded than the terminal **C**H_3 group of the *N*-propyl side chain at 11.7 ppm. The resulting methyl (4-**C**H_2NH) carbon atom adjacent to the bipyridyl ring at C4' position is represented by a signal at 51.9 ppm. To confirm the isolation of a pure product, the $^{13}C\{^1H\}$ NMR signal characteristic of the 4'-methyl-2,2'-bipyridine-4-carboxaldehyde carbonyl carbon atom is not observed. The quaternary carbon **C**4 initially at 156.9 ppm—as a result of the formyl electron withdrawing effect in 4'-methyl-2,2'-bipyridine-4-carboxaldehyde—shifts to 148.7 ppm (**Figure 2.3**, F1 axis, asterisk) in **L1**, confirming the integrity of the reductive amination product. The 2,2'-bipyridyl ring tertiary carbon atoms resonate between 119.6 – 148.8 ppm. In the 2D HSQC ^{13}C – ^1H correlation spectrum of **L1**, the 2,2'-bipyridyl ring quaternary

carbon atoms are represented by four medium intensity peaks downfield between 148.7 – 155.3 ppm (**C**2, **C**2', **C**4 and **C**4') and there is a signal overlap corresponding to **C**2/**C**2' at 155.3 ppm.

Figure 2.4 displays the ^{1}H NMR spectrum of the dendritic ligand **L2** (generation 1 dendrimer). The ^{1}H NMR spectra of the dendrimers **L2** and **L3** have the aliphatic protons between 1.25 – 3.25 ppm assigned to the dendritic core (diaminobutane) and branches (polypropyl chains). In the ^{1}H NMR spectrum of the dendritic ligands, a singlet resonance, assigned to the 4-C**H**$_2$NH (adjacent to the bipyridyl ring) methyl protons, at 3.68 ppm and 3.67 ppm for **L2** and **L3**, respectively, integrates for two protons and confirms the presence of the amino group (as opposed to the imino group by Govender *et al*).[10] The aromatic proton resonances observed in **L1** ^{1}H NMR spectrum (**Figure 2.2**, magnified region) resonate in the same region as the aromatic protons of the dendritic analogues **L2** (**Figure 2.4**) and **L3**.

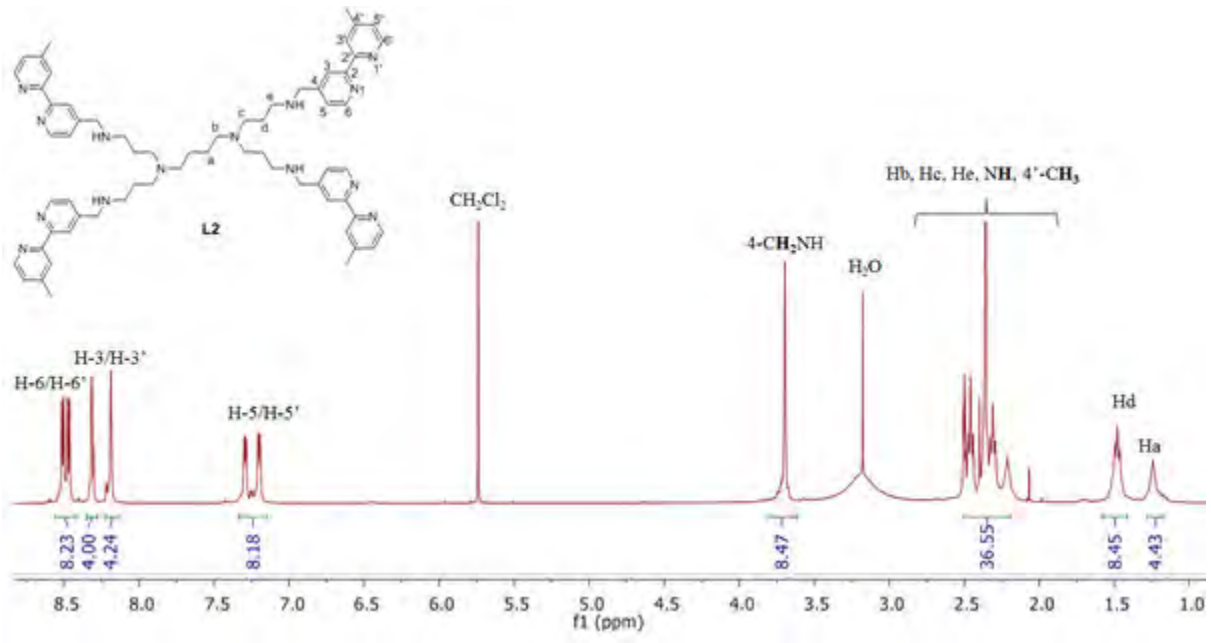

Figure 2.4: ^{1}H NMR spectrum of **L2** in $(CD_3)_2SO$.

In the $^{13}C\{^{1}H\}$ NMR spectra, the aliphatic carbon atoms are between 20.4 – 53.3 ppm and the aromatic carbon atoms are in the region of 119.5 – 155.2 ppm for both generations **L2** and **L3**.

2.3.2. Infrared spectroscopy

The infrared spectra of **L1 – L3** were recorded in Nujol oil using sodium chloride plates. Two distinct sharp absorption bands in the region of 1554 – 1597 cm^{-1}, attributed to the $\nu_{C=N}$ bond of the bipyridyl ring, are observed in all ligands. The absence of a diagnostic imine absorption band between $\nu_{C=N}$ ~1650 – 1648 cm^{-1} infers a successful reductive amination reaction.

2.3.3. Elemental analysis and mass spectrometry

Dendrimers are known to encase solvent molecules and chelate inorganic salts. Supported by the ^{1}H NMR spectra of **L1 – L3**, the elemental analysis data for the dendritic ligands **L2** and **L3** were discovered to include CH_2Cl_2 and MeOH molecules, respectively. The calculated values for C, H and N atoms, with inclusion of solvent molecules, correlate with the found values. As per EI-MS analysis, a base peak of *m/z* = 184.00 (calculated mass for [M – $CH_3CH_2CH_2NH]^+$ *m/z* = 184.10, where $CH_3CH_2CH_2NH$ corresponds to the *N*-propyl-1-amine chain of **L1** in **Figure 2.2**). The HR-ESI-MS analysis of ligands **L2** and **L3** ionized adducts have prominent peaks corresponding to *m/z* = 1045.6774 (calculated mass for [M + $H]^+$ *m/z* = 1045.6769) and *m/z* = 752.0718 (calculated mass for [M + 2H+ $Na]^{3+}$ *m/z* = 752.0393), respectively.

2.4. Synthesis and characterization of *N,N'*-picolyl functionalized monomeric and dendritic bidentate ligands L4, L5 and L6

Picolyl amines and their derivatives are known copper chelators.[22-25] Such compounds can be synthesized by reacting α, β or γ-pyridinecarboxaldehydes with various alkyl secondary amines, *via* a reductive amination reaction (**Scheme 2.2a**).[25,26] The basic nature of picolyl alkyl amines resembles that of naturally occurring class of alkaloids of different biochemical and botanical origin.[27] Bandyopadhyay *et al*. synthesized and reported on several picolyl alkyl amine derivatives to confer inhibitory activity towards tyrosinase (EC 1.14.18.1), a copper-containing polyphenol oxidase responsible for the enzymatic browning of fruits and vegetables.[25]

Govender *et al*. reported on a series of periphery functionalized, cationic and neutral PPI metallodendrimers, with *N,N'*-picolyl imine moieties (*via* a Schiff base condensation reaction) coordinated to ruthenium(II)-arene groups.[4] In the current study, complexation reactions using similar dendritic ligands resulted in the hydrolysis of the imine bond. The imine bond was significantly cleaved at high temperatures (during complexation reactions). Therefore, a reductive amination reaction was used to achieve ligands **L4 – L6** (**Scheme 2.3**). Using a similar synthetic approach to **L1 – L3**, *N*-propylamine was reacted with 2-pyridinecarboxaldehyde to afford the monomeric α-picolyl alkyl amine, *N*-((pyridine-2-yl)methyl)propan-1-amine (**L4**), in the presence of $NaBH_4$ as the reducing agent.[25,26] The dendritic ligands **L5** and **L6** were synthetized analogous to the monomer **L4**.

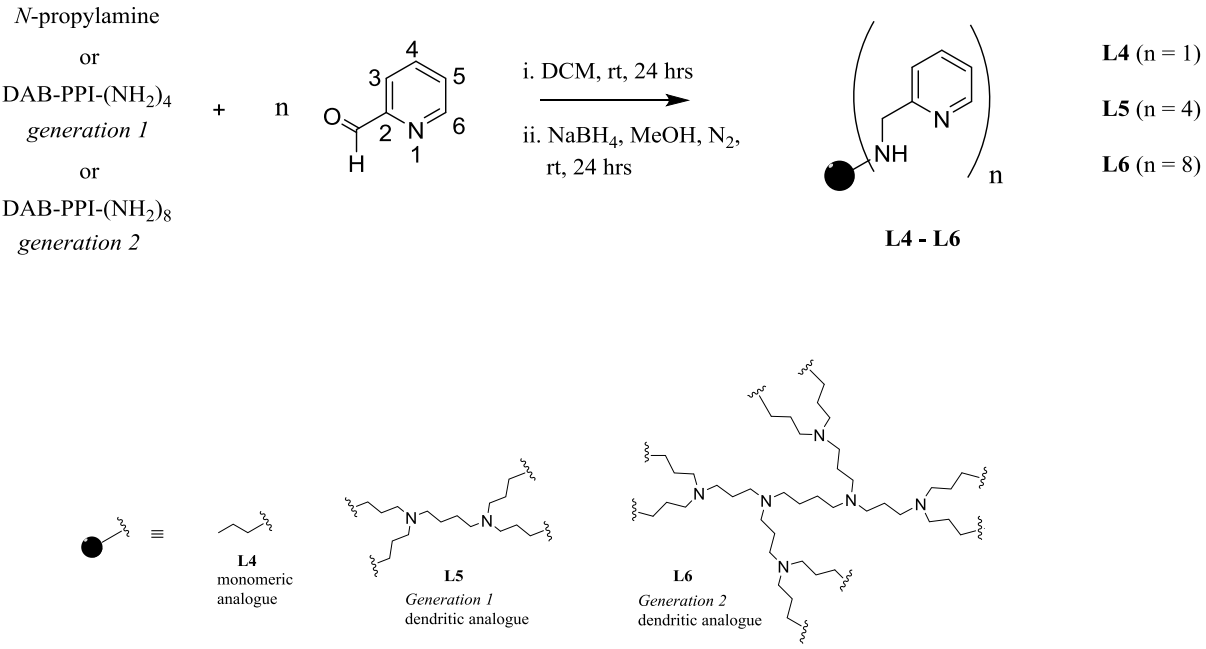

Scheme 2.3: Synthesis of the monomeric and dendritic ligands **L4 – L6** by reacting 2-pyridinecarboxaldehyde with either *N*-propylamine, DAB-G1dendr-$(NH_2)_4$ or DAB-G2dendr-$(NH_2)_8$ in a one-pot reaction.

The picolyl alkyl amine **L4** is a yellow liquid and the dendritic ligands **L5 –L6** are brown oils, the ligands were isolated in 30.0 – 44.0% yield. **L4 – L6** are soluble in water and polar organic solvents. Apart from the water solubility, these ligands exhibit relative spectroscopic features to the bipyridyl ligands **L1 – L3**, omitting one pyridine ring. The ligands **L4 – L6** were characterized by ^{1}H NMR, ^{13}C{^{1}H} NMR, FT-IR spectroscopy, elemental analysis, and mass spectrometry.

2.4.1. ^{1}H and ^{13}C{^{1}H} NMR spectroscopy

The ^{1}H NMR spectrum of **L4**, in **Figure 2.5**, has a singlet resonance at 3.76 ppm assigned to the methyl protons at the α-position of the pyridine ring. This confirms the formation of an amine bond contrary to the imine derivatives synthesized by Govender *et al*.[4] Also, the diagnostic singlet resonance for the methyl protons (at the α-position of the pyridine ring) is present in the ^{1}H NMR data reported in the literature for **L4** in deuterated chloroform.[25,26]

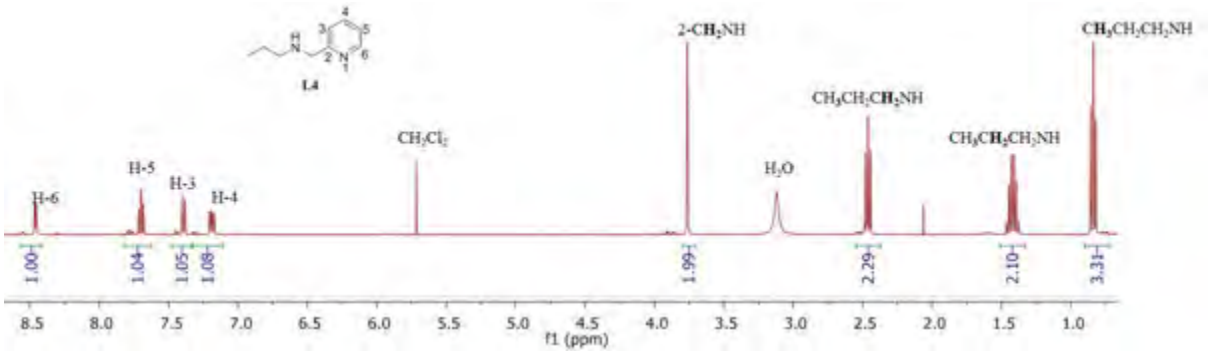

Figure 2.5: ^{1}H NMR spectrum of **L4** in $(CD_3)_2SO$.

In the ^{1}H NMR spectrum of **L4**, the aromatic region between 8.50 – 7.00 ppm corresponds to the aromatic protons of the picolyl ring, with H-6 being the most deshielded proton at 8.46 ppm, as a result of the resonance effect of the pyridine ring.[26] The alkyl amine side chain (*N*-propan-1-amine) is shielded occurring upfield in the region between 2.50 – 0.80 ppm of the spectrum. The ^{1}H NMR spectra of the dendritic ligands **L5** and **L6** only deviate from **Figure 2.5** in the upfield aliphatic region as their spectra feature the dendrimer framework aliphatic protons. **Figure 2.6** displays the ^{1}H NMR spectrum of **L5** which features the overlapping dendrimer framework aliphatic proton resonances in the region between 1.25 – 3.00 ppm, integrating for 32 protons.

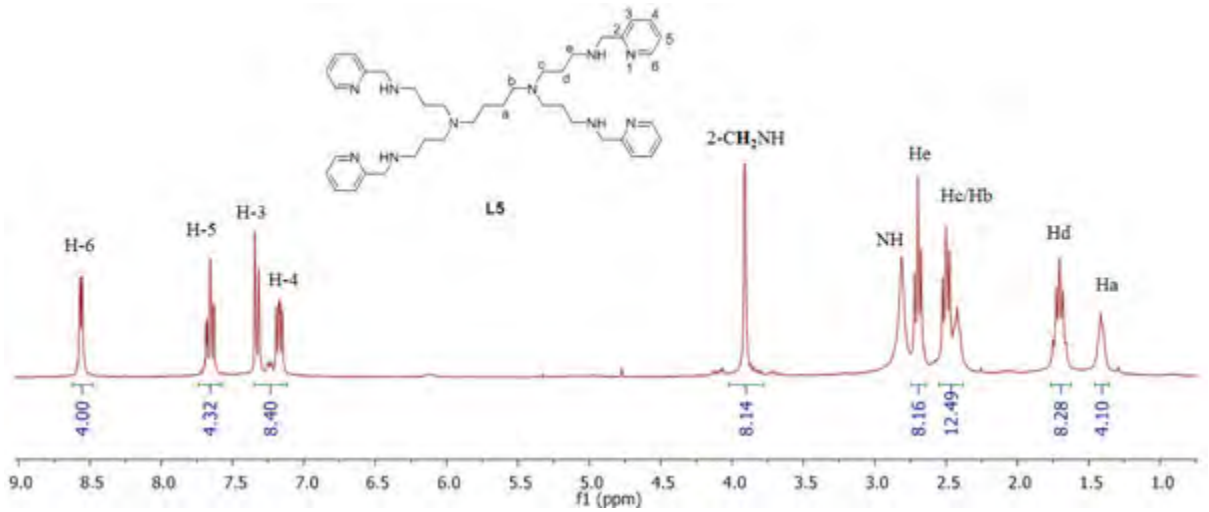

Figure 2.6: ^{1}H NMR spectrum of **L5** in $(CD_3)_2SO$.

In addition to the aliphatic and aromatic carbon peaks, the $^{13}C\{^{1}H\}$ NMR spectra of **L4 – L6** display a peak between 54.5 – 55.0 ppm which corresponds to the 2-**C**H_2NH (adjacent to C2) methyl carbon atom at the α-position of the pyridine ring.

2.4.2. Infrared spectroscopy

In addition to the ^{1}H and $^{13}C\{^{1}H\}$ NMR spectra, a sharp absorption band at ~1590 cm^{-1} is observed in the IR spectra of **L4 – L6** and is attributed to the pyridyl C=N bond. Furthermore, a sharp absorption band at ~1377 cm^{-1} is observed and is attributed to the secondary amine C-N bond.

2.4.3. Elemental analysis and mass spectrometry

The elemental analysis data of **L4 – L6** are within the expected values. The EI-MS of **L4** shows a base peak *m/z* = 93.03 ($[M - CH_3CH_2CH_2NH)^+$] (where $CH_3CH_2CH_2NH$ corresponds to the *N*-propane-1-amine moiety of **L4** in **Figure 2.5**). The ligands **L5** and **L6** HR-ESI-MS base peaks are prominent at *m/z* = 341.2581 ($[M + 2H]^{2+}$) and *m/z* = 376.2898 ($[M + 4H]^{4+}$), respectively.

2.5. Summary

A series of monomeric and dendritic poly(propylene amine) ligands, **L1 – L6**, functionalized with either *N,N'*-bipyridyl or *N,N'*-picolyl bidentate moieties have been successfully synthesized *via* a reductive amination reaction. Characterization of these ligands was done using spectroscopic (1D and 2D ^{1}H NMR, $^{13}C\{^{1}H\}$ NMR, infrared spectroscopy and mass spectrometry) and analytical (elemental analysis) methods. The NMR spectra peak assignment of the dendritic scaffolds was comparable to the spectra of the monomeric analogues. Interestingly, the first and second generation dendritic ligands **L5** and **L6** were discovered to be water-soluble (0.01 mg/μL). In the literature, water-soluble dendrimers such as oligoethyleneoxy- modified poly (propylene amine) (POMAM) have been demonstrated to

encapsulate hydrophilic xathene dyes, accentuating the unlimited possibilities of dendrimer binding behaviour.[28] The complexation of such ligands with trace amounts of therapeutic or diagnostic metals will contribute towards the research of PPI-based dendritic architectures as drug delivery vehicles.

2.6. Experimental

2.6.1. Chemical reagents

All reagents were purchased from Sigma-Aldrich and used without further purification. 1,4-Diaminobutane poly(propylene amine) octaamine (DAB-PPI-$(NH_2)_8$) was purchased from SyMO-Chem. All reactions were performed at room temperature using standard Schlenk-line techniques, and the reductive amination reactions were performed under nitrogen line. Dichloromethane (CH_2Cl_2) was dried using the molecular sieves (Sigma Aldrich, 3Å beads, 4 – 8 mesh) and methanol (MeOH) was dried in the Innovative Technology Swagelok® (PS-Micro, PSM-13-564).

2.6.2. Purification

Purification was carried out using deionized water and column chromatography Biotage-KP-C_{18}-HS, where stated.

2.6.3. Spectroscopic and analytical methods

Nuclear magnetic resonance (NMR) spectra were recorded on a Bruker Ultrashield 400 Plus spectrometer (^{1}H: 399.95 MHz; ^{13}C{^{1}H}: 100.60 MHz) at ambient temperature. All chemical shifts are reported in the standard δ notation of parts per million using tetramethylsilane (TMS) as an internal standard and were referenced relative to the signal of correspondinig deuterated solvents. The *J* coupling constants are reported in Hertz (Hz). Spin multiplicities are reported in abbreviated conventional format.

Infrared (IR) absorption bands were measured on a Perkin-Elmer spectrum 100 FT-IR Nujol oil. Melting points were determined on a Reichert-Jung Thermovar hot-stage microscope and are uncorrected. Elemental analysis were performed using Thermo Flash EA 112 Series combustion analyser. Electrospray Ionisation (ESI+) mass spectra were recorded on a Waters

API Quattro Micro triple quadrupole mass spectrometer by courtesy of the University of Stellenbosch. Furthermore, Electron impact mass spectrometry (EI-MS) was carried out on a JEOL GCmateII mass spectrometer.

2.6.4. Synthesis and characterization of *N,N'*-bipyridyl ligands

2.6.4.1. Preparation of 4'-methyl-2,2'-bipyridine-4-carboxaldehyde[16,17]

SeO_2 (3.31 g, 29.9 mmol) was added to a stirring solution of 4,4'-dimethly-2,2'-bipyridine (5.00 g, 27.1 mmol) in 1,4 dioxane (150 mL) and refluxed for 36 hours under nitrogen. The reaction mixture was filtered hot through a Celite pad and the solvent of the filtrate was removed by rotary evaporation to give an amorphous residue. The residue was suspended in EtOAc (3 × 50.0 mL), the organic fractions combined, and filtered by gravity. The filtrate was washed with 1M Na_2CO_3 (2 × 100 mL) and the organic layer subsequently washed with 0.3 M $Na_2S_2O_5$ (3 × 100 mL) to form a bisulfide adduct. The combined aqueous extracts were adjusted to pH 10 with Na_2CO_3 and the desired product extracted with CH_2Cl_2 (4 × 100 mL). The combined organic fractions were dried over $MgSO_4$, filtered and evaporation of the solvent of the filtrate afforded 4'-methyl-2,2'-bipyridyl-4-carboxaldehyde.

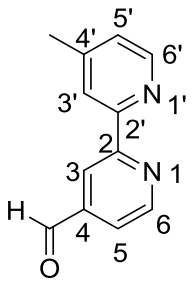

4'-Methyl-2,2'-bipyridyl-4-carboxaldehyde: White solid, yield: 1.54 g (28.7%). **IR**: KBr pellets, ν/cm^{-1}: 1705 (sharp, aldehyde, CO), 1594, 1557 (sharp, bipyridyl, C═N). **^{1}H NMR** (400.22 MHz, $(CD_3)_2SO$): δ 2.59 (s, 3H, 4'-CH_3), 7.64 (d, 1H, ^3J = 5.64 Hz, H-5'), 8.10 (dd, 1H, ^4J = 1.60 Hz, ^3J = 5.60 Hz, H-5), 8.82 (s, 1H, H-3'), 8.88 (d, 1H, ^3J = 5.68 Hz, H-6'), 9.10

(s, 1H, H-3), 9.28 (d, 1H, ^{3}J =5.4 Hz, H-6), 10.20 (s, 1H, HCO). **^{13}C{^{1}H} NMR** (100.60 MHz, $(CD_3)_2SO$): δ = 20.7 (CH_3), 119.4 (C-3), 121.4 (C-5), 121.9 (C-3'), 125.5 (C-5'), 142.6 (C-4'), 148.3 (C-2') 149.2 (C-6'), 150.7 (C-6), 154.1 (C-2), 156.9 (C-4), 193.4 (CHO). **Elemental analysis** (%): Calc. For $C_{12}H_{10}N_2O$ (198.2): C, 72.71; H, 5.09; N, 14.13; Found: C, 72.10; H, 5.10; N, 14.62. **Mp**: 130.2 – 131.9 °C. **MS** (EI; *m/z*): 198.00 $[M]^+$.

2.6.4.2. Preparation of *N*-((4'-Methyl-2,2'-bipyridin-4-yl)methyl)propan-1-amine (L1)[14,20]

To a stirring solution of 4'-methyl-2,2'-bipyridyl-4-carboxaldehyde (0.0447 g, 0.760 mmol)) in dry CH_2Cl_2 (30.0 mL), *N*-propylamine (0.0622 mL, 0.760 mmol) was syringed into the flask dropwise. In addition, $MgSO_4$ (0.150 g) was introduced to the mixture. After stirring at room temperature for 24 hours, the reaction mixture was filtered by gravity and the solvent of the filtrate was removed by rotary evaporation to afford a yellow oil. The crude oil was dissolved in MeOH (30.0 mL) and stirred for 30 minutes, under nitrogen. Thereafter, $NaBH_4$ (0.0333 g, 0.876 mmol) was added to the stirring solution and the reaction proceeded overnight at room temperature under nitrogen. The reaction mixture was cooled in an ice bath and the excess hydride was quenched with ice cooled water (30.0 mL). The azeotropic mixture was reduced by rotary evaporation to afford an aqueous mixture. The desired product was extracted with CH_2Cl_2 (40.0 mL). The organic layer was then washed with H_2O (3 × 50.0 mL) and dried over anhydrous $MgSO_4$. Subsequently, $MgSO_4$ was filtered and rinsed with CH_2Cl_2 (2 × 15.0 mL). The solvent of the filtrate was removed by rotary evaporation to afford a pale yellow oil, **L1**, which was dried *in vacuo*.

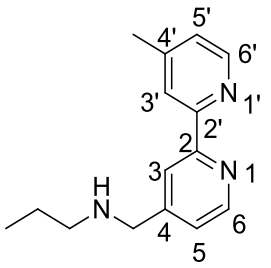

L1

Compound **L1**: Light yellow oil, yield: 0.105 g (57.2%). **IR**: Nujol between NaCl plates, ν/cm^1 = 1597, 1556 (sharp, bipyridyl, C═N). **^{1}H NMR** (400 MHz, $(CD_3)_2SO$): δ = 0.85 (t, 3H, ^3J = 7.40 Hz, C**H$_3$**CH$_2$CH$_2$), 1.44 (qn, 2H, ^3J = 7.27 Hz, CH$_3$C**H$_2$**CH$_2$), 2.39 (s, 3H, 4'-CH$_3$), 2.46 (t, 2H, ^3J = 7.10 Hz, CH$_3$CH$_2$C**H$_2$**), 3.77 (s, 2H, 4-CH$_2$),7.24 (d, 1H, ^3J = 4.96 Hz, H-5'), 7.37 (d, 1H, ^3J = 4.00 Hz, H-5), 8.23 (s, 1H, H-3'), 8.36 (s, 1H, H-3), 8.51 (d, 1H, ^3J = 4.96 Hz, H-6'), 8.56 (d, 1H, ^3J = 4.95 Hz, H-6). **^{13}C{^{1}H} NMR** (100.60 MHz, $(CD_3)_2SO$): δ = 11.7 (**C**H$_3$CH$_2$CH2), 21.0 (4'-CH$_3$), 22.6 (CH$_3$**C**H$_2$CH$_2$), 50.7 (CH$_3$CH$_2$**C**H$_2$), 51.9 (4-CH$_2$), 119.6 (C-3), 121.2 (C-3'), 123.1 (C-5), 124.7 (C-5'), 148.7 (C-4), 148.8 (C-6', C-6), 151.3(C-4'), 155.2 (C-2, C-2'). **Elemental analysis** (%): Calculated for $C_{15}H_{19}N_3$ (241.3380): C, 74.65; H, 7.94; N, 17.41; Found: C, 74.10; H, 7.76; N, 17.05. **MS** (EI; *m/z*): Calculated for $C_{15}H_{19}N_3$ [M – $CH_3CH_2CH_2NH$]$^+$,184.10. Found: 184.00.

2.6.4.3. Preparation of L2

A synthetic procedure, analogous to that of compound **L1**, was followed in the synthesis of the dendritic ligands **L2** and **L3**. Synthesis of ligand **L2** involved reacting 4'-methyl-2,2'-bipyridyl-4-carboxaldehyde (0.400 g; 2.02 mmol) and DAB-G1dendr-$(NH_2)_4$ (0.160 g, 0.505 mmol) in dry CH_2Cl_2 (30.0 mL) and $MgSO_4$ (0.100 g). The workup was carried out as outlined in the preparation of **L1** with $NaBH_4$ (0.115 g, 3.03 mmol) used as the reducing agent.

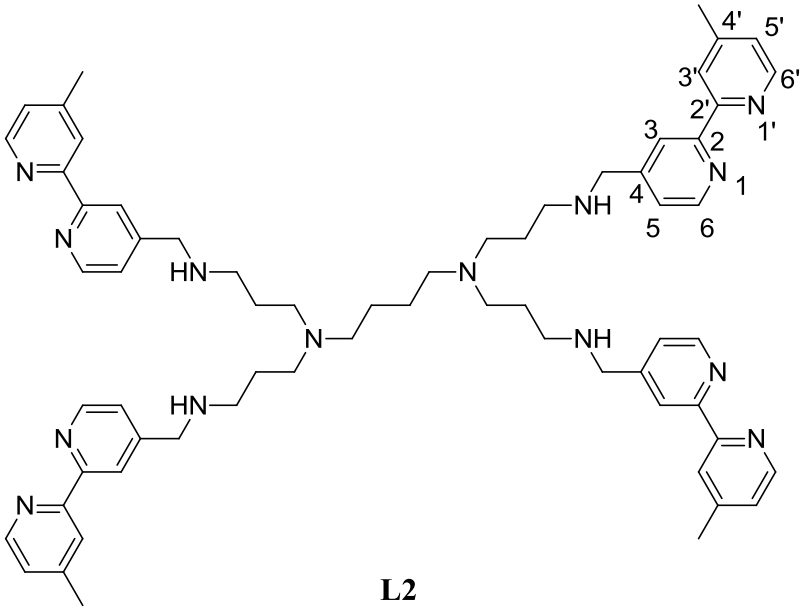

L2

Compound **L2**: Yellow oil, Yield: 0.290 g (54.9%). **IR**: Nujol between NaCl plates, ν/cm^{-1}= 1596, 1554 (sharp, bipyridine, C═N). **^{1}H NMR** (400 MHz, $(CD_3)_2SO$): δ = 1.23 (br signal, 4H, $NCH_2C\mathbf{H_2}C\mathbf{H_2}CH_2N$), 1.47 (m, 8H, $NCH_2C\mathbf{H_2}CH_2NH$), 2.20 – 2.34 (overlapping peak signals, 24H, 4'-CH_3, $NC\mathbf{H_2}CH_2CH_2C\mathbf{H_2}N$, $NC\mathbf{H_2}CH_2CH_2NH$), 2.45 (m, 8H, $NCH_2CH_2C\mathbf{H_2}NH$), 3.68 (s, 8H, 4-CH_2), 7.19 (d, 4H, ^3J = 4.35 Hz, H-5'), 7.28 (d, 4H, ^3J = 4.80 Hz, H-5), 8.18 (s, 4H, H-3'), 8.30 (s, 4H, H-3), 8.46 (d, 4H, ^3J = 4.88 Hz, H-6'), 8.50 (d, 4H, ^3J = 4.88 Hz, H-6). **^{13}C{^{1}H} NMR** (100.60 MHz, $(CD_3)_2SO$): δ = 20.6 (4'-CH_3), 24.4 ($NCH_2\mathbf{C}H_2\mathbf{C}H_2CH_2N$), 27.0 ($NCH_2\mathbf{C}H_2CH_2NH$), 47.3 ($NCH_2CH_2\mathbf{C}H_2NH$), 51.7 ($N\mathbf{C}H_2CH_2CH_2NH$), 52.1 (4-$CH_2$), 53.4 ($N\mathbf{C}H_2CH_2CH_2\mathbf{C}H_2N$), 119.6 (C-3), 121.1 (C-3'), 123.0 (C-5), 124.6 (C-5'), 147.6 (C-4), 148.7 (C-6', C-6), 151.2 (C-4'), 155.1 (C-2), 155.2 (C-2'). **Elemental analysis** (%): Calculated for $C_{64}H_{80}N_{14}.CH_2Cl_2$ (1130.3690): C, 69.07; H, 7.31; N, 17.35; Found: C, 69.18; H, 7.36; N, 17.35. **MS** (HR – ESI – TOF, *m/z*): Calculated for $C_{64}H_{80}N_{14}$ $[M + H]^+$, 1045.6769. Found: 1045.6774.

2.6.4.4. Preparation of L3

L3 was prepared by reacting 4'-methyl-2,2'-bipyridyl-4-carboxaldehyde (0.411 g; 2.07 mmol) and DAB-G2dendr-$(NH_2)_8$ (0.195 g, 0.252 mmol) in dry CH_2Cl_2 (30.0 mL).

Approximately 0.100 g of anhydrous $MgSO_4$ was added. $NaBH_4$ (0.153 g, 4.03 mmol) in MeOH (50.0 mL) was used in the reducing step.

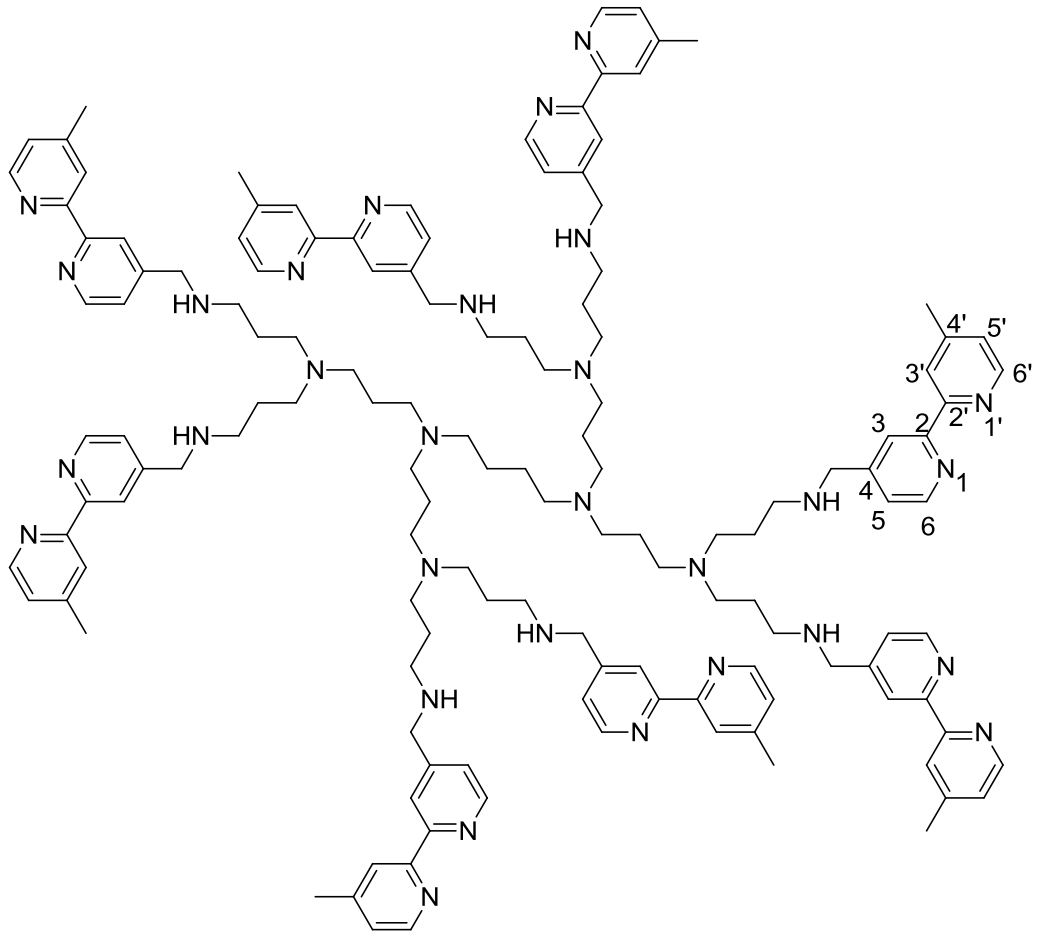

L3

Compound **L3.** Light red-yellow oil. Yield: 0.401 g (71.4%) **IR**: Nujol between NaCl plates, ν/cm^{-1}= 1598, 1560 (sharp, bipyridyl, C═N). **^{1}H NMR** (400 MHz, $(CD_3)_2SO$): δ = 1.20 (m, 4H, $NCH_2C\mathbf{H_2}C\mathbf{H_2}CH_2N$), 1.31 (br qn, 8H, $NCH_2C\mathbf{H_2}CH_2N$), 1.45 (qn, 16H, ^3J = 6.72 Hz, NCH2C**H2**CH2NH), 2.16 – 2.22 (two overlapping br t, 20H, $NC\mathbf{H_2}CH_2CH_2C\mathbf{H_2}N$, $NC\mathbf{H_2}CH_2C\mathbf{H_2}N$), 2.32 (s, 24H, 4'-$CH_3$), 2.43 – 2.47 (m, 32H, $NC\mathbf{H_2}CH_2CH_2NH$, $NCH_2CH_2C\mathbf{H_2}NH$), 3.67 (s, 16H, 4-CH_2), 7.15 (d, 8H, ^3J= 4.92 Hz, H-5'), 7.24 (dd, 8H, ^3J= 4.96 Hz, ^3J = 1.48 Hz, H-5), 8.14 (s, 8H, H-3'), 8.27 (s, 8H, H-3), 8.42 (d, 8H, ^3J= 4.92 Hz, H-6'), 8.46 (d, 8H, ^3J= 4.88 Hz, H-6). **^{13}C{^{1}H} NMR** (100.60 MHz, $(CD_3)_2SO$): δ = 20.4 (4'-CH_3), 24.2, 24.3 (overlapping $NCH_2C\mathbf{H_2}CH_2N$, $NCH_2C\mathbf{H_2}C\mathbf{H_2}CH_2N$), 26.9

($NCH_2\mathbf{CH_2}CH_2NH$),47.1 ($N\mathbf{CH_2}CH_2CH_2NH$), 51.7 – 51.5 (overlapping $N\mathbf{CH_2}CH_2CH_2\mathbf{CH_2}N$, $NCH_2CH_2\mathbf{CH_2}NH$), 51.9 (4-CH_2), 53.3 ($N\mathbf{CH_2}CH_2\mathbf{CH_2}N$), 119.5 (C-3), 120.9 (C-3'), 122.8 (C-5), 124.4 (C-5'), 147.3 (C-4), 148.5, 148.6 (overlapping C-6', C-6), 150.7 (C-4'), 155.1, 155.2 (overlapping C-2, C-2'). **Elemental analysis** (%): Calculated for $C_{136}H_{176}N_{30}$**.**10MeOH (2551.5340): C, 68.73; H, 8.53; N, 16.47; Found: C, 68.35; H, 8.55; N, 16.56. **MS** (HR – ESI – TOF, *m/z*): Calculated for $C_{136}H_{176}N_{30}$ $[M + 2H + Na]^{3+}$, 752.0393. Found: 752.0718.

2.6.5. Synthesis and characterization of *N,N'*-pyridyl ligands

2.6.5.1. Preparation of *N*-((pyridine-2-yl)methyl)propan-1-amine (L4)[24,25]

N-propylamine (0.154 mL, 1.87 mmol) was injected dropwise to a stirring solution of 2-pyridinecarboxaldehyde (0.178 mL, 1.87 mmol) in dry CH_2Cl_2 (30.0 mL). Thereafter, $MgSO_4$ (0.100 g) was added to the stirred mixture and the reaction proceeded for 24 hours. Filtration of the drying agent and evaporation of the solvent of the filtrate afforded a brown liquid. The crude liquid was further reacted with $NaBH_4$ (0.142 g, 3.74 mmol) in MeOH (30.0 mL) under nitrogen for 24 hours. The excess hydride was quenched with ice cooled water (20.0 mL). Thereafter, the H_2O/MeOH mixture was reduced using a rotary evaporator and the crude product was extracted with CH_2Cl_2 (2 × 30.0 mL). Evaporation of CH_2Cl_2 from the combined organic extracts afforded a yellow liquid which was further purified using reverse phase column chromatography eluting with water (100%) then gradually increasing the gradient to 100% MeOH. The combined organic extracts were dried over anhydrous MgSO4, filtered and **L4** was achieved as a light non-viscous yellow oil.

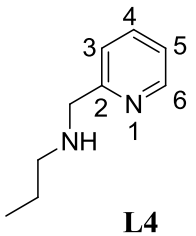

L4

Compound **L4**: light brown oil, Yield: 0.101 g (35.9%). **IR**: Nujol between NaCl plates, ν/cm^{-1}= 1592 (sharp, pyridyl, C═N), 1378 (sharp, 2° amine, CN). **^{1}H NMR** (400 MHz, $(CD_3)_2SO$): δ = 0.84 (t, 3H, ^3J = 7.38 Hz, C**H$_3$**CH_2CH_2), 1.42 (qn, 2H, ^3J = 7.18 Hz, CH_3C**H$_2$**CH_2), 2.46 (t, 2H, ^3J = 7.04 Hz, CH_3CH_2C**H$_2$**), 3.12 (br s, 1H, NH), 3.76 (s, 2H, 2-CH_2), 7.19 (m, 1H, H-4), 7.39 (m, 1H, H-3), 7.70 (td, 1H, ^3J = 7.68 Hz, ^4J = 1.83 Hz, H-5), 8.46 (m, 1H, H-6). **^{13}C{^{1}H} NMR** (100.60 MHz, $(CD_3)_2SO$): 11.7 (**C**$H_3CH_2CH_2$), 22.7 (CH_3**C**H_2CH_2), 50.8 (CH_3CH_2**C**H_2), 54.6 (2-CH_2), 121.7 (C-4, C-3), 136.3 (C-5), 148.6 (C-6), 160.5 (C-2). **Elemental analysis** (%): Calculated for $C_9H_{14}N_2$ (150.2250): C, 71.96; H, 9.39; N, 18.65; Found: C, 70.79; H, 9.14; N, 17.92. **MS** (EI; *m/z*): Calculated for $C_9H_{14}N_2$ [M – $CH_3CH_2CH_2NH]^+$,93.06. Found: 93.03.

2.6.5.2. Preparation of L5

DAB-G1dendr-$(NH_2)_4$ (0.306 mL, 0.930 mmol) was syringed dropwise to a stirring solution of 2-pyridinecarboxaldehyde (0.355 mL, 3.73 mmol) in dry CH_2Cl_2 (50.0 mL). $MgSO_4$ (0.400 g) was added and the reaction mixture was stirred overnight at room temperature. The drying agent was filtered and the solvent evaporated to afford a brown-yellow oil. The oil was dissolved in MeOH (60.0 mL) and stirred for 30 minutes while being purged with nitrogen. Subsequently, $NaBH_4$ (0.353 g, 9.33 mmol) was added to the stirred solution and the reaction proceeded overnight at room temperature under nitrogen. To quench the reaction, ice cooled water (70.0 mL) was added and the azeotropic mixture was evaporated by rotary evaporation to afford a suspension to which CH_2Cl_2 (50.0 ml) was added. The organic mixture was washed with H_2O (2 × 20.0 mL) and evaporation of CH_2Cl_2 from the combined organic

extracts afforded a brown oil which was further purified using reverse phase column chromatography as outlined in preparation of **L4**. The combined organic extracts were dried over anhydrous $MgSO_4$, filtered off and **L5** was achieved as a brown oil.

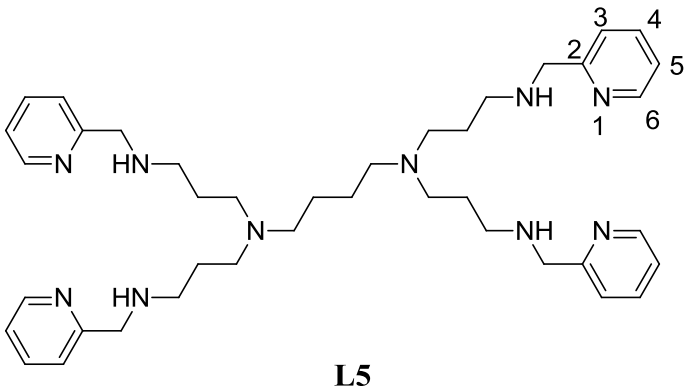

L5

Compound **L5**: Brown oil, Yield: 0.190 g (30.0%). **IR**: Nujol between NaCl plates, ν/cm^{-1}= 1593 (sharp, pyridyl, C═N), 1377 (sharp, 2° amine, C-N). **^{1}H NMR** (400 MHz, $(CD_3)_2SO$): δ = 1.30 (m, 4H $NCH_2C\mathbf{H_2}C\mathbf{H_2}CH_2N$), 1.53 (br qn, 8H, $NCH_2C\mathbf{H_2}CH_2NH$, 2.29 – 2.38 (overlapping m, 12H, $NC\mathbf{H_2}CH_2CH_2C\mathbf{H_2}N$, $NC\mathbf{H_2}CH_2CH_2NH$), 2.54 (br t, 8H, $NCH_2CH_2C\mathbf{H_2}NH$),), 2.81 (br s, 4H, NH), 3.77 (s, 8H, 2-CH_2), 7.19 (m, 4H, H-4), 7.38 (d, 4H, ^3J = 7.80 Hz, H-3), 7.69 (br td, 4H, H-5), 8.46 (br d, 4H, H-6). **^{13}C{^{1}H} NMR** (100.60 MHz, $(CD_3)_2SO$): 24.4 ($NCH_2\mathbf{C}H_2CH_2CH_2N$), 26.7 ($NCH_2\mathbf{C}H_2CH_2NH$), 47.2 ($NCH_2CH_2\mathbf{C}H_2NH$), 51.7 ($N\mathbf{C}H_2CH_2CH_2NH$), 53.4 ($N\mathbf{C}H_2CH_2CH_2\mathbf{C}H_2N$), 54.8 (2-$CH_2$), 121.6 (C-4), 122.7 (C-3), 136.2 (C-5), 148.6 (C-6), 159.9 (C-2). **Elemental analysis** (%): Calculated for $C_{40}H_{60}N_{10}.2H_2O$ (717.0200): C, 67.01; H, 9.00; N, 19.54; Found: C, 66.57; H, 8.92; N, 19.60. **MS** (HR – ESI – TOF, *m/z*): Calculated for $C_{40}H_{60}N_{10}$ $[M + 2H]^{2+}$, 341.2580. Found 341.2581.

2.6.5.3. Preparation of L6

Ligand **L6** was synthesized in analogous manner to **L5**. DAB-G2dendr-$(NH_2)_8$ (0.360 mL, 0.466 mmol) and 2-pyridinecarboxaldehyde (0.400 g, 3.73 mmol) were stirred in dry CH_2Cl_2

(40.0 mL) and $MgSO_4$ (0.100 g) was added. Thereafter, the reaction was stirred for 24 hours prior to the reducing step using $NaBH_4$ (0.656g, 17.3 mmol) in MeOH (40.0 mL).

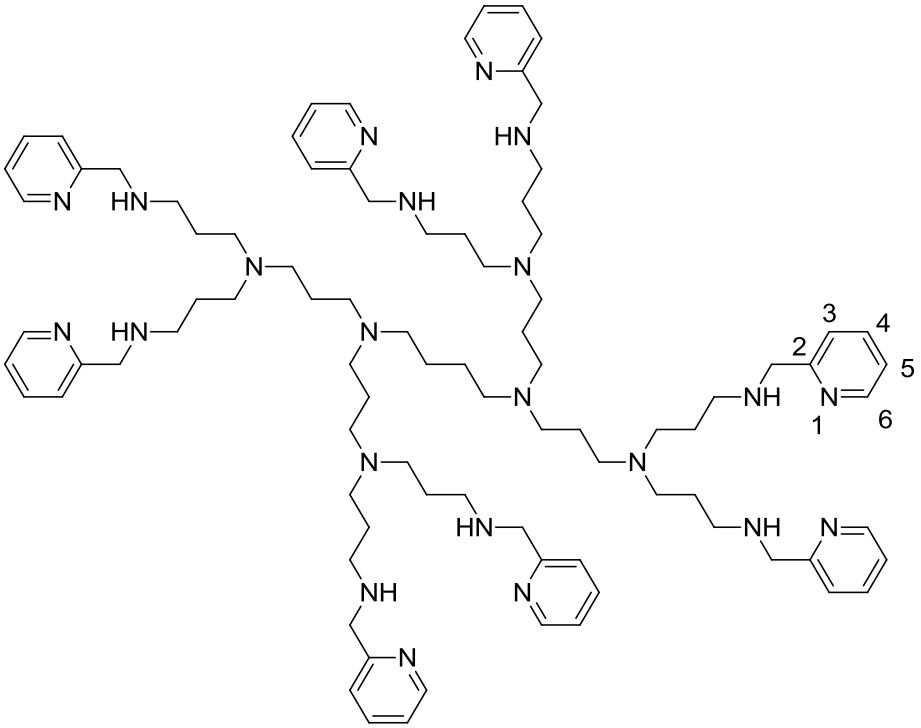

L6

Compound **L6**. Dark brown oil, Yield: 0.89 g (44.0%). **IR**: Nujol between NaCl plates, ν/cm^{-1} = 1592 (sharp, pyridyl, C═N), 1377 (sharp, 2° amine, C-N). **^{1}H NMR** (400 MHz, $(CD_3)_2SO$): δ = 1.38 (m, 4H, $NCH_2C\mathbf{H_2}C\mathbf{H_2}CH_2N$), 1.57 (br qn, 8H, $NCH_2C\mathbf{H_2}CH_2N$), 1.69 (qn, 16H, $NCH_2C\mathbf{H_2}CH_2NH$), 1.94 (br s, NH), 2.40 (m, 20H, $NC\mathbf{H_2}CH_2CH_2C\mathbf{H_2}N$, $NC\mathbf{H_2}CH_2C\mathbf{H_2}N$) 2.50 (t, 16H, ^3J = 7.20 Hz, $NC\mathbf{H_2}CH_2CH_2NH$), 2.70 (t, 16H, ^3J = 7.02 Hz, $NCH_2CH_2C\mathbf{H_2}NH$), 3.90 (s, 16H, 2-CH_2), 7.12 (m, 8H, H-4), 7.31 (d, 8H, ^3J = 7.68 Hz, H-3), 7.63 (tdd, 8H, ^3J = 7.72Hz, ^4J = 1.72 Hz, H-5, ^6J = 0,72 Hz, H-5), 8.55 (ddd, 8H, ^3J = 4.89 Hz, ^4J = 1.72 Hz, ^5J = 0.96 Hz, H-6). **^{13}C{^{1}H} NMR** (100.60 MHz, $(CD_3)_2SO$): 20.4 ($NCH_2\mathbf{C}H_2CH_2N$), 24.2 ($NCH_2\mathbf{C}H_2\mathbf{C}H_2CH_2N$), 27.5 ($NCH_2\mathbf{C}H_2CH_2NH$), 47.8 ($NCH_2CH_2\mathbf{C}H_2NH$), 51.5 ($N\mathbf{C}H_2CH_2CH_2\mathbf{C}H_2N$, $N\mathbf{C}H_2CH_2\mathbf{C}H_2N$), 51.7 ($N\mathbf{C}H_2CH_2CH_2NH$,), 51.9 (2-$CH_2$), 119.5 (C-3), 120.9 (C-3'), 121.9 (C-4), 122.8 (C-5),

124.4 (C-5') 148.6 (C-6), 160.1 (C-2). **Elemental analysis** (%): Calculated for $C_{88}H_{136}N_{22}.CH_2Cl_2$ (1587.1370): C, 67.35; H, 8.76; N, 19.42; Found: C, 66.91; H, 8.76; N, 19.18. **MS** (HR – ESI – TOF, *m/z*): Calculated for $C_{88}H_{136}N_{22}$ $[M + 4H]^{4+}$, 376.2908. Found 376.2898. $\boldsymbol{S_{25\,°C}}$ = 0.01 mg/μL in water.

2.7. References

1. C. Spagnul, R. Alberto, G. Gasser, S. Ferrari, V. Pierroz, A. Bergamo, T. Gianferrara, E. Alessio, *J. Inorg. Biochem.*, 2013, **122**, 57 – 65.
2. D. F. Baban, L. W. Seymour, *Adv. Drug Delivery Rev*., 1998, **34**, 109 – 119.
3. P. Govender, N. C. Antonels, J. Mattsson, A.K. Renfrew, P. J. Dyson, J. R. Moss, B. Therrien, G. S. Smith, *J. Organomet. Chem*., 2009, **694**, 3470 – 3476.
4. P. Govender, A. K. Renfrew, C. M. Clavel, P. J. Dyson, B. Therrien, G. S. Smith, *Dalton Trans.,* 2011, **40**, 1158 – 1167.
5. T. Kapp, A. Dullin, R. Gust, *J. Med. Chem.,* 2006, **49**, 1182 – 1190.
6. X. Zhao, A. C. J. Loo, P. P.-F. Lee, T. T. Y. Tan, C. K. Chu, *J. Inorg. Biochem.*, 2010, **104**, 105 – 110.
7. L. C. Sudding, R. Payne, P. Govender, F. Edafe, C. M. Clavel, P. J. Dyson, B. Therrien, G. S. Smith, *J. Organomet. Chem*., 2014, **774**, 79 – 85.
8. E. W. Price, C. Orvig, *Chem. Soc. Rev.*, 2014, **43**, 260 – 290.
9. B. H. Zinselmeyer, S. P. Mackay, A. G. Schatzlein, I. F. Uchegbu, *Pharm. Res.,* 2002, **19**, 960 – 967.
10. P. Govender, S. Pai, U. Schatzschneider, G. S. Smith, *Inorg. Chem.,* 2013, **52**, 5470 – 5478.
11. A. Juris, F. Barigelletti, S. Campagna, V. Balzani, P. Belser, A. von Zelewsky, *Coord. Chem. Rev*., 1988, **84**, 85 – 277.
12. M. E. Kober, J. V. Caspar, R. S. Lumpkin, T. J. Meyer, *J. Phys. Chem.*, 1986, **90**, 3722 – 3734.
13. J. V. Caspar, T. J. Meyer, *J. Phys. Chem.*, 1983, **87**, 952 – 957.
14. J. O. Massing, R. P. Planalp, *Dalton Trans*., 2015, **44**, 11887 – 11892.

15. A. E. Martell, R. M. Smith, *NIST Critically Selected Stability Constants for Metal Complexes, Version 8.0,* National Institute of Science and Technology (NIST), Gaithersburg, MD, 2004.

16. B. M. Peek, G. T. Ross, S. W. Edwards, G. I. Meyer, T. J. Meyer, B. W. Erickson, *Int. J. Peptide and Protein Res.*, 1991, **38**, 114 – 123.

17. G. F. Strouse, J. R. Schoonover, R. Duesing, S. Boyde, W. E. Jones Jr., T. J. Meyer, *Inorg. Chem*., 1995, **34**, 413 – 481.

18. N. Rabjohn, *Org. React.*, 1965, **14**, 261 – 270.

19. C. Busche, P. Comba, A. Mayboroda, H. Wadepohl, *Eur. J. Inorg. Chem.,* 2010, 1295 − 1302.

20. S. Yao, A. M. Jones, J. Du, R. K. Jackson, J. O. Massing, D. P. Kennedy, N. E. Bencivenga, R. P. Planalp, S. C. Burdette, W. R. Seitz, *Analyst,* 2012, **137**, 4734 – 4741.

21. A. F. Abde-Magid, K. G. Carson, B. D. Harrism, C. A. Maryanoff, R. D. Shah, *J. Org. Chem.*, 1996, **61**, 3849 – 3862.

22. G. J. Sutton, *Aust. J. Chem.*, 1961, **14**, 550 – 554.

23. B. Geisser, R. Alsfasser, *Dalton Trans.*, 2003, **4**, 612 – 618.

24. D. Ma, F. Lu, T. Overstreet, D. E. Milenic, M. W. Brechbiel, *Nucl. Med. Biol.*, 2002, **29**, 91 – 105.

25. P. Bandyopaddhyay, S. Jha, S. K. I. Ali, *J. Agric. Food Chem*., 2009, **57**, 9780 – 9786.

26. S. Mundinger, U. Jakkob, P. Bichovski, W. Bannwarth, *J. Org. Chem.*, 2012, **77**, 8968 – 8979.

27. S. W. Pelletier, *Alkaloids: Chemical and Biological Perspectives*, Pergamon Press, Oxford, UK, 1999, 13.

28. M. W. P. L. Baars, R. Kleppinger, M. H. J. Koch, S.-L. Yeu, E. W. Meijer, *Angew. Chem.,* 2000, **112**, 1341 – 1342.

Chapter 3

Synthesis and characterization of *fac*-[Re(CO)$_3$(*N,N'*-bidentate)X] complexes

3.1. General introduction

Rhenium occurs naturally as a mixture of non-radioactive ('cold') isotopes, ^{185}Re (37.4%) and ^{187}Re (62.6%).[1] By virtue of the 'lanthanide contraction'—a phenomenon which ensures that the complexes of two different metals are similar in terms of their physical properties (such as size and lipophilicity)—'cold' rhenium complexes are used to characterize (*e.g.* structural elucidation) radioactive ('hot') technetium-99m complexes.[1] The complexes of Re are kinetically inert and harder to reduce than their Tc analogues.[1]

Re(I) is a d^6 centre and its kinetic behaviour often permits the isolation of intermediates which are not the thermodynamic end-products.[2] The *fac*-[M(CO)$_3$]$^+$ (M = Re(I) or ^{99m}Tc(I)) core is the most versatile and studied adduct as it permits efficient complexation (or labeling) under aqueous conditions.[3-9] Traditionally, complexes of the general formula *fac*-[M(CO)$_3$Ligand] (M = Re or ^{99m}Tc, Ligand = tridentate ligand) were prepared from M_2CO_{10} through high pressure carbonylation, an impractical synthetic route for clinical application.[8]

Currently, as part of Green Chemistry, organometallic reactions in aqueous solutions are of interest in drug design. Alberto *et al.* discovered a new method for the synthesis of *fac*-[Re(CO)$_3$]$^+$ containing complexes, derived from the *fac*-(Et_4N)$_2$[Re(CO)$_3$X$_3$] (X = halide) precursor.[9] Herein, the synthesis and characterization of various *fac*-[Re(CO)$_3$(*N,N*-bidentate)X]^n (n = 0, X = Cl or Br and n= +1, X = H_2O) monomeric and dendritic complexes is described.

3.2. Neutral *fac*-[Re(CO)$_3$X] (X = Cl or Br) core complexes

A method by Del Guerzo *et al*. was used for the synthesis of chlorinated Re(I) complexes.[10] **Scheme 3.1** displays the reaction between the ligands **L1 – L6** with equimolar ratios of $Re(CO)_5Cl$ in toluene. To remove the traces of the unreacted starting material, the complexes **C7 – C12** were purified by repeated precipitation and washing with hot benzene.

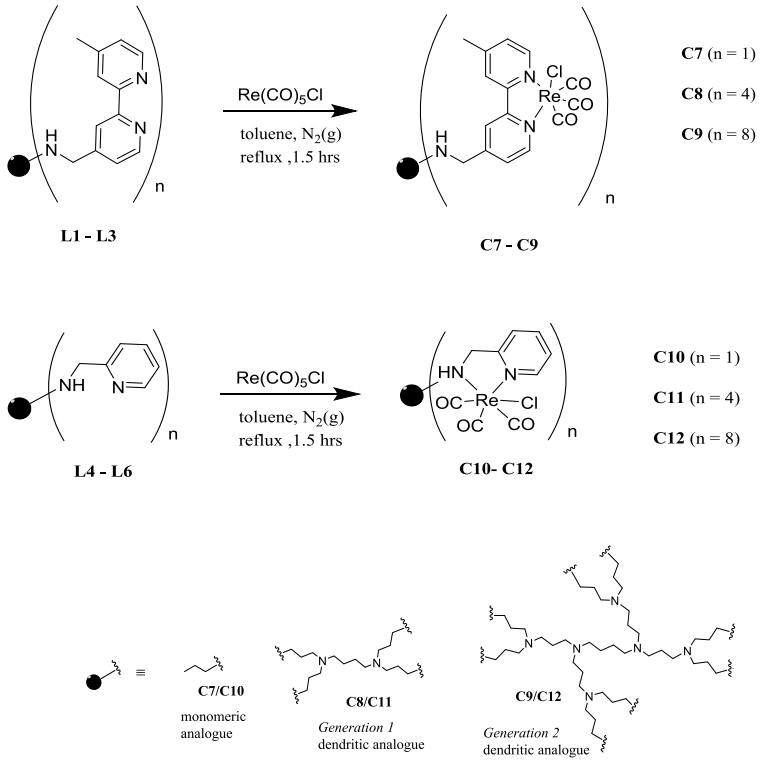

Scheme 3.1: Synthesis of the tricarbonylchlororhenium(I) complexes using $Re(CO)_5Cl$.[10]

The monomeric tricarbonylchlororhenium(I) complex **C7** was isolated as a pale yellow solid in 66.7% yield The tricarbonylchlororhenium(I) metallodendrimers, **C8** and **C9**, were isolated as yellow-brown amorphous solids in 56.6 and 33.4% yield, respectively. **C7 – C9** are soluble in $(CH_3)_2CO$, $(CH_3)_2SO$ and partially soluble in CH_3CN.

The picolyl metallodendrimers **C11** and **C12** were isolated as grey amorphous solids in 25.3 and 43.1% yield, respectively. The monomeric complex **C10** was isolated as white flakes in 49.5% yield. **C10 – C12** are soluble in $(CH_3)_2CO$, $(CH_3)_2SO$ and partially soluble CH_2Cl_2.

Furthermore, **C7 – C12** have melting point ranges greater than 300 °C. The model monomeric analogues **C7** and **C10** were found to be insoluble or rather partially soluble in most organic solvents other than $(CH_3)_2SO$, notably, at room temperature, making them difficult to crystallize. It was suggested that their corresponding brominated counterparts might be isolated as solids with the possibility to further crystallize from the appropriate solvent(s).

fac-$(Et_4N)_2[Re(CO)_3X_3]$ (X = halide) is a precursor compound that allows facile substitution of the X ligands, even under mild conditions, by mono-, bi- or tridentate incoming ligands. The brominated complexes were therefore synthesized by reacting the monomeric and dendritic ligands **L1 – L6** with the rhenium precursor *fac*-$(Et_4N)_2[ReBr_3(CO)_3]$ in dry MeOH at room temperature (**Scheme 3.2**). The desired products were collected as precipitates which were further washed with cooled MeOH to afford **C13 – C18** as defined solids.

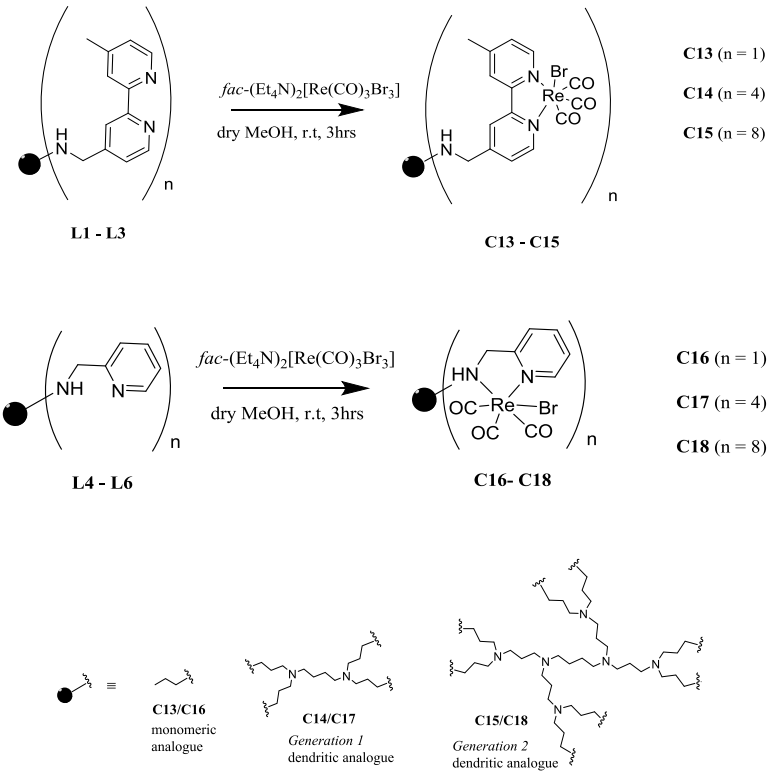

Scheme 3.2: A synthesis scheme of rhenium(I) tricarbonylbromo complexes **C13 – C18**.

The tricarbonylbromorhenium(I) metallodendrimers, **C14** and **C15**, were isolated as yellow solids in 79.0 and 61.6% yield, respectively. The monomeric analogue **C13** was isolated as a pale yellow solid in 76.0% yield. **C13** is soluble in polar organic solvents such as EtOH, $(CH_3)_2CO$, $CHCl_3$, CH_2Cl_2 and partially soluble in H_2O. The complexes **C14** and **C15** are soluble in $(CH_3)_2SO$ and partially soluble in CH_2Cl_2. **C13 – C15** have melting point range less than 200 °C.

The picolyl monomeric complex **C16** was isolated in 57.0% yield as a white solid which was further recrystallized from EtOH to afford white needles. **C16** is soluble in polar organic solvents such as EtOH, $(CH_3)_2CO$, $(CH_3)_2SO$, $CHCl_3$, CH_2Cl_2, and warm MeOH. The metallodendrimers **C17** and **C18** were isolated as brown solids in 19.5% and 25.0% yield, respectively. **C17** is soluble in $(CH_3)_2CO$, $(CH_3)_2SO$ and partially soluble in warm CH_2Cl_2, whereas, **C18** is soluble in $(CH_3)_2SO$.

The structural integrity of all the complexes was confirmed using ^1H, $^{13}C\{^1H\}$ NMR, infrared spectroscopy, mass spectrometry, elemental analysis and by X-ray diffraction with respect to **C16**. The tricarbonylchlororhenium(I) and tricarbonylbromorhenium(I) complexes have similar spectroscopic features.

3.2.1. ^1H and $^{13}C\{^1H\}$ NMR spectroscopy

The NMR spectra were recorded in deuterated dimethyl sulfoxide and the spectroscopic features of the Cl complexes translate to Br complexes.

*3.2.1.1. fac-[$Re_n(CO)_{3n}$(N,N'-bipyridyl)X_n] (n = 1, 4 and 8. X = Cl or Br) complexes (**C7** – **C9** and **C13 – C15**)*

The ^1H NMR spectrum in **Figure 3.1** corresponds to the mononuclear complex **C7** and displays a distinctive downfield shift between 9.00 – 7.57 ppm corresponding to the

bipyridyl ring aromatic protons as a result of tricarbonylbromorhenium(I) coordination preference for the bipyridyl *N,N'*-donor atoms, attesting to the complexation reaction.

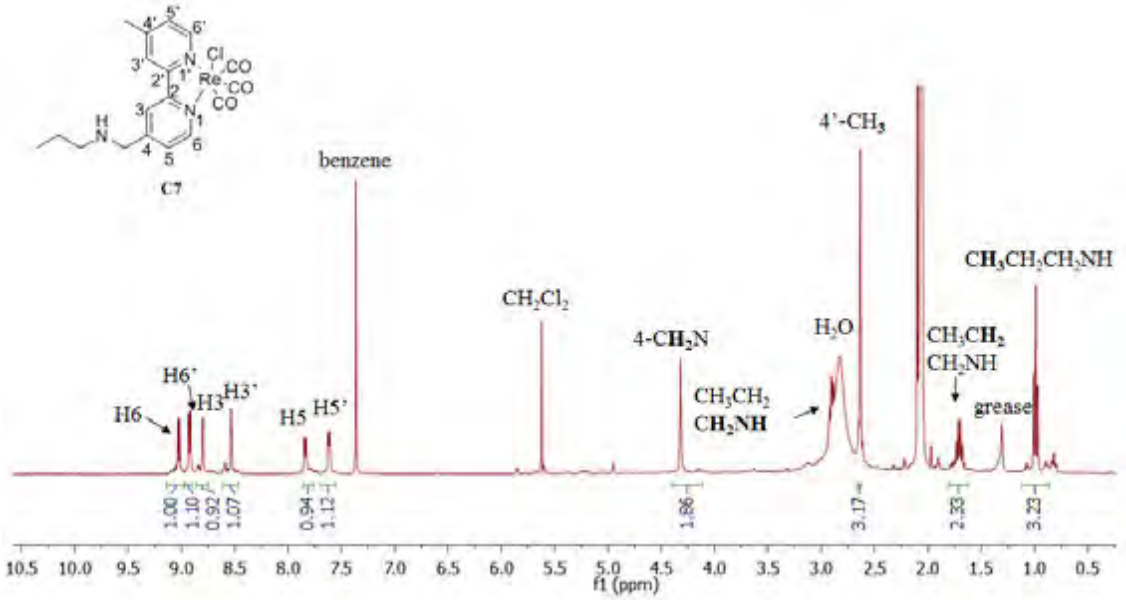

Figure 3.1: ^{1}H NMR spectra of the monomeric complex **C7** in $(CD_3)_2CO$.

Furthermore, in the ^{1}H NMR spectrum of **C7** the C**H**$_3$CH$_2$CH$_2$NH aliphatic protons corresponding to the terminal *N*-propyl chain appear slightly downfield and overlap with the deuterated solvent water signal between 2.75 – 3.00 ppm, the presence of the C**H**$_3$CH$_2$CH$_2$NH aliphatic protons in the spectrum was also confirmed by 2D NMR spectra. The deshielding shifts of the aromatic and aliphatic proton resonances in the ^{1}H NMR spectrum of **C7** were encountered in the ^{1}H NMR spectrum of the tricarbonylbromorhenium(I) mononuclear analogue **C13**. The similarities in the chemical shifts of **C7** and **C13** confirm the complexation reaction. The tricarbonylchlororhenium(I) metallodendrimers **C8** and **C9** have spectral changes analogous to their corresponding tricarbonylbromorhenium(I) counterparts, **C14** and **C15**.

Figure 3.2 illustrates the ^{1}H NMR spectrum of the first generation tricarbonylbromorhenium(I) complex **C14** in deuterated dimethylsulfoxide.

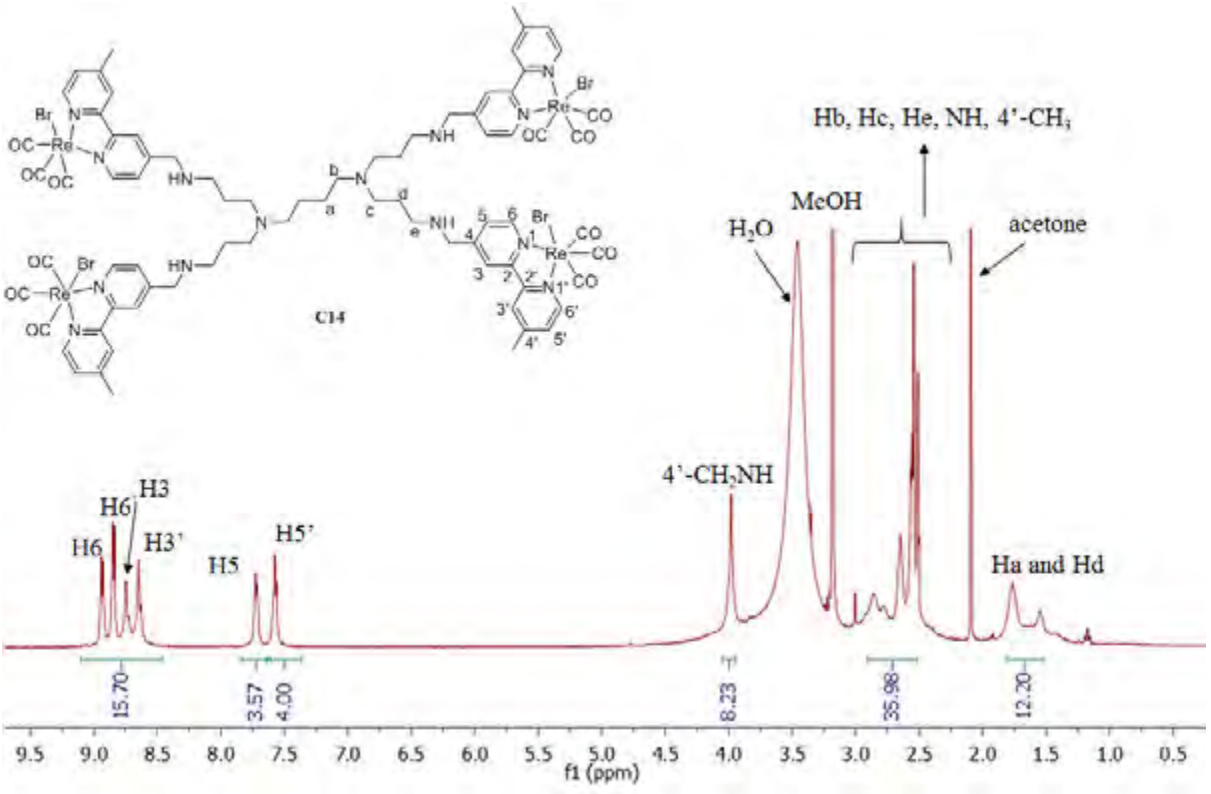

Figure 3.2: ^{1}H NMR spectrum of **C14** in $(CD_3)_2SO$.

In the ^{1}H NMR spectrum of the multinuclear complex **C14**, the broadening characteristic of the proton resonances corresponding to the dendritic arms and core (DAB), in the aliphatic region between 1.50 – 3.00 ppm, is observed as a result of the paramagnetic rhenium(I) metal. In general, the presence of an unpaired electron in the paramagnetic metal broadens the NMR lines of the nuclei of a compound with which it form a complex.[11-13] The magnetic field of the paramagnetic ion changes the relaxation time of the magnetically active nuclei.[11-13] Thus, line broadening is a consequence of the enhanced relaxation time which affords the observation of instantaneous NMR signals from all possible orientations (adverse broad peaks) of the molecule in solution (isotropic effect), instead of the averaged signals normally observed for protracted relaxation events (defined peaks).[11-13] The complexation reaction is confirmed by the downfield chemical shifts of the bipyridyl ring aromatic protons, which were previously observed between 7.19 – 8.50 ppm in the ^{1}H NMR spectrum of **L2** (**Chapter 2**, **Figure 2.4**), now resonating between 7.50 – 9.00 ppm in the ^{1}H NMR spectrum

of **C14**. In addition to the line broadening of the aliphatic proton signals, peak broadening is also observed in the aromatic region of **C14** ^{1}H NMR spectrum (supported by presence of broad doublets and multiplets). The line broadening is observed in the ^{1}H NMR spectra of all the bipyridyl metallodendrimers.

The $^{13}C\{^{1}H\}$ NMR confirms the presence of the *fac*-$[Re(CO)_3]^+$ core carbonyl carbon atoms. As a result of the low solubility of **C7** in deuterated dimethylsulfoxide, $(CD_3)_2CO$ was used to obtain the acquisition of an acceptable $^{13}C\{^{1}H\}$ NMR spectrum. The $^{13}C\{^{1}H\}$ NMR spectra of complexes **C7** – **C15** show two resonances—as opposed to the three expected resonances of the *fac*-$[Re(CO)_3]^+$ core—corresponding to the **C**O ligands between 189.0 – 198.0 ppm (for **C8/C14**) and 190.0 – 197.0 ppm (for **C13/C15**). In **Figure 3.3**, is the ^{13}C APT spectrum of **C9** in $(CD_3)_2SO$.

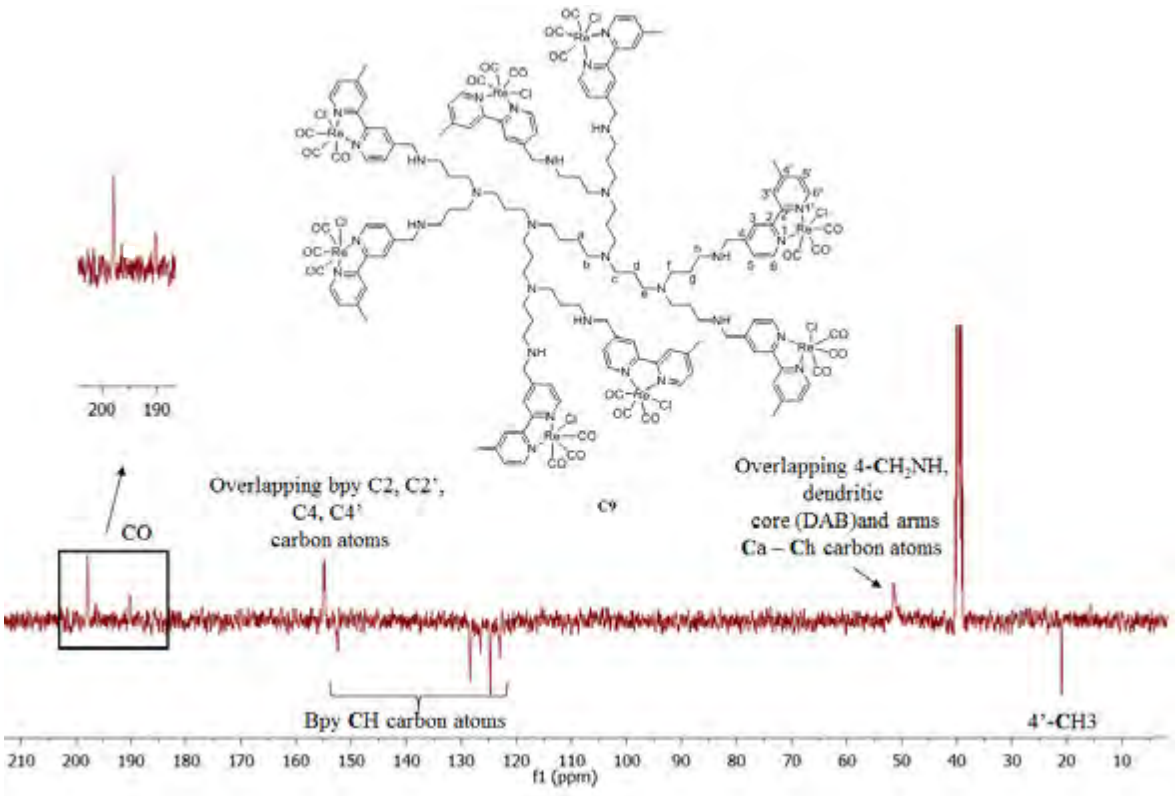

Figure 3.3: ^{13}C APT spectrum of **C9**. **C**H_3 and **C**H signals in the negative mode. **C**H_2, **C** and **C**O signals in the positive mode. Bpy = bipyridyl

In the ^{13}C APT spectrum of **C9**, the characteristic 2:1 ratio of the CO carbon atom resonances between 190 – 200 ppm signifies that two of the three carbon atoms are magnetically equivalent on NMR time scale.[14] The aliphatic carbon resonances corresponding to the dendritic core and arms coalesce into a broad resonance around ~ 50 ppm. Similarly, the overlap of the bipyridyl (C2/C2' and C4/C4') resonances between 155 – 160 ppm is observed. The presence of overlapping carbon resonances was confirmed by 2D HSQC ^{13}C – ^{1}H correlation spectrum.

*3.2.1.2. fac-[Re$_n$(CO)$_{3n}$(N,N'-picolyl)X$_n$] (n = 1, 4and 8. X = Cl or Br) complexes, (**C10** –**C12** and **C16** – **C18**)*

The NMR data of tricarbonylbromorhenium(I) and tricarbonylchlororhenium(I) complexes were recorded in deuterated dimethylsulfoxide and acetone, respectively. The NMR spectra of complexes **C10 – C12** are comparable to those of their corresponding analogues **C16 – C18**. Metallation of **L4** (**Chapter 2**, **Figure 2.5**) with 1 equivalent of *fac*-$(Et_4N)_2[ReBr_3(CO)_3]$ is confirmed by the set of two doublet of doublets at 4.16 and 4.82 ppm (previously observed as singlet at 3.76 ppm in the ^{1}H NMR spectrum of **L4**, **Chapter 2**, **Figure 2.5**) present in the ^{1}H NMR spectrum of **C16**, **Figure 3.4**.

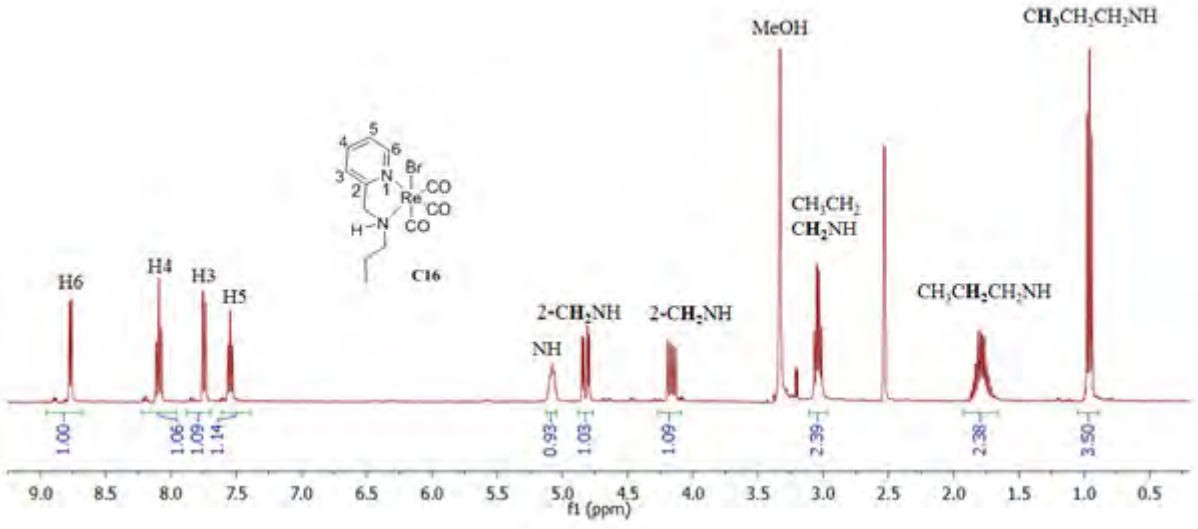

Figure 3.4: ^{1}H NMR spectrum of **C16** in $(CD_3)_2SO$.

The two doublet of doublets at 4.16 and 4.82 ppm are assigned to the 2-C**H**$_2$NH methyl proton resonances adjacent to the pyridyl ring and have ^2J coupling constants of ~15.0 Hz, consistent with geminal coupling constants.[14] The splitting of the 4-C**H**$_2$NH methyl proton resonances is also observed in the ^{1}H NMR spectra of the multinuclear complexes **C17** and **C18**, confirming synthesis of the metallodendrimers. The peak splitting patterns in the ^{1}H NMR spectra of **C17** and **C18** appear as multiplets on account of peak broadening influenced by the presence of the paramagnetic Re(I).

The complexation reaction between **L6** (**Chapter 2**) and 8 equivalents of $Re(CO)_5Cl$ is confirmed by the ^{1}H NMR spectrum of the second generation tricarbonylchloro(I) complex **C12**, in **Figure 3.5**.

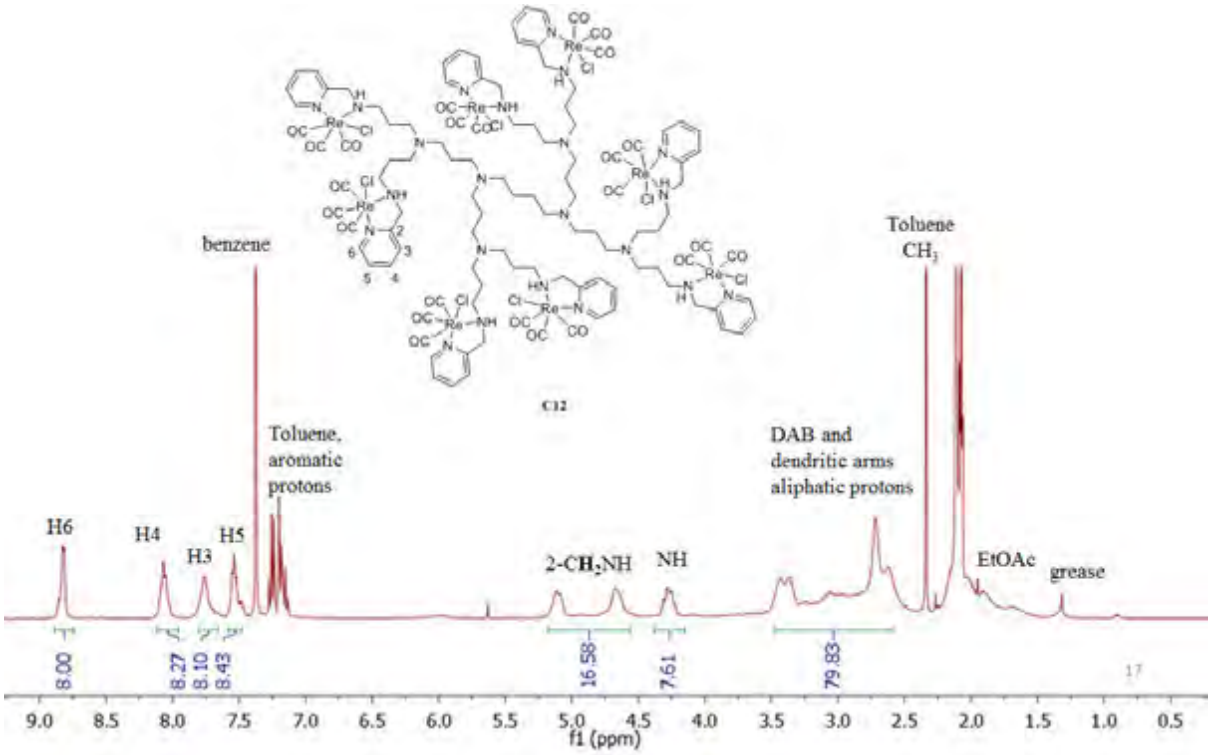

Figure 3.5: ^{1}H NMR spectrum of **C12** in $(CD_3)_2CO$.

The previously enantiotopic 2-C**H**$_2$NH methyl protons adjacent to the pyridyl ring (**L6** spectra, **Chapter 2**), appear as diastereotopic around the prochiral 2-C**H**$_2$NH centre post the complexation reaction, confirming the chiral nature of [Re(CO)$_3$(*N,N'*-picolyl)X] (X = Cl or

Br) complexes.[14] The diastereotopic nature is supported by the ^{1}H NMR spectrum of **C12** which shows two broad multiplets in the region between 4.50 – 5.25 ppm assigned to the 2-C**H$_2$**NH methyl protons adjacent to the pyridyl ring. Proton integrations in the ^{1}H NMR spectrum (**Figure 3.5**) of **C12** account for the total number of protons in the complex. Other resonances in **Figure 3.5** correspond to solvent molecules.

The most valuable NMR data were achieved from the ^{13}C{^{1}H} NMR spectra of **C10** – **C12** and **C16 – C18** supporting a bidentate chelation mode *via N,N* donor atoms. **Figure 3.6** corresponds to the 2D HSQC ^{13}C – ^{1}H correlation spectrum of **C16** in $(CD_3)_2SO$. The F1 axis corresponds to the carbon signals of **C16** and the quaternary carbons in this case are omitted. The 2D HSQC spectrum of **C16** correlates the chemical shifts of the diastereotopic 2-C**H$_2$**NH protons and *N*-propyl side chain CH_3CH_2C**H$_2$**NH protons with the carbon chemical shift at 59.7 ppm, the crosspeaks are linked by a black solid line in **Figure 3.6**.

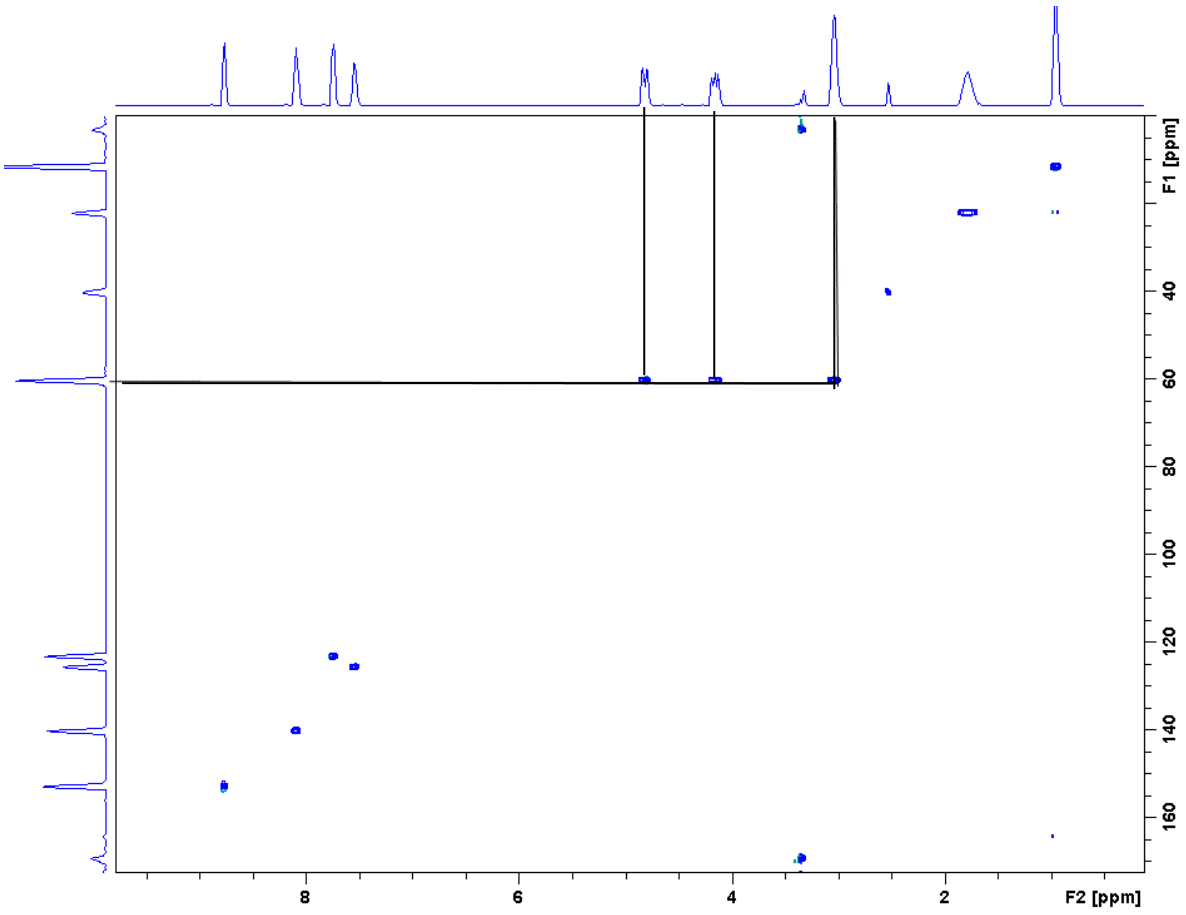

Figure 3.6: The 2D HSQC spectrum of **C16** in $(CD_3)_2SO$. The black line correlates the corresponding C-H nuclei. Peak assignments in F2 axis correspond to ***Figure 3.4***.

The presence of the three carbonyl resonances corresponding to the *fac*-$[Re(CO)_3]^+$ moiety is observed in the ^{13}C APT spectra of [$Re(CO)_3$(*N,N'*-picolyl)X] (X = Cl or Br) complexes. **Figure 3.7** shows the ^{13}C APT spectrum of **C16** in $(CD_3)_2CO$.

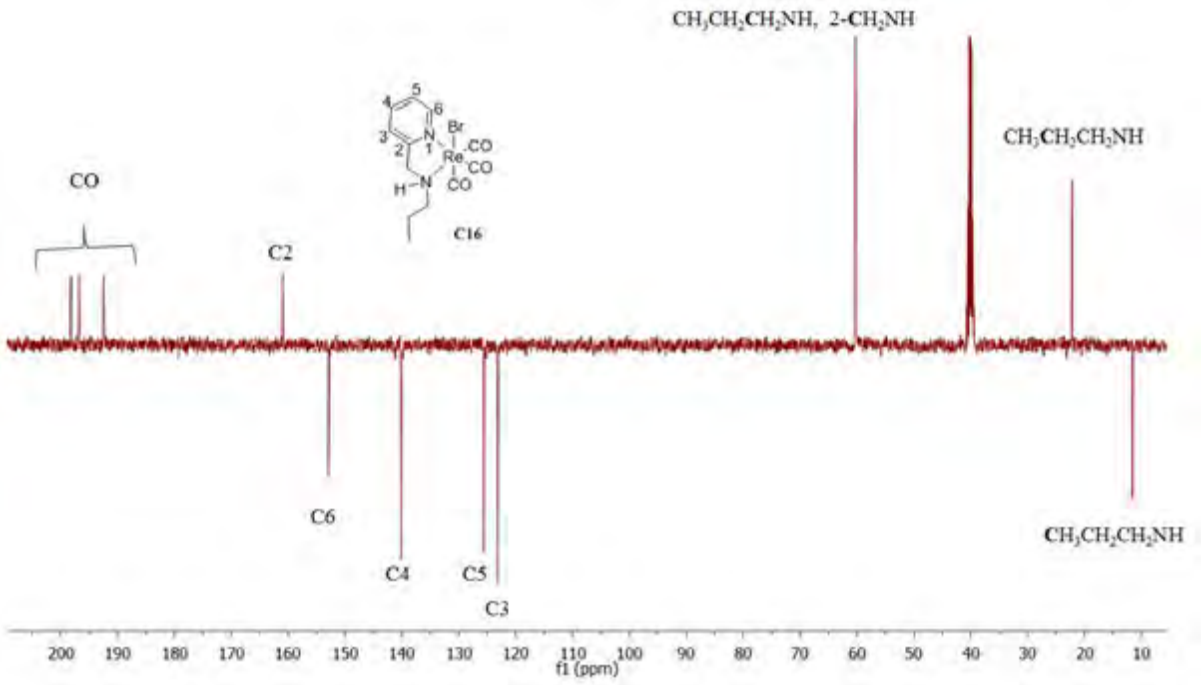

Figure 3.7: ^{13}C APT spectrum of **C16** in $(CD_3)_2SO$. **C**H_3 and **C**H signals in the negative mode. **C**H_2, **C** and **C**O signals in the positive mode.

The ^{13}C APT spectrum of **C16** in, **Figure 3.7**, reveals three deshielded CO carbon resonances upfield at 191.9, 196.2 and 197.7 ppm. The ^{13}C APT spectrum of the second generation tricarbonylchlororhenium(I) complex **C12** in deuterated acetone is shown in **Figure 3.8**. In **Figure 3.8** the three carbonyl ligands resonate at 192.5, 197.1 and 198.3 ppm, respectively. As a result of peak overlap resonances due to broad peaks, the general ^{13}C NMR spectral data of the halogenated metallodendrimers does not give the exact number of the carbon signals for the proposed structures.

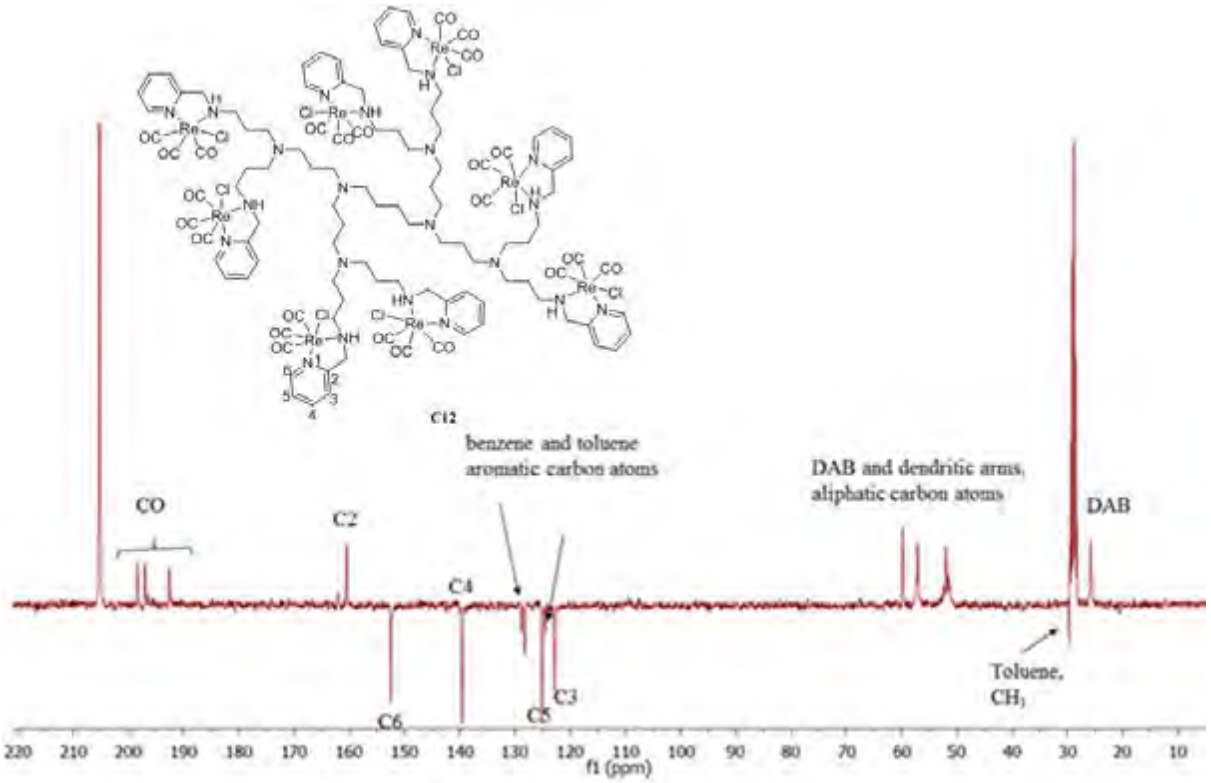

Figure 3.8: ^{13}C APT spectrum of **C12** in $(CD_3)_2CO$. **C**H_3 and **C**H signals in the negative mode. **C**H_2, **C** and **C**O signals in the positive mode.

The C4 signal resonating ~ 122.4 ppm in the $^{13}C\{^1H\}$ NMR spectra of **L4 – L6** (**Chapter 2**, *Section 2.6.5.1 – 2.6.5.3*) shifts downfield by ~20 ppm to ~140.0 ppm upon the formation of complexes **C10 – C12** and **C16 – C18**. The carbon atom C4 in picolyl systems is either electrophilic or electronegative (*e.g.* N-oxides). In the case of picolyl complexes, the presence of the *fac*-$[Re(CO)_3X]$ (X = Br or Cl) moiety imposes a deshielding effect at C4, confirming the successful complexation reactions *via N,N'*-donor atoms.

3.2.2. Infrared spectroscopy

The IR spectrum of $Re(CO)_5Cl$ in KBr pellet displays two absorption bands of different intensities corresponding to the carbonyl absorption bands at 1985 and 2046 cm^{-1}, whereas, the ATR-FTIR spectrum of *fac*-$(Et_4N)_2[ReBr_3(CO)_3]$ has typical *fac*-$[Re(CO)_3]^+$ carbonyl absorption bands at 1846 and 1995 cm^{-1}.

*3.2.2.1. fac-[Re$_n$(CO)$_{3n}$(N,N'-bipyridyl)X$_n$] (n = 1, 4 and 8. X = Cl or Br) complexes (**C7** – **C9** and **C13 – C15**)*

Table 3.1 summarises the IR and ATR-FTIR frequencies for the complexes **C7 – C9** and **C13 – C15**.

Table 3.1: Summary for the stretching frequencies of CO ligands in [Re(CO)$_3$(*N,N'*-bipyridyl)X] (X = Cl or Br) type complexes **C7 – C9** and **C13 – C15**

a = IR spectrum (KBr), **b** = ATR-FTIR spectrum

Complex	**C7**[a]	**C8**[a]	**C9**[a]	**C13**[b]	**C14**[b]	**C15**[b]
v(CO)/ cm^{-1}	2020, 1919, 1895	2019, 1917, 1893	2021, 1916, 1895	2027, 1914, 1867	2016, 1877 (br)	2010, 1960, 1879

The IR spectra of the tricarbonylchloro bipyridyl metal complexes **C7 – C9** show three CO characteristic asymmetric stretching vibrations between 2019 – 1893 cm^{-1}, indicating the presence of *fac*-[Re(CO)$_3$]$^+$ isomer.[14,15] The ATR-FTIR spectra of tricarbonylbromo-rhenium(I) complexes **C13** and **C15** have three absorption bands analogous to the bromo complexes **C7** and **C9**, as summarized in **Table 3.1**. Complex **C14** ATR-FTIR spectrum shows two absorption bands at 2016 and 1877 cm^{-1}, with the latter being broad as a result of the symmetric stretching vibrations of the CO ligands in the equatorial plane. The two bipyridyl C=N absorption bands, previously observed between 1556 – 1597 cm^{-1} in the IR spectrum of the ligands **L1 – L3**, shift to higher wavenumbers ranging between 1603 – 1628 cm^{-1} in **C7 – C15** infrared spectra, indicating that the aromatic *N,N'*-donor atoms (2,2'-bipyridyl nitrogen atoms, C=N) are the Re(I) chelate.

*3.2.2.2. fac-[Re$_n$(CO)$_{3n}$(N,N'-picolyl)X$_n$] (n = 1, 4 and 8. X = Cl or Br) complexes (**C10 – C12** and **C16 – C18**)*

Table 3.2 summarizes the IR and ATR-FTIR frequencies corresponding to the complexes **C10 – C12** and **C16 – C18**.

Table 3.2: Summary for the stretching frequencies of CO ligands in *fac*-[$Re(CO)_3$(*N,N'*-pyridyl)X] (X = Cl or Br) type complexes **C10 – C12** and **C16 – C18**

a = IR spectrum (KBr), **b** = ATR-FTIR spectrum

Complex	**C10**[a]	**C11**[a]	**C12**[a]	**C16**[b]	**C17**[b]	**C18**[b]
ν(CO)/cm^{-1}	2023, 1920, 1885	2011, 1905, 1892	2015, 1903, 1897	2012, 1912, 1875	2014, 1863 (br)	2014, 1865 (br)

The complexes **C10 – C16** exhibit three strong carbonyl absorption bands in the region ranging from 2011 – 1875 cm^{-1}. Furthermore, two carbonyl absorption bands are observed in the spectra of **C17** and **C18**, **Table 3.2**, which deviate from 1846 and 1995 cm^{-1} observed in the ATR-FTIR spectrum of the precursor *fac*-$(Et_4N)_2[ReBr_3(CO)_3]$. These data confirm the metallation of **L4 – L6** with *fac*-$[Re(CO)_3]^+$, where the carbonyl ligands are coordinated *via* a terminal CO bonding mode around on Re(I) metal center.

3.2.3. Elemental analysis and mass spectrometry

*3.2.3.1. fac-[$Re_n(CO)_{3n}$(N,N'-bipyridyl)X_n] (n = 1, 4 and 8. X = Cl or Br) complexes (**C7 – C9** and **C13 – C15**)*

The elemental analysis of the bpy tricarbonylchloro and tricarbonylbromorhenium(I) were within the acceptable limits. Notably, the elemental analysis of the complexes **C7 – C9** and **C14** attest the inclusion of water molecules. The water molecules may have resulted from the reaction solvents and the starting material DAB-PPI dendrimers which contain 1% (w/v) water. Furthermore, Jansen *et.al*. have previously reported on the capability of dendritic architectures to encapsulate small molecules by forming a dendritic box through free rotation and folding of the dendritic arms.[16]

The identification of the complexes **C7 – C9** and **C13 – C15** is supported by the HR-ESI-TOF-MS data and in each case, the base peaks corresponds to a charged complex.

*3.2.3.2. fac-[Re$_n$(CO)$_{3n}$(N,N'-picolyl)X$_n$] (X = Cl or Br) complexes (**C10** – **C12** and **C16 – C18**)*

The C, H, and N elemental analysis of the complexes **C10 – C12** and **C16 – C18** were within satisfactory ranges. The prominent mass per charge (*m/z*) spectral data obtained using HR-ESI mass spectrometry is summarised in **Table 3.3**.

Table 3.3: Summary of the mass spectral data corresponding to the *fac*-[Re(CO)$_3$(*N,N'*-picoly)X] (X = Cl or Br) complexes **C10 – C12** and **C16 – C18**

M = exact mass of the complex excluding the encapsulated solvent molecules

Complex	**C10**	**C11**	**C12**	**C16**	**C17**	**C18**
Base peak (*m/z*)	$[M + Cl]^+$	$[M + H]^+$	$[M + C_7H_8 - 8Cl]^{8+}$	$[M - Br]^+$	$[M + 2H]^{2+}$	$[M + 3H - Br]^{4+}$

The base peaks corresponding to **C11** and **C17** adducts exhibited a 1+ and 2+ charge, respectively. The base peaks of second generation metallodendrimers **C12** and **C18** depict multivalent adducts

3.2.4. Crystallographic studies on *fac*-[ReBr(CO)$_3${*N*-((pyridine-2-yl) methyl)propan-1-amine}] (C16)

The molecular structure of the monomeric model complex, *fac*-[ReBr(CO)$_3${*N*-((pyridine-2-yl)methyl)propan-1-amine}] (**C16**), was determined by X-ray diffraction, and is shown in **Figure 3.9**.

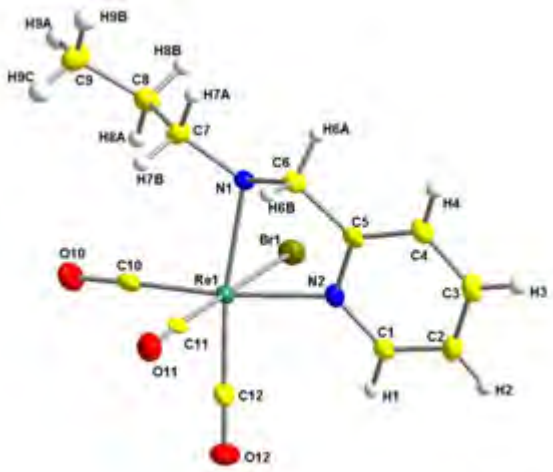

Figure 3.9: X-ray structure of *fac*-[ReBr(CO)$_3${*N*-((pyridine-2-yl)methyl)propan-1-amine}], **C16**. Ellipsoids drawn at 50% probability.

C16 crystallizes in a monoclinic space group, P2$_1$/*c*, with four formula units per unit cell (Z = 4). The asymmetric unit contains one independent molecule. The molecular structure of **C16** is represented in **Figure 3.9** along with the atom numbering scheme. The ^{1}H NMR spectrum of **C16** (**Figure 3.4**) illustrates the presence of N(1)-H bond (confirmed by proton integration and 2D NMR), whereas, the XRD structure in **Figure 3.9** shows the presence of a three bonded N(1) atom. This could be attributed to the different forms of **C16** in liquid and solid state. **Table 3.4** and **Table 3.5** illustrate the general X-ray diffraction data and geometrical parameters corresponding to **C16**, respectively.

Table 3.4: X-ray diffraction data of **C16**

empirical formula	$C_{12}H_{13}BrN_2O_3Re$
formula weight	499.35
crystal system	monoclinic
space group	$P2_1/c$
a (Å)	8.880(5)
b (Å)	21.341(5)
c (Å)	7.693(5)
α (degrees)	90.000(5)
β (degrees)	95.410(5)
γ (degrees)	90.000(5)
V (Å^3)	1451.4(13)
Z	4
D_{cald} (mg.cm^{-3})	2.285
μ (mm^{-1})	11.129
F(000)	932
T (K)	293(2)
crystal colour	colourless
θ range (degrees)	1.91 – 28.00
completeness of θ (%)	100
index ranges	h = -11 to 11
	k = -26 to 28
	l = -10 to 8
reflections collected	39 600
independent reflections	3508
R_{int}	0.0699
data/restraints/parameters	3508/0/173
GOF	1.325
R_1 [I > 2σ(I)][a]	R1 = 0.0253, wR2 = 0.082
R_1 (all data)	R1 = 0.0282, wR2 = 0.0964
ρ_{max} and ρ_{min} (e Å^{-3})	1.332, -1.660

Table 3.5: Selected average bond lengths and bond angles corresponding to **C16**

Selected bond angles	**Bond angle (°)**
C(10)-Re(1)-Br(1)	91.57(17)
C(11)-Re(1)-Br(1)	179.24(14)
C(12)-Re(1)-Br(1)	92.91(19)
N(2)-Re(1)-Br(1)	85.33(12)
N(1)-Re(1)-Br(1)	84.61(11)
C(10)-Re(1)-N(2)	174.10(19)
C(12)-Re(1)-N(1)	171.51(18)
	Bite angle
N(2)-Re(1)-N(1)	75.17(16)

Selected bond lengths	**Bond length (Å)**
Re(1)-Br(1)	2.6202(8)
Re(1)-C(10)	1.924(6)
Re(1)-C(11)	1.908(5)
Re(1)-C(12)	1.919(6)
Re(1)-N(1)	2.220(4)
Re(1)-N(2)	2.183(5)
C(5)-N(2)	1.348(7)
C(6)-N(1)	1.491(6)
N(1)-C(7)	1.502(7)

The central rhenium atom coordinates with the nitrogen atoms of *N*-((pyridine-2-yl)methyl)propan-1-amine (**L4**) to form a five-membered ring. Three carbonyl ligands are facially coordinated to the metal centre, together with a bromide anion to complete the slightly distorted octahedral arrangement around rhenium(I). The *trans* angles assigned to the rhenium–CO (C(10)-Re(1)-Br(1), C(11)-Re(1)-Br(1), C(12)-Re(1)-Br(1)) range between 171.51(18) – 179.24(14)°, showing a slight deviation from the desirable octahedral limit (180.00°).[14] The N(2)-Re(1)-N(1) chelate angle of 75.17(16)°, instead of the ideal angle of 90°, delineates the formation of a geometrically strained 5-membered ring which contributes significantly to the angular distortion of the octahedral complex, **C16**.[14,17]

The C(6)–N(1) bond length measures 1.491(6) Å which is consistent with Saw *et al*. observations of 1.46(1) Å for a single bond.[18] The bond length assigned to Re(I)-N(1), 2.220(4) Å, is slightly longer than 2.183(5) Å assigned to Re(I)-N(2). The Re-N bond angles are consistent with sp^3 and sp^2 - hybridized nitrogen donor atoms, respectively.[14,18] Also, a normal aliphatic trigonal pyramidal geometry around N(1) reflects the amino versus imino distinction of sp^3 hybridized nitrogen atom. All the bond distances and angles of **C16** are consistent with the similar structures reported in the literature.[14,17-19] The monoclinic crystal is stabilized by one C-H---O intermolecular interaction. This is formed between an aromatic hydrogen atom (H3) of the pyridine ring and the carbonyl oxygen atom of a neighbouring molecule (O11), *see* **Figure 3.10**.

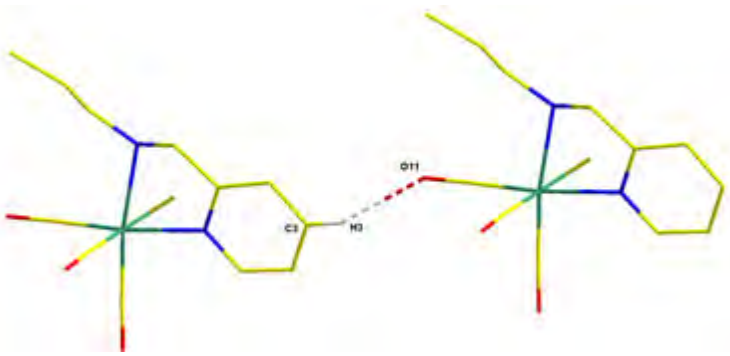

Figure 3.10: Hydrogen bonding in **C16**

The molecules pack in a head-to-head fashion diagonally across the a-b plane as illustrated in **Figure 3.11**.

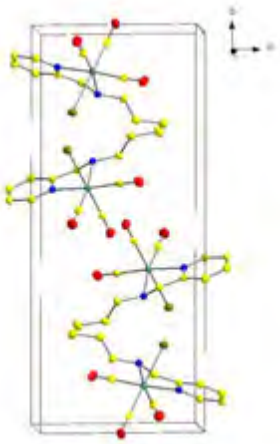

Figure 3.11: Illustration of **C16** molecules across the a-b plane

As illustrated in **Figure 3.12** the two carbon atoms which form part of the five-membered ring, C5 and C6, are displaced by 0.229(6) and 0.584(6) Å, respectively, from a plane constructed through the central rhenium atom, the two nitrogen atoms coordinated to it and the two carbonyl ligands *trans* to the nitrogen atoms.

(a)

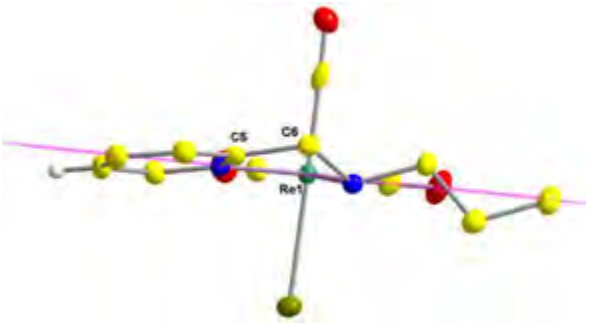

(b)

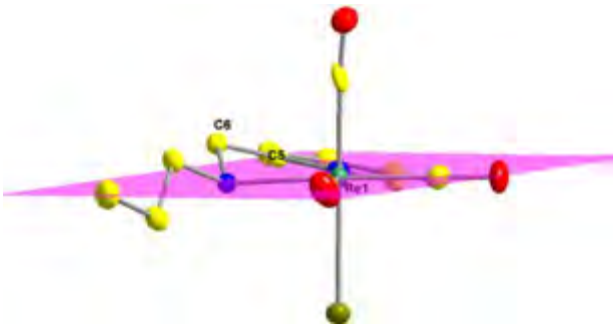

Figure 3.12: C5 and C6 lie above the mirror plane.

3.3. Synthesis and characterization of monomeric and dendritic cationic *fac*-$[Re(CO)_3H_2O]^+$ isomer complexes

In the current study, one of the aims was to synthesize water soluble dendritic Re(I) aqua complexes and to study the substitution kinetic behaviour of the complexes in aqueous medium. Different synthetic strategies have emerged from the use of tridentate ligands to a combination of a mono- and bidentate ligands (2 + 1 approach) to saturate the coordination sphere of *fac*-$[M(CO)_3(OH_2)_3]^+$ (M = Re(I) or ^{99m}Tc(I)).[20] As proposed by Mundwiler *et al.*,[21] the mixed ligand approach comprises a bidentate ligand to substitute two of the three labile aqua ligands, and a monodentate ligand to occupy the third aqua coordination site (**Scheme 3.3**).[20-22]

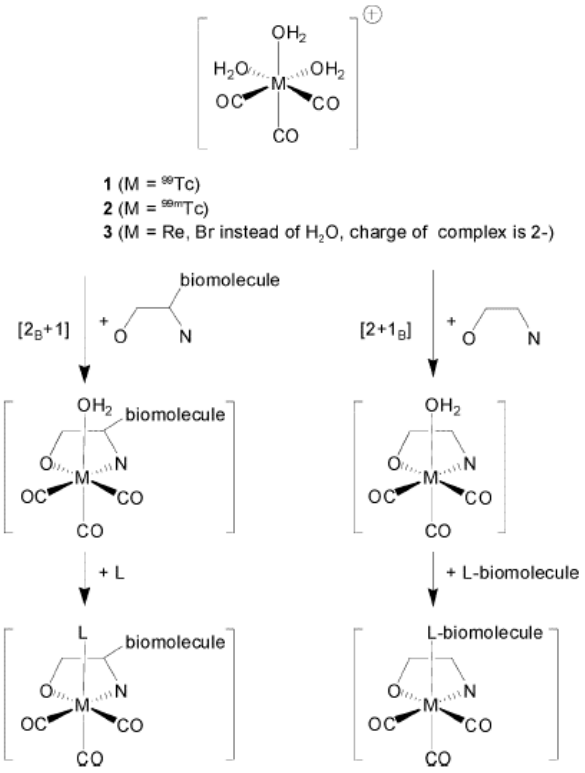

Scheme 3.3: The concept of the mixed ligand [2 + 1] approach where 2_B represents the bidentate biomolecule and 1_B represents the monodentate biomolecules.[21]

A bidentate ligand can control the lipophilicity (*e.g.* the dendrimer terminal functional groups) and a monodentate bifunctional ligand can act as a potential linker to a biomolecule.

The chemical nature of complexes achieved *via* the 2 + 1 approach (mixed ligand approach) can be tailored and the *in vivo* properties can be tuned by varying the mono- or bidentate ligands (through coordinating a mono- or bidentate biologically active molecule rather than coordinating a single tridentate targeting molecule).[20-22] The complexes **C19 – C21** and **C22 – C24** were synthesized as outlined in **Scheme 3.4**.

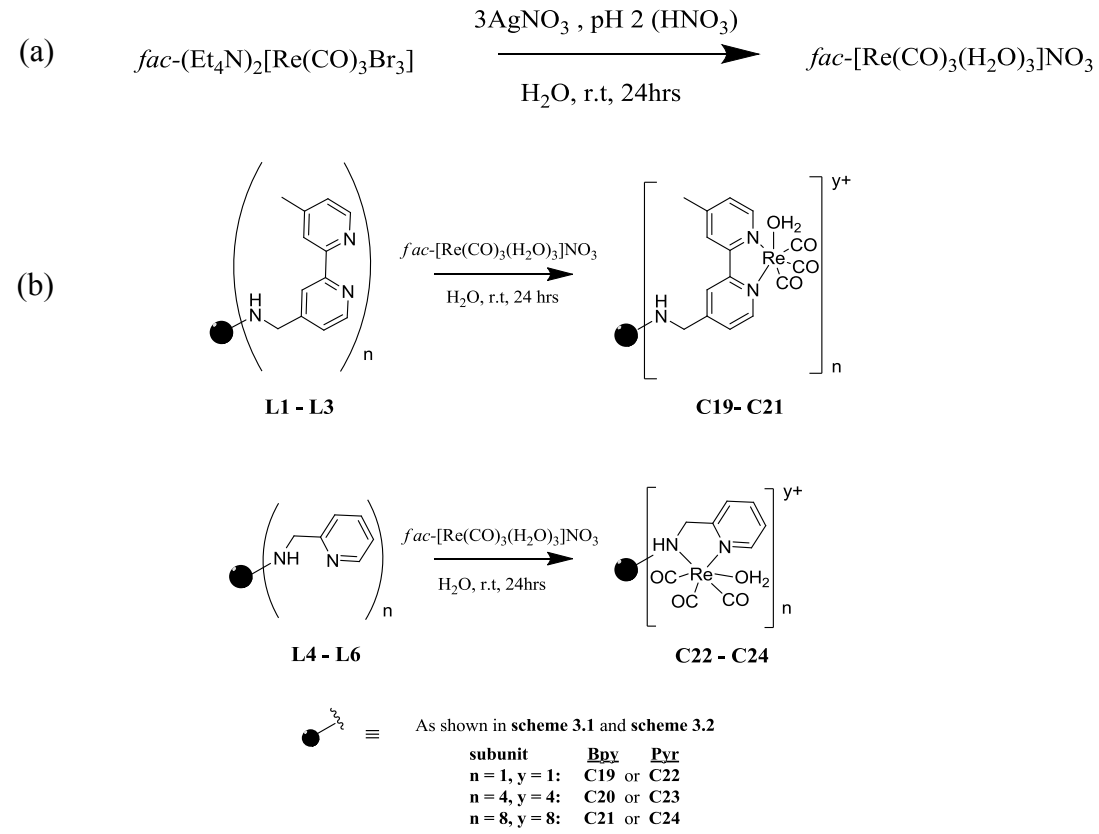

Scheme 3.4: (a) Synthesis of *fac*-$[Re(CO)_3(OH_2)_3]^+$. **(b)** Reaction scheme for the synthesis of compounds **C19 – C21** and **C22 – C24** by reacting *fac*-$[Re(CO_2)_3(OH_2)_3]^+$ with **L1 – L3**, and **L4 – L6**.

The dissolution of *fac*-$(Et_4N)_2[ReBr_3(CO)_3]$ in water, **Scheme 3.4 (a)**, results in an organometallic aqua cation *fac*-$[Re(OH_2)_3(CO)_3]^+$, which is stable in water.[23] *fac*-$(Et_4N)_2[ReBr_3(CO)_3]$ was dissolved in water under acidic conditions to minimize dimerization as a result of bridging hydroxo ligands.[24] The solution was stirred in the presence of silver nitrate, for halide extraction, to form *fac*-$[Re(CO)_3(H_2O)_3]^+$. However, the substitution reaction produces Et_4N^+ as a side product which exhibits similar polarity to *fac*-

$[Re(CO)_3Ligand]^+$ complexes,[25] making the purification of **C19 – C24** (**Scheme 3.4** (**b)**)using silica and alumina chromatography difficult. Furthermore, Et_4NBr tends to co-crystallize with the desired product(s)[25], resulting in inaccurate melting points. As a result of excess Et_4N^+, calculation of the reaction percentage yields was omitted.

The complexes **C19 – C21** were synthesized by reacting a solution of *fac*-$[Re(CO)_3(H_2O)_3]^+$ with equimolar ratios of ligands **L1 – L3**. The ligands **L1 – L3** (~30 mg) were observed to be soluble in 5 mL of water, at pH 2.2. The complexes **C19 – C21** were isolated as yellow solids which were filtered and rinsed with water. A prolonged exposure to moisture of these complexes changes their solid state to oil residues. **C19 – C21** are soluble in coordinating solvents such as MeCN and $(CH_3)_2CO$, $(CH_3)_2SO$. In solid state, the melting points range of **C19**, **C20** and **C21** were found to be 192 – 195 °C, 132 – 135 °C and 179 – 182 °C, respectively.

The complexes **C22 – C24** remained in solution after the reaction, hence, water was removed using a freeze drier. These complexes, however, are prone to decomposition and/or dimerization if placed *in vacuo* to remove water for a prolonged time limiting their characterization, as confirmed using NMR. **C22** and **C24** were isolated as colourless suspensions which turn brown when lyophilized to remove all the water, whereas, **C23** was isolated as light brown solid. **C22 – C24** are soluble in MeOH and in various non-coordinating polar organic solvents such as CH_2Cl_2 and $CHCl_3$. Spectroscopic and analytical techniques were further utilized for complete characterization of **C19 – C24**.

3.3.1. ^{1}H NMR and $^{13}C\{^1H\}$ NMR spectroscopy

Due to the protracted relaxation times of the carbonyl ligands, some of these signals are not observed on the $^{13}C\{^1H\}$ NMR time scale. However, the carbonyl ligands are detected on the IR spectra of all complexes.

3.3.1.1. *fac*-[$Re_n(CO)_{3n}$(*N,N'*-bipyridyl)$(OH_2)_n]^{n+}$ (n = 1, 4 and 8) complexes (**C19 – C21**)

The trend observed in the ^{1}H NMR spectra of the *fac*-[Re(CO)$_3$(*N,N'*-bipyridyl)X] (X – Br or Cl) type complexes is observed in the ^{1}H NMR spectra of **C19 – C21**, which are contaminated with Et_4N^+. The spectra of **C19 – C21** also shows peak broadening and contains water. In the ^{13}C{^{1}H} NMR spectra of **C20** and **C21**, the tricarbonyl carbon resonances were not observed as a result of the long relaxation time of these carbons atoms. Considering the inadequate data obtained using the NMR, other characterization methods were considered to be sufficient.

3.3.1.2. *fac*-[$Re_n(CO)_{3n}$(*N,N'*-picolyl)$(OH_2)_n]^{n+}$ (n = 1, 4 and 8) complexes (**C22 – C24**)

Similarly, the complexes **C22 – C24** exhibited similar spectroscopic features to their *fac*-[Re(CO)$_3$(*N,N'*-bipyridyl)X] (X – Br or Cl) type analogues. The monomeric analogue **C22** and the metallodendrimer **C23** could be analysed using ^{13}C{^{1}H} NMR. In **Figure 3.13** is the ^{13}C{^{1}H} NMR spectrum of **C22** in deuterated chloroform.

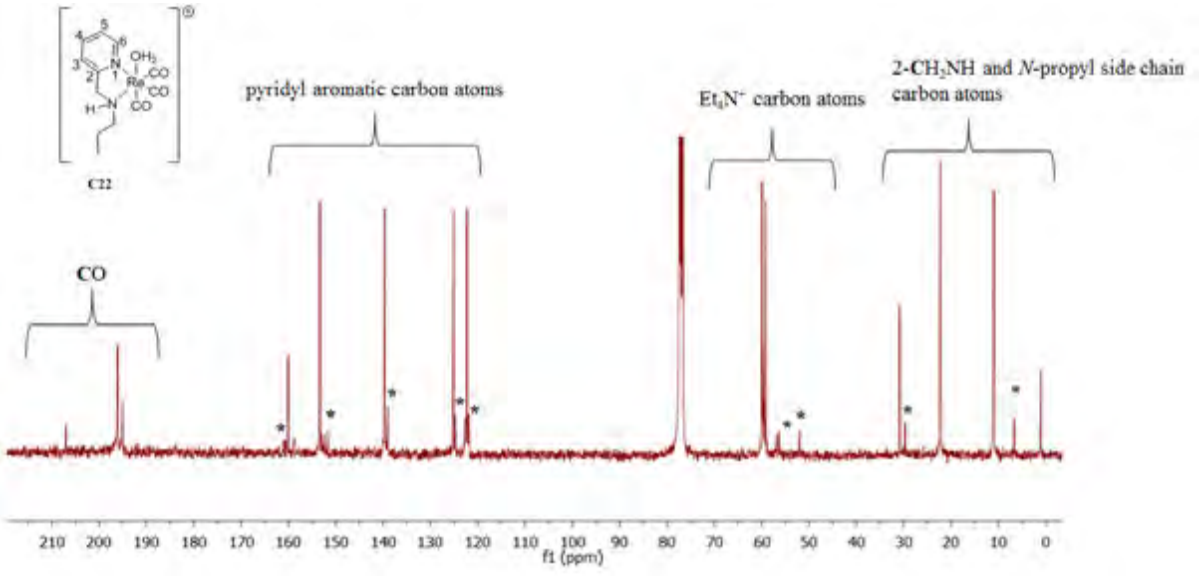

Figure 3.13: ^{13}C{^{1}H} NMR spectrum of **C22** in non-coordinating $CDCl_3$. * = unreacted **L4**.

In the spectrum of **C22**, **Figure 3.13**, the carbonyl carbon atoms are observed as three resonances with different intensities at 195.1, 196.0 and 206.9 ppm, respectively. The spectrum show traces of the unreacted starting material **L4 (**asterisks). The ^{13}C NMR spectrum of **C24,** the acquisition of an acceptable $^{13}C\{^{1}H\}$ NMR spectrum was not obtained.

3.3.2. Infrared spectroscopy

A trend was observed for the IR stretching frequencies of the metal complexes, although there are some exceptions. By virtue of the π-backbonding from interaction between π-acceptor ligand *p*-orbitals and the Re(I) *d*-orbitals, complexes with enhanced electron density have lower IR stretching frequencies (high wavenumbers).

3.3.2.1. fac-[Re$_n$(CO)$_{3n}$(N,N'-bipyridyl)(OH$_2$)$_n$]$^{n+}$ (n = 1, 4 and 8) complexes ***(C19 – C21)***

The IR absorption bands of complexes **C19 – C21** are summarized in **Table 3.6.**

Table 3.6: CO stretching frequencies of complexes **C19 – C21**

Complex	**C19**	**C20**	**C21**
ν(CO)/ cm^{-1}	2022, 1891	2025, 1894	2022, 1884

The aqua complexes **C19 – C21** exhibited two sharp IR absorption bands, of higher wavenumbers as compared to their halogenated corresponding complexes (*Section 3.2.2.1*), indicating that the interaction between the anionic counter ion NO_3^- and the aqua complexes is weak.[26]

3.3.2.2. fac-[Re$_n$(CO)$_{3n}$(N,N'-picolyl)(OH$_2$)^n]$^{n+}$ (n = 1, 4 and 8) complexes ***(C22 – C24)***

Table 3.7: CO stretching frequencies of complexes **C22 – C24**

Complex	**C22**	**C23**	**C24**
ν(CO)/ cm^{-1}	2022, 1891	2020,1881	2015, 1863

The IR spectra of complexes **C22 – C24** show two absorption bands. The positively charged complexes, where the carbonyls act mainly as sigma donors, display higher frequencies than their corresponding neutral complexes, where the carbonyls act as π-donors.[27]

The discrimination of the coordinated aqua ligand in complexes **C23** and **C24** by MeOH and DMAP ligands was investigated using IR spectroscopy. The aqua complexes **C23** and **C24** were reacted with either MeOH or DMAP as entering ligands (using MeOH as the reaction solvent) under reflux for 2 hours to afford the products that were isolated and analysed using IR spectroscopy. **Table 3.8** and **Table 3.9** summarize the IR frequencies of the substitution products.

Table 3.8: CO stretching frequencies of **C23** in MeOH and DMAP

[a] = 4:1 (Ligand:**C23** equimolar ratio), [b] = 1:1 (Ligand: **C23** equimolar ratio)

Ligand	***ν*(CO)/cm^{-1}**
MeOH[a]	2022, 2000, 1870
DMAP[b]	2021, 1901
DMAP[a]	2022, 1898

In **Table 3.8**, the IR spectra of DMAP complexes display two absorption bands with the broad band(s) approximately ~1900 cm^{-1} representing two equivalent CO ligands. There is a progressive decrease in wavenumbers from MeOH complexes to Br$^-$ complexes.

The aqua complex **C23** has two absorption bands at 2020 and 1881 cm^{-1}. The IR spectrum of the product formed between **C23** and DMAP[a] has two absorption bands at 2022 and 1898 cm^{-1}, whereas, the monosubstituted (DMAP[b]) product has two absorption bands at 2022 and 1901 cm^{-1}. There is no pronounced deviation in the wavelengths indicating that the two species, obtained from four DMAP equivalents *vs* one DMAP equivalent, are similar and that there is an increase electron density in each metal centre as the ratio of DMAP increases. The IR absorption band corresponding to DMAP[b] at 2021 cm^{-1} has a shoulder. Insignificant changes are observed in the CO asymmetric absorption band wavenumbers.

The IR spectrum of the reactions involving **C24** display the shifting of absorption bands to higher wavenumbers as summarized in **Table 3.9**.

Table 3.9: CO stretching frequencies of **C24** in MeOH and DMAP

[a] = 8:1 (Ligand:**C24** equimolar ratio), [b] = 1:1 (Ligand: **C24** equimolar ratio)

Ligand	***ν*(CO)/cm^{-1}**
MeOH[a]	2022, 1999, 1872
DMAP[b]	2018, 1999, 1886
DMAP[a]	2021, 1898

The IR spectra of the product formed between **C24** in DMAP[a] (**Table 3.9**) has similar CO wavenumbers (2021 and 1898 cm^{-1}) to the complex formed in DMAP[b] (2018, 1999 and 1886 cm^{-1}). In the presence of the aqua ligands (**Table 3.7**) the complex **C24** has two absorption bands at 2015 and 1863 cm^{-1}. By reacting **C23** with MeOH or DMAP, the IR spectrum shows the shifting of absorption bands to higher wavenumbers as summarized in **Table 3.9**. This observation was unexpected as the wavenumbers are expected to decrease with increasing ligand strength.[33] As the ligand strength is enhanced, the π-backdonation becomes stronger and the CO bond order is reduced resulting in the decrease in the CO stretching frequencies.[34]

The IR spectroscopy results illustrate that the *N,N*-picolyl chelate is a weaker σ-donor and/or π-acceptor ligand than the CO ligand. Also, the IR spectra of the complexes support the integrity of the chelate around the Re(I) metal centre as the dissociation of the ligand could not be observed as confirmed by IR absorption bands of ~1641 cm^{-1} (this absorption band is observed around ~1590 cm^{-1} in the IR spectra of the free ligands, **Chapter 2**).

3.3.3. Elemental analysis and mass spectrometry

The elemental analysis of the complexes **C19 – C24** were within the acceptable limits and the presence of excess nitric acid was detected. The mass spectrometry attests the formation of aqua adducts and *hydroxy* adducts. The *hydroxy* ligand bridges two rhenium centres from the

neighbouring dendritic arms (Re-O(H)-Re) thus displacing the aqua ligand. Therefore, a stronger acid than nitric acid is necessary to maintain acidic conditions during the storage of the complexes and inhibit dimerization. The mass spectrum of **C23** and the base peak is observed at *m/z* = 898.7490. The HR-ESI-MS spectral data is consistent with the proposed structures of the mononuclear complexes **C19** and **C22**.

3.4. Conclusions

Series of neutral monomeric and new dendritic complexes containing *fac*-[Re(CO)(*N,N*-bidentate)X] have been synthesized and characterized using analytical and spectroscopic techniques, namely ^{1}H, $^{13}C\{^{1}H\}$ NMR, infrared spectroscopy, elemental analysis and mass spectrometry. The Single X-ray diffraction of the monomeric complex **C16** elucidates the *facial* geometry of the *fac*-$[Re(CO)_3]^+$ core and the bonding mode of the *N,N'*-bidentate ligand.

Furthermore, a series of unprecedented cationic monomeric and dendritic aqua complexes have been synthesized and characterized. The mass spectrometry shows the possible formation of hydroxyl bridged metallodendrimers. The IR data of Re(I) aqua coordinated complexes agree with the general observation that anionic ligands (in neutral complexes) induce enhanced π-backbonding between the rhenium metal centre and CO ligands, resulting in a red shift of the stretching frequencies.

3.5. Experimental

3.5.1. Chemical reagents

All reagents were purchased from Sigma-Aldrich and used without further purification. The complexation reactions using $Re(CO)_5Cl$ as the precursor were performed under nitrogen. *fac*-$(Et_4N)_2[Re(CO)_3Br_3]$ was synthesized according to the literature method.[28] Methanol was distilled and dried over calcium hydride.

3.5.2. Spectroscopic and analytical methods

Nuclear magnetic resonance (NMR) spectra were recorded on a Bruker Ultrashield 400 Plus spectrometer (^{1}H: 399.95 MHz; $^{13}C\{^1H\}$: 100.60 MHz) at ambient temperature. All chemical shifts are reported in the standard δ notation of parts per million using tetramethylsilane (TMS) as an internal standard and were referenced relative to the signal of corresponding deuterated solvents. The *J* coupling constants are reported in Hertz (Hz).

Infrared (IR) absorption bands were measured on a Perkin-Elmer spectrum 100 FT-IR Nujol oil. Melting points were determined on a Reichert-Jung Thermovar hot-stage microscope and are uncorrected. Elemental analysis were performed using Thermo Flash EA 112 Series combustion analyser. Electrospray Ionisation (ESI+) mass spectra were recorded on a Waters API Quattro Micro triple quadrupole mass spectrometer by courtesy of the University of Stellenbosch. Furthermore, Electron impact mass spectrometry (EI-MS) was carried out on a JEOL GCmateII mass spectrometer.

Diffraction data was collected on a Bruker ApexII 4K CCD diffractometer using Mo-Kα (0.71073 Å) and ω-scans at 100K. All reflections were merged and integrated with SAINT-PLUS[28] and corrected for Lorentz, polarization, and absorption effects using SADABS.[29] Both structures were solved by the heavy atom method and refined through full-matrix least-

squares cycles using SHELX-97[30] as part of the WinGX[31] package with $\Sigma(||F_o|-|F_c||)^2$ being minimized. All non-H atoms were refined with anisotropic displacement parameters, while hydrogens were constrained to parent atom sites using a riding model [aromatic C–H = 0.95 Å $\{U_{iso}(H) = 1.2U_{eq}\}$; aliphatic C–H = 0.98 Å $\{U_{iso}(H) = 1.5U_{eq}\}$]. The graphics were obtained with the visual crystal structure information system software DIAMOND.[32]

3.5.3. Synthesis and characterization of *fac*-[Re(CO)$_3$(*N,N'*-bidentate)Cl] type complexes, C7 – C12

3.5.3.1. Preparation of C7

To a stirring suspension of pentacarbonylchlororhenium(I) (46.0 mg, 0.128 mmol) in toluene (12.0 ml), **L1** (34.0 mg, 0.141 mmol) was added. The suspension was heated to reflux for 1.5 hours and the reaction mixture was cooled to room temperature. The solvent was removed by suction filtration to afford a solid residue. The resulting residue was dissolved in CH_2Cl_2 (8.00 mL) and the solution was filtered by gravity. Thereafter, the solvent was removed by rotary evaporation to afford an orange solid which was rinsed with hot benzene. The resulting solid was dried under high pressure to afford complex C**7** as a yellow powder.

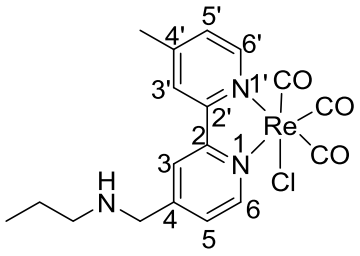

C7

Complex **C7**: Pale yellow solid, Yield: 0.018 g (66.7%). **IR**: KBr pellet, ν/cm^{-1} = 2020 (s, carbonyl, CO), 1919 (br, carbonyl, CO) 1895, (br, carbonyl, CO), 1604, 1615 (w, C=N, pyridyl). **^{1}H NMR** (400 MHz, $(CD_3)_2CO$): δ = 0.99 (t, 3 H, ^3J = 7.42 Hz, C**H$_3$**CH_2CH_2), 1.66 (sext,2H, ^3J = 7.47 Hz, CH_3C**H$_2$**CH_2), 2.59 (s, 3H, 4'-CH_3), 2.83-2.87 (overlapping t, 2H,

$CH_3CH_2C\mathbf{H_2}$), 4.31 (s, 2H,4-CH_2), 7.60 (d, 1H, ^3J= 5.52 Hz, H-5'), 7.83 (d, 1H, ^3J= 5.20 Hz, H-5), 8.53 (s, 1H, H-3'), 8.79 (s, 1H, H-3), 8.92 (d, 1H, ^3J= 5.60 Hz, H-6'), 9.01 (d, 1H, ^3J= 5.72 Hz, H-6). **^{13}C{^{1}H} NMR** (100.60 MHz, $(CD_3)_2CO$): δ = 34.8 (**C**$H_3CH_2CH_2$), 36.0 (4'-CH_3), 62.1 (CH_3**C**H_2CH_2), 67.8 (CH_3CH_2**C**H_2), 70.3 (4-CH_2), 133.3, 133.6 (C-3, C-3'), 135.6 (C-5), 126.4 (C-5'), 135.1 (overlapping peak, C-4', C-4), 150.1, 162.9 (C-6', C-6), 170.8, 172.2 (C-2, C-2'), 202.9, 208.7 (CO). **Elemental analysis** (%): Calculated for $C_{18}H_{19}ClN_3O_3Re.H_2O$ (565.04): C, 38.26; H, 3.75; N, 7.44; Found: C, 37.80; H, 3.89 N, 7.29. **MS** (HR – ESI – TOF, *m/z*): calculated for $C_{18}H_{19}ClN_3O_3Re$ $[M - Cl]^+$, 512.0984. Found: 512.0972.

Compounds **C7** – **C12** were prepared using a similar procedure by varying the metal precursor to ligand equivalences (1:1 ratio per monomeric analogue, 4:1 ratio per first generation PPI dendrimer and 8:1 ratio per second generation dendrimer).

3.5.3.2. Characterization of C8

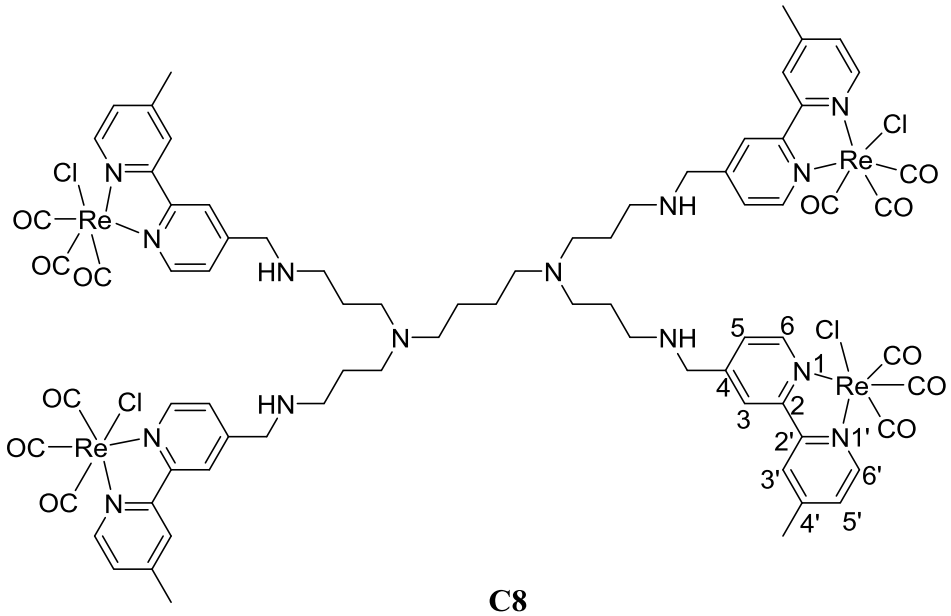

C8

Complex **C8**: Yellow-brown solid, Yield: 0.027 g (56.6%). **IR**: KBr pellet, ν/cm^{-1} = 2019 (s, carbonyl, CO), 1917 (br, carbonyl, CO), 1893 (br, carbonyl,

CO), 1607, 1621 (w, C=N, pyridyl). **^{1}H NMR** (400 MHz, $(CD_3)_2SO$): δ = 1.58 – 1.82 (broad signals $NCH_2C\mathbf{H_2}C\mathbf{H_2}CH_2N$, NH), 2.70 (overlapping signals, $NCH_2C\mathbf{H_2}CH_2NH$, $NCH_2CH_2C\mathbf{H_2}NH$, $NC\mathbf{H_2}CH_2CH_2NH$, $NC\mathbf{H_2}CH_2CH_2C\mathbf{H_2}N$), 3.51 (br s, 4'-CH3), 4.09 (m, 8H, 4-CH_2), 7.76 (d, 4H, ^{3}J = 5.08 Hz, H-5'), 7.88 (d, 4H, ^{3}J = 5.84 Hz, H-5), 8.75 – 8.82 (br s, 8H, H-3', H-3), 9.02 – 9.09 (broad dd, 8H, H-6' and H-6). **^{13}C{^{1}H} NMR** (100.60 MHz, $(CD_3)_2SO$): δ = 26.3 (4'-CH_3), 47.3, 51.8 – 52.1 ($N\mathbf{C}H_2CH_2CH_2NH$, $NCH_2CH_2\mathbf{C}H_2NH$, 4-CH_2, $N\mathbf{C}H_2CH_2CH_2\mathbf{C}H_2N$), 123.5 (C-3), 125.1 (C-3'), 125.7 (C-5), 126.9 (C-5'), 128.6, 128.8 (overlapping signals, C-4', C-4), 152.1, 152.9 (overlapping signals C-6', C-6), 155.3 (C-2'), 155.7 (C-2'), 190.7, 198.4 (CO). **Elemental analysis** (%): Calculated for $C_{76}H_{80}Cl_4N_{14}O_{12}Re_4.20H_2O$ (2628.49): C, 34.73; H, 4.60; N, 7.46; Found: C, 34.45; H, 4.80; N, 7.54. **MS** (HR – ESI – TOF, *m/z*): calculated for $C_{76}H_{80}Cl_4N_{14}O_{12}Re_4$ $[M + H_2O - 2Cl]^{2+}$, 1108.1896. Found: 1108.1668.

3.5.3.3. Characterization of C9

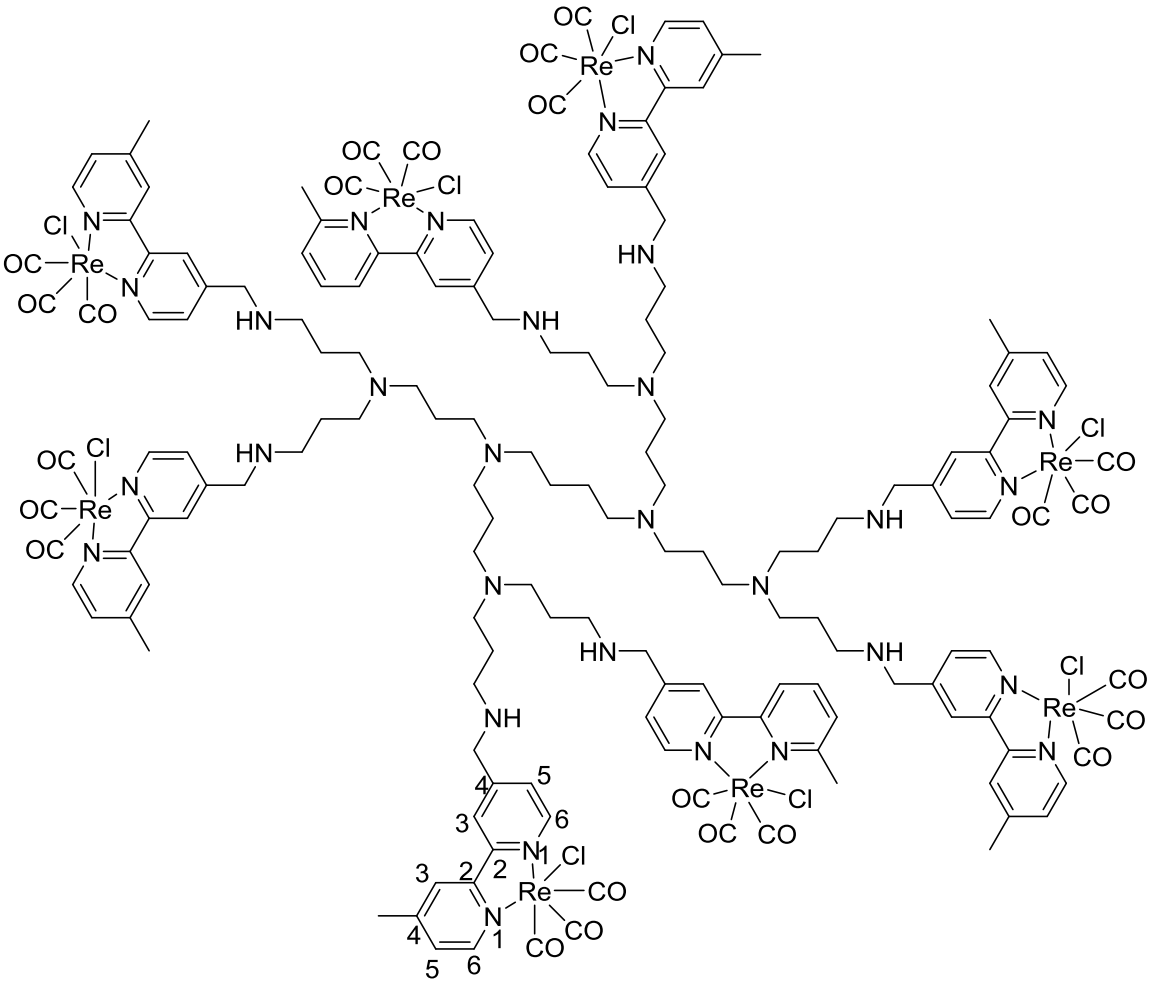

C9

Complex **C9**: Yellow brown solid, Yield: 0.0358 g (33.4%). **IR**: KBr pellet, ν/cm^{-1} = 2021 (s, carbonyl, CO), 1916 (br, carbonyl,(CO), 1895 (br, carbonyl, CO), 1609, 1628 (w, C=N, pyridyl). **^{1}H NMR** (400 MHz, $(CD_3)_2SO$): δ = 1.59 (br m, 12H, $NCH_2C\mathbf{H_2}C\mathbf{H_2}CH_2N$, $NCH_2C\mathbf{H_2}CH_2N$), 2.48 – 2.54 (m, 32H, $NCH_2C\mathbf{H_2}CH_2NH$, $NCH_2C\mathbf{H_2}CH_2N$, NH), 3.31 (br signal, 4'-CH_3, $NC\mathbf{H_2}CH_2C\mathbf{H_2}N$, $NC\mathbf{H_2}CH_2CH_2C\mathbf{H_2}N$, $NC\mathbf{H_2}CH_2C\mathbf{H_2}NH$, 4-$CH_2$), 7.51 – 7.65 (m, 16H, H-5', H-5), 8.54 – 8.50 (m, 16 H, H-3', H-3), 8.78 - 8.85 (m, 16H, H-6', H-6). **^{13}C{^{1}H} NMR** (100.60 MHz, $(CD_3)_2SO$): δ = 20.9 (4'-CH_3), 51.1 – 51.6 (br overlapping signals, $N\mathbf{C}H_2CH_2CH_2NH$, $NCH_2CH_2\mathbf{C}H_2NH$, $NCH_2CH_2\mathbf{C}H_2NH$, 4-CH_2, $N\mathbf{C}H_2CH_2CH_2\mathbf{C}H_2N$, $N\mathbf{C}H_2CH_2\mathbf{C}H_2N$), 122.8 (C-3), 124.8 (C-3'), 126.4 (C-5), 128.3 (C-5'),

152 (overlapping signals C-4, C-4'), 153.4 (overlapping signals C-6', C-6), 154.7 (C-2), 154.9 (C-2'), 190.2, 197.8 (CO). **Elemental analysis** (%): Calculated for $C_{160}H_{176}Cl_8N_{30}O_{24}Re_8.80H_2O$ (6117.81): C, 31.41; H, 5.54; N, 6.87; Found: C, 31.81; H, 5.37; N, 6.62. **MS** (HR – ESI – TOF, *m/z*): calculated for $C_{160}H_{176}Cl_8N_{30}O_{24}Re_8$ [M + $4H_2O$ – 6Cl]$^{6+}$, 756.8990. Found: 756.4956.

3.5.3.4. Characterization of C10

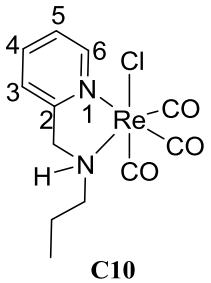

C10

Complex **C10**: White flakes, Yield: 0.065 g (49.5%). **IR**: KBr pellet, ν/cm^{-1} = 2023, 1920, 1885 (s, CO), 1604 (s, C=N, pyridyl). **^{1}H NMR** (400 MHz, $(CD_3)_2CO$): δ = 0.99 (t, 3H, ^3J = 7.42 Hz, **CH_3**CH_2CH_2), 1.88 (m, 2H, CH_3**CH_2**CH_2), 3.23 (m, 2H, CH_3CH_2C**H_2**), 4.26 (d, 1H, ^2J = 14.69 Hz, 2-CH_2), 4.99 (d, 1H, ^2J= 14.65 Hz, 2-CH_2), 7.49 (m, 1H, H-5), 7.69 (d, 1H, ^3J = 7.92 Hz, H-3), 8.04 (td, 1H, ^3J = 7.76 Hz, ^4J = 1.56 Hz, H-4), 8.76 (m, 1H, H-6). **^{13}C{^{1}H} NMR** (100.60 MHz, $(CD_3)_2CO$): 11.6 (**C**$H_3CH_2CH_2$), 23.1 (CH_3**C**H_2CH_2), 60.6 (CH_3CH_2**C**H_2), 60.8 (2-CH_2), 123.7 (C-3), 126.1 (C-5), 140.5 (C-4), 153.5 (C-6), 161.3 (C-2), 198.3, 202.5, 207.0 (CO). **Elemental analysis** (%): Calculated for $C_{12}H_{14}ClN_2O_3Re$ (455.91): C, 31.61 H, 3.10; N, 6.14; Found: C, 31.69; H, 3.06; N, 5.97. **MS** (HR – ESI – TOF, *m/z*): Calculated for $C_{12}H_{14}ClN_2O_3Re$ [M – Cl]$^+$, 421.0562. Found 421.0561.

3.5.3.5. Characterization of C11

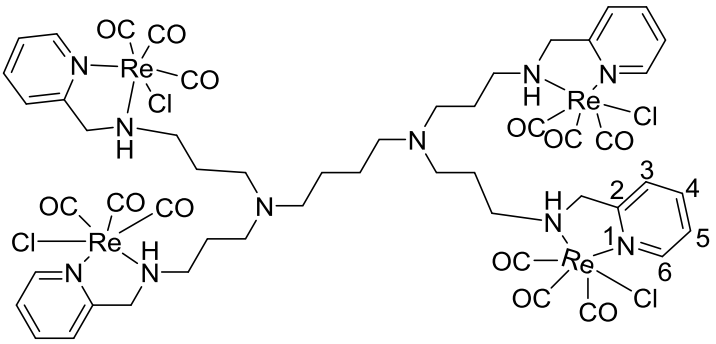

C11

Complex **C11**: Grey solid, Yield: 0.053 g (25.3%) **IR**: KBr pellet, ν/cm^{-1} = 2011 (s, CO), 1905, 1892 (br, CO), 1600 (s, C=N, pyridyl). **^{1}H NMR** (400 MHz, $(CD_3)_2CO$): δ = 1.69 (br signal, 4H, $NCH_2C\mathbf{H_2}C\mathbf{H_2}CH_2N$), 2.09, 2.84, 3.37 – 3.44 (br signals, $NCH_2C\mathbf{H_2}CH_2NH$, $NC\mathbf{H_2}CH_2CH_2NH$, $NCH_2CH_2C\mathbf{H_2}NH$), 4.48 (m, 4H, 2-CH_2), 4.68 – 4.53 (br signal, 4H, $NC\mathbf{H_2}CH_2CH_2C\mathbf{H_2}N$), 5.06 (d, 4H, ^{2}J = 11.16 Hz, 2-CH_2), 7.53 (m, 4H, H-5), 7.73 (m, 4H, H-3), 8.06 (m, 4H, H-4), 8.82 (br dd, 4H, H-6). **^{13}C{^{1}H} NMR** (100.60 MHz, $(CD_3)_2CO$): 25.0 ($NCH_2C\mathbf{H_2}C\mathbf{H_2}CH_2N$), 26.3 ($NCH_2C\mathbf{H_2}CH_2NH$), 52.5 ($N\mathbf{C}H_2CH_2CH_2NH$), 54.3 ($NCH_2CH_2C\mathbf{H_2}NH$), 57.4 ($N\mathbf{C}H_2CH_2CH_2C\mathbf{H_2}N$), 60.7 (2-$CH_2$), 123.7 (C-3), 126.1 (C-5), 140.5 (C-4), 153.4 (C-6), 161.2 (C-2), 193.3, 197.8, 199.1 (CO). **Elemental analysis** (%): Calculated for $C_{52}H_{60}Cl_4N_{10}O_{12}Re_4$ (1903.74): C, 32.81; H, 3.18; N, 7.36; Found: C, 32.44; H, 3.22; N, 6.98. **MS** (HR – ESI – TOF, *m/z*): Calculated for $C_{52}H_{60}Cl_4N_{10}O_{12}Re_4$ $[M + H]^+$, 1905.1455. Found: 1905.0795.

3.5.3.6. Characterization of C12

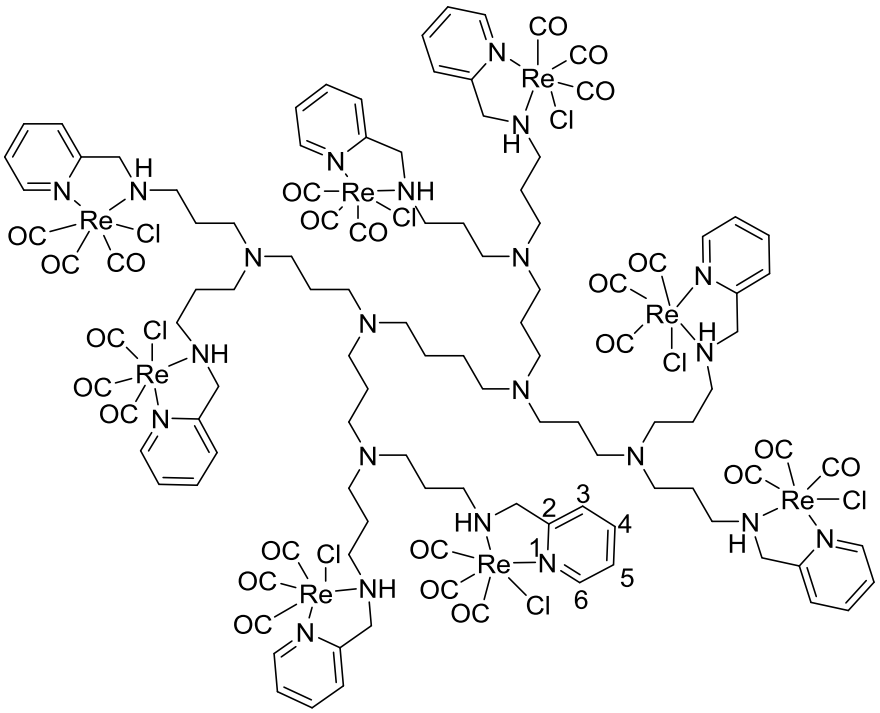

C12

Complex **C12**: Grey solid, Yield: 0.0793 g (43.1%). **IR**: KBr pellet, ν/cm^{-1} = 2015 (s, CO), 1903, 1897 (br, CO), 1607 (s, C=N, pyridyl). **^{1}H NMR** (400 MHz, $(CD_3)_2CO$): δ = 1.69 – 1.88 (br signal, 4H, $NCH_2C\mathbf{H_2}C\mathbf{H_2}CH_2N$), 2.60 – 3.45 (broad, overlapping signals, $NC\mathbf{H_2}CH_2C\mathbf{H_2}NH$, $NCH_2C\mathbf{H_2}CH_2NH$, $NC\mathbf{H_2}CH_2C\mathbf{H_2}N$, $NCH_2C\mathbf{H_2}CH_2N$), 4.22 (m, 8H, 2-CH_2), 4.65 (br s, 4H, $NC\mathbf{H_2}CH_2CH_2C\mathbf{H_2}N$), 5.08 (d, 8H, ^2J = 11.92 Hz, 2-CH_2), 7.51 (br t, 8H, H-5), 7.74 (br s, 8H, H-3), 8.05 (m, 8H, H-4), 8.80 (d, 8H, ^3J = 4.48 Hz, H-6). **^{13}C{^{1}H} NMR** (100.60 MHz, $(CD_3)_2CO$): 25.8 ($NCH_2\mathbf{C}H_2\mathbf{C}H_2CH_2N$), 51.5 – 52.3 ($N\mathbf{C}H_2CH_2\mathbf{C}H_2NH$, $NCH_2\mathbf{C}H_2CH_2NH$, $NCH_2\mathbf{C}H_2CH_2N$, $N\mathbf{C}H_2CH_2\mathbf{C}H_2N$), 57.1 ($N\mathbf{C}H_2CH_2CH_2\mathbf{C}H_2N$), 59.8 (2-$CH_2$), 122.8 (C-3), 125.3 (C-5), 139.0 (C-4), 152.5 (C-6), 160.1 (C-2), 192.5, 197.1, 198.3 (CO). **Elemental analysis** (%): Calculated for $C_{112}H_{136}Cl_8N_{22}O_{24}Re_8.4C_7H_8$ (4316.27): C, 38.96; H, 3.92; N, 7.14; Found: C, 38.84; H, 4.48; N, 7.55. **MS** (HR – ESI – TOF, *m/z*): Calculated for $C_{112}H_{136}Cl_8N_{22}O_{24}Re_8$ [M + C_7H_8 – 8Cl]$^{8+}$, 470.0898. Found 470.0565.

3.5.4. Synthesis and characterization of [Re(CO)$_3$(*N,N'*-bidentante)Br] type complexes, C13 – C18

3.5.4.1. Preparation of C13

A dissolved amount of *fac*-$(Et_4N)_2[Re(CO)_3Br_3]$ (0.329 g, 0.427 mmol) in MeOH (5.00 mL) was added to a stirring MeOH (5.00 mL) solution of **L1** (0.103 g, 0.427 mmol). The reaction proceeded at room temperature for 3 hours and a yellow precipitate was filtered, washed with MeOH and CH_2Cl_2. Thereafter, the solid product was dried under high vacuum.

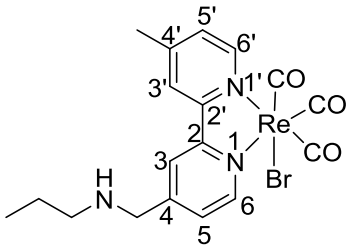

C13

Compound **C13**: Pale yellow solid, yield: 0.192 g (76.0%). **IR**: ATR, ν/cm^{-1}: 2027 (s, carbonyl, CO), 1914 (s, carbonyl, CO), 1867 (s, carbonyl, CO). **^{1}H NMR** (400 MHz, $(CD_3)_2SO$): δ = 0.84 (m, 3 H, C**H$_3$**CH$_2$CH$_2$), 1.46 (m ,2H, CH$_3$C**H$_2$**CH$_2$), 2.38 (s, 3H, 4'-CH$_3$), 2.44 (overlapping t, 2H, CH$_3$CH$_2$C**H$_2$**), 3.75, (s, 1H, 4'-CH$_3$), 3.91 (s, 2H, 4-CH$_2$), 7.53 (d, 1H, ^2J = 5.84 Hz, H-5'), 7.68 (d, 1H, ^2J = 5.68 Hz, H-5), 8.61 (s, 1H, H-3'), 8.67 (s, 1H, H-3), 8.81 (d, 1H, ^2J = 5.68 Hz, H-6'), 8.88 (d, 1H, ^2J = 5.68 Hz, H-6).**^{13}C{^{1}H} NMR** (100.60 MHz, $(CD_3)_2SO$): δ = 11.6 (**C**H$_3$CH$_2$CH$_2$), 20.9 (4'-CH$_3$), 23.5(CH$_3$**C**H$_2$CH$_2$), 61.8 (CH$_3$CH$_2$**C**H$_2$), 62.4 (4-CH$_2$), 122.0 (C-3), 125.1 (C-5), 126.5 (C-5'), 128.3 (C-3'), 152.2 (C-6), 152.3 (C-4), 152.6 (C-6'), 152.8 (C-4'), 155.0 (C-2, C-2'), 189.8, 197.6 (CO). **Elemental analysis** (%): Calculated for $C_{18}H_{19}BrN_3O_3Re$ (591.48): C, 36.55; H, 3.24; N, 7.40; Found: C, 36.83; H, 3.33; N, 6.81. **MS** (HR – ESI – TOF, *m/z*): Calculated for $C_{18}H_{19}BrN_3O_3Re$ [M – Br]$^+$, 512.0984. Found 512.0985. **MP:** 193 – 195 °C.

3.5.4.2. Preparation of C14

A synthetic procedure analogous to that of **C13** was followed for the synthesis of **C14**. *fac*-$(Et_4N)_2[Re(CO)_3(Br)_3]$ (0.221 g, 0.287 mmol) and **L2** (0.750 g, 0.0718 mmol) were reacted to afford. **C14** as a yellow precipitate.

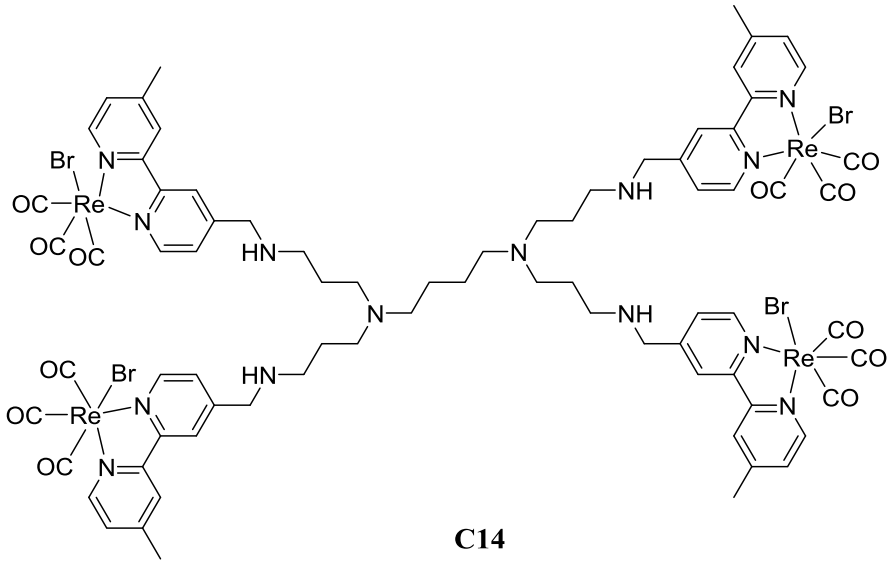

C14

Compound **C14**: Yellow solid, yield: 0.139 g (79.0%). **IR**: ATR, ν/cm^{-1}: 2016 (s, carbonyl, CO), 1877 (br, carbonyl, CO). **^{1}H NMR** (400 MHz, $(CD_3)_2SO$): δ = 1.54 – 1.78 (broad signals $NCH_2C\mathbf{H_2}C\mathbf{H_2}CH_2N$, $NCH_2C\mathbf{H_2}CH_2N$), 2.54 – 2.88 (overlapping signals, $NCH_2CH_2C\mathbf{H_2}NH$, $NC\mathbf{H_2}CH_2CH_2NH$, $NC\mathbf{H_2}CH_2CH_2C\mathbf{H_2}N$, NH, 4'-CH3), 3.98 (br s, 8H, 4-CH_2), 7.58 (br d, 4H, H-5'), 7.72 (br d, 4H, H-5), 8.65 (br s, 4H, H3'), 8.75 (br s, 4H, H-3), 8.85 (br d, 4H, H6'), 8.93 (br d, 4H, H-6). **^{13}C{^{1}H} NMR** (100.60 MHz, $(CD_3)_2SO$): δ = 21.4 (4'-CH_3), 31.1 ($NCH_2\mathbf{C}H_2\mathbf{C}H_2CH_2N$), 46.9, 49.1 – 52.9 ($N\mathbf{C}H_2CH_2CH_2NH$, $NCH_2CH_2\mathbf{C}H_2NH$, $NCH_2\mathbf{C}H_2CH_2N$, 4-CH_2, $N\mathbf{C}H_2CH_2CH_2\mathbf{C}H_2N$), 123.7 (C-3), 125.3 (C3'). 127.2, 127.1 (C-5, C-5'), 128.8 (C4), 152.7, 152.8 (overlapping signals C-6', C-6), 153.1 (C4'), 154.7 (C-2), 154.9 (C-2'), 189.5, 197.8, (CO). **Elemental analysis** (%)**:** Calculated for $C_{76}H_{80}Br_4N_{14}O_{12}Re_4.10H_2O$ (2626.16): C, 34.76; H, 3.84; N, 7.47; Found: C, 34.76; H, 3.53;

N, 7.36. Calculated for $C_{76}H_{80}Br_4N_{14}O_{12}Re_4$ $[M + 3H - Br]^{4+}$, 592.0524. Found 592.0241. **MP:** 182 – 184 °C.

3.5.4.3. Preparation of C15

To achieve **C15**, *fac*-$(Et_4N)_2[Re(CO)_3Br_3]$ (0.525 g, 0.0681 mmol) in MeOH (3.00 mL) was added to a stirring solution of **L3** (0.0380 g, 0.0170 mmol) in MeOH. The reaction proceeded at room temperature for 3 hours and the yellow precipitate was filtered, washed with MeOH and CH_2Cl_2, and dried under reduced pressure. Complex **C15** was isolated as a yellow solid.

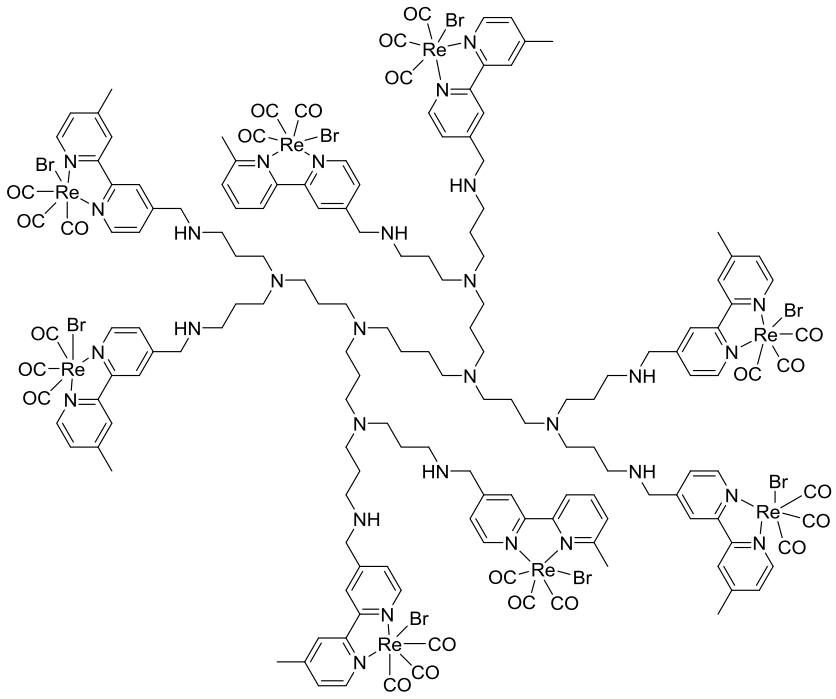

C15

Compound **C15**: Yellow solid, Yield: 0.0553g (64.6%). **IR**: ATR, ν/cm^{-1}: 2010 (s, carbonyl, CO), 1960, 1879 (br, carbonyl, CO). **^{1}H NMR** (400 MHz, $(CD_3)_2SO$): δ = (400 MHz, $CD_3)_2SO$): δ = 1.35 - 161 (br m, $NCH_2C\mathbf{H_2}C\mathbf{H_2}CH_2N$, $NCH_2C\mathbf{H_2}CH_2N$), 2.35 – 2.37 (m, 32H, $NCH_2C\mathbf{H_2}CH_2NH$, $NCH_2C\mathbf{H_2}CH_2N$, NH), 3.31 (br signal, 4'-CH_3, $NC\mathbf{H_2}CH_2C\mathbf{H_2}N$, $NC\mathbf{H_2}CH_2CH_2C\mathbf{H_2}N$, $NC\mathbf{H_2}CH_2C\mathbf{H_2}NH$), 3.89 (s, 16H, 4-$CH_2$), 7.54 – 7.65 (br d,16H, H-5', H-5), 8.58 – 8.66 (m, 16H, H-3', H-3), 8.82 - 8.88 (m, 16H, H-6', H-6). **^{13}C{^{1}H} NMR**

(100.60 MHz, $(CD_3)_2SO$): δ = 21.16 – 21.37 (overlapping peaks 4'-CH_3, $NCH_2\mathbf{CH_2}\mathbf{CH_2}CH_2N$, $NCH_2\mathbf{CH_2}CH_2N$, $NCH_2\mathbf{CH_2}CH_2NH$), 47.3, 51.6 – 52.0 (overlappig peaks $N\mathbf{CH_2}CH_2CH_2\mathbf{CH_2}N$, $N\mathbf{CH_2}CH_2\mathbf{CH_2}N$, $N\mathbf{CH_2}CH_2CH_2NH$, $N\mathbf{CH_2}CH_2CH_2\mathbf{CH_2}N$), 51.4 (4-$CH_2$), 123.5 (C-3), 125.2 (C-3'), 126.9 (C-5), 128.8 (C-5'), 147.0 (C-4'), 147.3 (C-4), 152.6 (C-6'), 152.9 (C-6), 155.3, 155.5 (overlapping peaks C-2, C-2'), 190.1, 197.8, (CO). **Elemental analysis:** Calculated for $C_{160}H_{176}Br_8N_{30}O_{24}Re_8$ (5032.24): C, 38.19; H, 3.53; N, 8.35; Found: C, 38.20; H, 4.68; N, 8.00. **MS** (HR – ESI – TOF, *m/z*): Calculated for $C_{160}H_{176}Br_8N_{30}O_{24}Re_8$ $[M + 4MeOH - 4Br]^{4+}$, 1210.0929. Found 1210.0341. **MP:** 158 – 161 °C.

3.5.4.4. Preparation of C16

fac-$(Et_4N)_2[Re(CO)_3Br_3]$ (0.862 g, 1.12 mmol) was dissolved in MeOH (5.00 mL) and added to a stirring solution of **L4** (0.168 g**,** 1.12 mmol**)** in MeOH (5.00 mL). The reaction was stirred for 3 hours and a white precipitate was filtered. Thereafter, the precipitate was washed with warm water (~30 °C) and recrystallized from EtOH to afford **C16** as colourless needles.

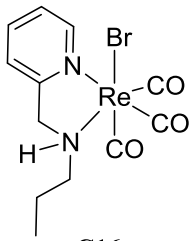

C16

Compound **C16**: White solid, yield: 0.321 g (57.0%). **IR**: ATR, *v*/cm^{-1}: 2012 (s, carbonyl, CO), 1912 (s, carbonyl, CO), 1875 (s, carbonyl, CO), 1672 (s, pyridyl, C═N). **^{1}H NMR** (400 MHz, $(CD_3)_2SO$): = 0.96 (t, 3H, ^3J = 7.41 Hz, $C\mathbf{H_3}CH_2CH_2$), 1.98 – 1.66 (m, 2H, $CH_3C\mathbf{H_2}CH_2$), 3.04 (m, 2H, $CH_3CH_2C\mathbf{H_2}$), 4.16 (dd, 1H, ^2J = 15.68 Hz, ^3J = 8.72 Hz, 2-$C\mathbf{H_2}$), 4.82 (dd, 1H, ^2J =15.72 Hz, ^3J = 5.08 Hz, 2-$C\mathbf{H_2}$), 5.07 (br m, NH), 7.57 (t, 1H, ^3J = 6.06 Hz, H5), 7.75 (d, 1H, ^3J = 7.84 Hz, H3), 8.09 (td, 1H, ^3J =7.75 Hz, 1.53 Hz,

H4), 8.77 (d, 1H, ^{3}J = 5.52 Hz, H6). **^{13}C{^{1}H} NMR** (101 MHz, $(CD_3)_2SO$): 11.0 ($\mathbf{C}H_3CH_2CH_2$), 21.6 ($CH_3\mathbf{C}H_2CH_2$), 59.7 ($CH_3CH_2\mathbf{C}H_2$, 2-CH_2), 122.6 (C-3), 125.1 (C-5), 139.6 (C-4), 152.4 (C-6), 160.4 (C-2), 191.9, 196.2, 197.7 (CO). **Elemental analysis** (%): Calculated for $C_{12}H_{14}BrN_2O_3Re$ (500.37): C, 28.81; H, 2.82; N, 5.60; Found: C, 28.92; H, 2.77; N, 5.42. **MS** (HR – ESI – TOF, *m/z*): Calculated for $C_{12}H_{14}BrN_2O_3Re$ $[M - Br]^+$, 421.0562. Found 421.0549. **MP:** 211 – 213 °C.

3.5.4.5. Preparation of C17

Complex **C17** was synthesized analogous to **C16**. *fac*-$(Et_4N)_2Re(CO)_3Br_3]$ (0.765 g, 0.993 mmol) and **L5** (0.169 g, 0.248 mmol) were used. A brown precipitate, **C17**, was filtered off, washed with warm water and dried under reduced pressure.

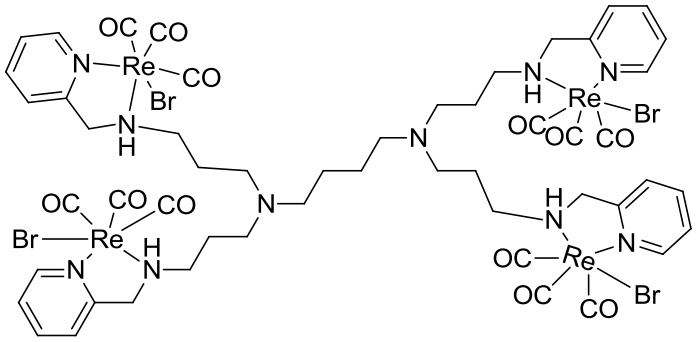

C17

Compound **C17**: Brown powder, yield: 0.169 g (19.5%). **IR**: ATR, ν/cm^{-1}: 2014 (s, carbonyl, CO), 1863 (br, carbonyl, CO), 1609 (s, pyridyl, C═N). **^{1}H NMR** (400 MHz, $(CD_3)_2SO$): δ = 1.53 (br signal, 4H, $NCH_2C\mathbf{H_2}C\mathbf{H_2}CH_2N$), 1.97 (br signal, 8H, $NCH_2C\mathbf{H_2}CH_2NH$), 2.91 – 3.25 (br m, 16 H, $NC\mathbf{H_2}CH_2CH_2NH$, $NCH_2CH_2C\mathbf{H_2}NH$), 4.17 (m, 4H, 2-CH_2), 4.47 (m, 4H, $NC\mathbf{H_2}CH_2CH_2C\mathbf{H_2}N$), 4.83 (m, 4H, 2-$CH_2$), 5.16 (br s, 4H, N**H**), 7.54 (m, 4H, H-5), 7.73 (m, 4H, H-3), 8.10 (m, 4H, H-4), 8.79 (br dd, 4H, H-6).**^{13}C{^{1}H} NMR** (101 MHz, $(CD_3)_2SO$): 24.1 ($NCH_2\mathbf{C}H_2\mathbf{C}H_2CH_2N$), 25.5 ($NCH_2\mathbf{C}H_2CH_2NH$), 51.1, 52.9 ($N\mathbf{C}H_2CH_2CH_2NH$. $NCH_2CH_2\mathbf{C}H_2NH$), 57.4 ($N\mathbf{C}H_2CH_2CH_2\mathbf{C}H_2N$), 59.6 (2-$CH_2$),

123.1 (C-3), 125.7 (C-5), 140.2 (C-4), 153.0 (C-6), 160.0 (C-2), 191.8, 196.2, 197.6 (CO). **Elemental analysis** (%): Calculated for $C_{52}H_{60}Br_4N_{10}O_{12}Re_4$ (2081.93): C, 30.01; H, 2.91; N, 6.73; Found: C, 30.18; H, 3.33; N, 6.65. **MS** (HR – ESI – TOF, *m/z*): Calculated for $C_{52}H_{60}Br_4N_{10}O_{12}Re_4$ $[M + 2H]^{2+}$, 1041.8850. Found 1041.9767. **MP:** 148 – 151 °C.

3.5.4.6. Preparation of C18

A 3.00 mL of MeOH was added in **L6** (0.0480 g, 0.0320 mmol) and allowed to stir until the ligand was dissolved completely. Thereafter, *fac*-$(Et_4N)_2[Re(CO)_3Br_3]$ (0.0980 g, 0.128 mmol) was then dissolved in MeOH (1.00 mL) and added to the stirring solution. The resulting precipitate was maintained in the stirring solution for 3 hours and subsequently filtered to afford a brown solid. The solid was washed with warm water and dried under reduced pressure to afford **C18**.

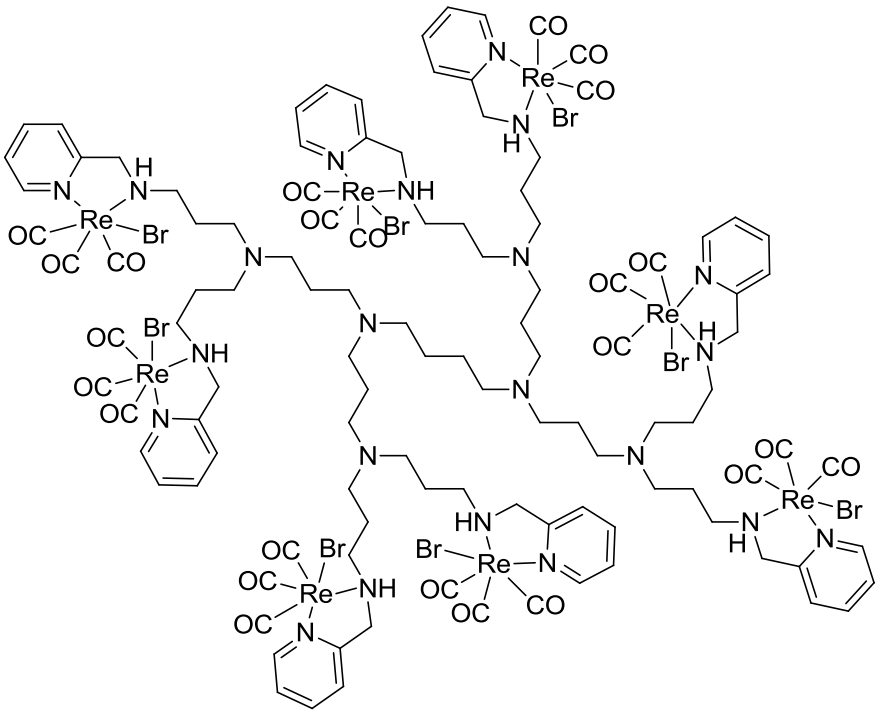

C18

Compound **C18**: Brown powder, yield: 0.0248 g (18.0%). **IR**: ATR, ν/cm^{-1}: 2014 (s, carbonyl, (CO), 1865 (br, carbonyl, CO), 1610 (s, pyridyl, C═N). **^{1}H NMR** (400 MHz, $(CD_3)_2SO$): δ = 1.70 – 1.88, 2.98 – 3.32 (br signals, 40H , $NCH_2C\mathbf{H_2}C\mathbf{H_2}CH_2N$,

NC**H₂**CH₂C**H₂**NH, NCH₂C**H₂**CH₂NH, NC**H₂**CH₂C**H₂**N, NCH₂C**H₂**CH₂N, NC**H₂**CH₂CH₂C**H₂**N), 4.19 (br m, 8H, NH), 4.50 (m, 8H, 2-CH_2), 5.07, 4.85 (br d, 8H, 2-CH_2), 7.55 (br t, 8H, H-5), 7.70 (br s, 8H, H-3), 8.07 (m, 8H, H-4), 8.74 (m, 8H, H-6). **$^{13}C\{^1H\}$ NMR** (100.60 MHz, $(CD_3)_2SO$): 25.9 (NCH₂**C**H₂**C**H₂CH₂N), 49.4, 50.1 – 57.0 (N**C**H₂CH₂**C**H₂NH, NCH₂**C**H₂CH₂NH, NCH₂**C**H₂CH₂N, N**C**H₂CH₂**C**H₂N, N**C**H₂CH₂CH₂**C**H₂N), 60.4 (2-CH_2), 123.2 (C-3), 125.7 (C-5), 140.3 (C-4), 152.9 (C-6), 160.9 (C-4), 192.5, 196.7, 198.3 (CO). **Elemental analysis** (%): Calculated for $C_{112}H_{136}Br_8N_{22}O_{24}Re_8$ (4303.34): C, 31.26; H, 3.19; N, 7.16; Found: C, 31.35; H, 3.77; N, 7.30. **MS** (HR – ESI – TOF, *m/z*): Calculated for $C_{112}H_{136}Br_8N_{22}O_{24}Re_8$ $[M + 3H - Br]^{4+}$, 1056.6145. Found 1056.5388. **MP**: 140 – 143 °C

3.5.5. Synthesis and characterization of *fac*-[Re(CO)₃(*N,N'*-bidentate)OH₂]⁺ type complexes, C19 – C24

3.5.5.1. Preparation of C19

fac-$(Et_4N)_2[Re(CO)_3Br_3]$ (0.100 g, 0.130 mmol) was dissolved in water (6.00 mL) and the solution was adjusted to pH 2.2 using HNO_3. Silver nitrate (0,066g, 0.389 mmol) was added to the solution and the suspension was stirred for 24 hours to afford a *fac*-$[Re(CO)_3(H_2O)_3]NO_3$ solution. Subsequently, AgBr was filtered and the filtrate was transferred to a round bottomed flask containing **L1** (0.0314g, 0.130 mmol). The solution was stirred for 4 hours and **C19** was filtered as a yellow solid.

Compound **C19**: Yellow solid, yield: 0.972 g. **IR**: ATR, ν/cm^{-1}: 2022 (s, carbonyl, CO), 1891 (s, carbonyl, CO), 1618 (br, bipyridyl, C═N). **^1H NMR** (300 MHz, $(CD_3)_2SO$): δ = 0.95 (m, 3 H, C**H₃**CH₂CH₂), 1.69 (m ,2H, CH₃C**H₂**CH₂), 2.59 (s, 3H, 4'-CH_3), 3.05 (br signal, 2H, CH₃CH₂C**H₂**), 4.44, 4.46 (overlapping signal, 2H,4-CH_2), 7.79 (m, 1H, H-5'), 8.53 – 9.19 (m, 5H, H-5, H-3', H-3, H-6', H-6). **Elemental analysis** (%):

Calculated for $C_{18}H_{21}N_3O_4Re.2HNO_3$ (655.61): C, 32.98; H, 3.54; N, 10.68; Found: C, 33.06; H, 4.17 N, 10.45. **MS** (HR – ESI – TOF, *m/z*): Calculated for $C_{18}H_{21}N_3O_4Re$ $[M - H_2O]^+$, 512.0984. Found: 512.0986. **MP**: 192 – 195 °C

3.5.5.2. Preparation of C20

fac-$[Re(CO)_3(H_2O)_3]NO_3$ (0.130 mmol) was synthesized in a similar manner as stated above. After filtering AgBr, the filtrate and **L2** (0.034g, 0.0325 mmol) were combined to form a mixture that was stirred for 4 hours. The resulting yellow precipitate was filtered to afford **C20**

Complex **C20**: Light brown solid, Yield: 0.109 g. **IR**: ATR, *v*/cm^{-1}: 2025 (s, carbonyl, CO), 1894 (s, carbonyl, CO), 1620 (br, bipyridyl, C═N). **^{1}H NMR** (300 MHz, $(CD_3)_2SO$): δ = 1.74 – 2.14 (br overlapping signals, 6H, $NCH_2C\mathbf{H_2}C\mathbf{H_2}CH_2N$, $NCH_2C\mathbf{H_2}CH_2NH$), 2.57 (s, 12H, 4'-CH3), 3.64 (br m, $NCH_2CH_2C\mathbf{H_2}NH$, $NC\mathbf{H_2}CH_2CH_2NH$, $NC\mathbf{H_2}CH_2CH_2C\mathbf{H_2}N$), 4.50 (m, 8H, 4-$CH_2$), 7.74 – 7.89 (m, 8H, H-5', H-5), 8.54 – 9.38 (m, 16H, H-3', H-3, H-6' and H-6). **Elemental analysis** (%): Calculated for $C_{76}H_{88}N_{14}O_{16}Re_4.4HNO_3.Et_4N.35H_2O$ (3211.28): C, 31.42; H, 5.71; N, 8.29; Found: C, 31.18; H, 5.52; N, 8.78. **MS** (HR – ESI – TOF, *m/z*): Calculated for $C_{76}H_{88}N_{14}O_{16}Re_4$ $[M + 2H_2O + Et_4N^+]^{5+}$, 472.5291. Found: 472.0348. **MP**: 132 – 135 °C.

3.5.5.3. Preparation of C21

L3 (0.0363 g, 0.0163 mmol) was stirred in a *fac*-$[Re(CO)_3(H_2O)_3]NO_3$ (0.130 mmol) solution for 4 hours. The resulting yellow precipitate was filtered to give **C21**.

Complex **C21**: Yellow solid, Yield: 0.109 g. **IR**: ATR, *v*/cm^{-1}: 2022 (s, carbonyl, CO), 1884 (s, carbonyl, CO), 1620 (br, bipyridyl, C═N).). **Elemental analysis** (%): Calculated for $C_{160}H_{192}N_{30}O_{32}Re_8.4HNO_3.Et_4N$ (5645.34): C, 41.20; H, 4.43; N, 9.97; Found:

C, 41.40; H, 4.33; N, 10.29. **MS** (HR – ESI – TOF, *m/z*): calculated for $C_{160}H_{192}N_{30}O_{32}Re_8$ $[M + HNO_3 + 8Et_4N^+]^{16+}$, 352.8338. Found: 352.9930. **MP**: 179 – 182 °C.

3.5.5.4. Preparation of C22

fac-$(Et_4N)_2[Re(CO)_3(Br)_3]$ (0.100 g, 0.130 mmol) was dissolved in water (6.00 mL) and the solution was adjusted to pH 2.2 using HNO_3. Silver nitrate (0.066g, 0.389 mmol) was added to the solution and the suspension was stirred for 24 hours to afford *fac*-$[Re(CO)_3(H_2O)_3]NO_3$ (0.130 mmol) in solution. Subsequently, AgBr was filtered off and **L4** (0.0195g, 0.130 mmol) dissolved in the filtrate, the solution was stirred for 10 hours. The product remained in solution and water was removed using a freeze drier to afford a colourless suspension.

Compound **C22**: Colourless suspension, yield: 0.674 g. **IR**: ATR, ν/cm^{-1}: 2022 (s, carbonyl, CO), 1891 (s, carbonyl, CO), 1624 (s, pyridyl, C═N). **^{1}H NMR** (300 MHz, $(CD_3)_2SO$): = 0.83 (t, 3H, ^3J = 7.46 Hz, C**H$_3$**CH_2CH_2), 1.59 (m, 2H, CH_3C**H$_2$**CH_2), 2.94 (t, 2H, ^3J = 7.71 Hz, CH_3CH_2C**H$_2$**), 4.26 (br m, 2H, 2-C**H$_2$**), 7.47 – 7.55 (m, 2H, H5, H3), 7.96 (td, 1H, ^3J =7.77, 1.73, H4), 8.52 (d, 1H, ^3J = 5.13, H6). **^{13}C{^{1}H} NMR**. **Elemental analysis** (%): Calculated for $C_{12}H_{16}N_2O_4Re$ (438.48): C, 32.87; H, 3.86; N, 6.39; Found: C, 32.23; H, 3.45; N, 7.00. **MS** (HR – ESI – TOF, *m/z*): Calculated for $C_{12}H_{16}N_2O_4Re$ $[M - H_2O]^+$, 421.0562. Found 421.0560.

3.5.5.5. Preparation of C23

A *fac*-$[Re(CO)_3(H_2O)_3]NO_3$ (0.130 mmol) solution was added to **L5** (0.0221 g, 0.0325 mmol), the reaction was stirred for 10 hours. The resulting solution was freeze dried (minimally) to give a colourless suspension.

Compound **C23**: colourless suspension, yield: 0.107 g. **IR**: ATR, ν/cm^{-1}: 2020 (s, carbonyl, CO), 1881 (s, carbonyl, CO), 1644 (s, pyridyl, C═N). **^{1}H NMR** (400 MHz, $(CD_3)_2SO$): = 1.71 (br signal, 4H, NCH_2C**H$_2$**C**H$_2$**CH_2N), 2.09 (br signal, 8H,

$NCH_2C\mathbf{H_2}CH_2NH$), 2.83 – 3.13 (br m, 16 H, $NC\mathbf{H_2}CH_2CH_2NH$, $NCH_2CH_2C\mathbf{H_2}NH$), 4.94 – 5.00 (br signal, 16H, $NC\mathbf{H_2}CH_2CH_2C\mathbf{H_2}N$, 2-$C\mathbf{H_2}$, N**H**), 7.45 – 7.53 (m, 8H, H-5, H-3), 7.93 (m, 4H, H-4), 8.67 (m, 4H, H-6). **Elemental analysis** (%): Calculated for $C_{52}H_{68}N_{10}O_{16}Re_4.5HNO_3$ (2149.06): C, 29.06; H, 3.42; N, 9.78; Found: C, 29.39; H, 3.13; N, 9.60. **MS** (HR – ESI – TOF, *m/z*): Calculated for $C_{52}H_{60}N_{10}O_{14}Re_4$ $[M + 2H]^{2+}$, 898.6299. Found 898.7490.

3.5.5.6. Preparation of C24

A *fac*-$[Re(CO)_3(H_2O)_3]NO_3$ (0.130 mmol) solution was added to **L6** (0.0244 g, 0.0163 mmol), the reaction was stirred for 10 hours. The product was freeze-dried to afford C24 as a brown suspension.

Compound **C24**: brown suspension. **IR**: NaCl cell, ν/cm^{-1}: 2015 (s, carbonyl, CO), 1863 (s, carbonyl, CO), 1621 (s, pyridyl, C═N). **Elemental analysis** (%): Calculated for $C_{112}H_{152}N_{22}O_{32}Re_8.15HNO_3.Et_4N$ (4883.66): C, 29.90; H, 3.89; N, 10.75; Found: C, 29.54; H, 3.43; N, 10.54. **MS** (HR – ESI – TOF, *m/z*): Calculated for $C_{112}H_{152}N_{22}O_{32}Re_8$ $[M + 30H_2O + 2Et_4N^+]^{10+}$, 460.9781. Found 461.0756.

3.6. References

1. J. R. Dilworth, S. J. Parrott, *Chem. Soc. Rev.*, 1998, **27**, 43 – 55.
2. R. Alberto, E. Abram, K. Hegetschweiler, P. A. J. Schubiger, *Chem. Soc. Dalton Trans.,* 1994, 2815.
3. R. Alberto, R. Schibli, R. Waibel, U. Abram, P. A. Schubiger, *Coord. Chem. Rev.,* 1999, **192**, 901 – 919.
4. R. Alberto, R. Schibli, A. Egli, A. P. Schubiger, *J. Am. Chem. Soc.,* 1998, **120**, 7987 – 7988.
5. R. Alberto, *J. Organomet. Chem.*, 2007, **692**, 1179 – 1186.
6. R. Alberto, H. Braband, H. W. P. N'Dongo, *Curr. Radiopharm.*, 2009, **2**, 254 – 267.
7. G. E. Kodina, A. O. Malysheva, O. E. Klement'eva, A. A. Inkin, N. I. Gorshkov, A. A. Lumpo, D. N. Suglobov, *J. Nucl. Radiochem. Sci.,* 2005, **6**, 183 – 185.
8. W. A. Herrmann, R. Alberto, J. C. Bryan, A. P. Sattelberger, *Chem. Ber.*, 1991, **124**, 1107 – 1111.
9. R. Alberto, R. Schibli, A. Egli, A. Schubiger, W. A. Herrmann, G. Artus, U. Abram, T. A. Kaden, *J. Organomet. Chem.*, 1995, **493**, 119 – 127.
10. A. Del Guerzo, S. Leroy, F. Fages, R. H. Schmehl, *Inorg. Chem.*, 2002, **41**, 359 – 366.
11. H. M. Mcconnell, *J. Chem. Phys.,* 1958, **28**, 430.
12. M. Cohn, T. R. Hughes Jr., *J. Biol. Chem.*, 1962, **237**, 176 – 181.
13. M. Prudêncio, J. Rohovec, J. A. Peters, E. Tocheva, M. J. Boulanger, M. E. P. Murphy, H-J. Hupkes, W. Kosters, A. Impagliazzo, M. Ubbink, *Chem. Eur. J.*, 2004, **10**, 3252 – 3260.
14. S. R. Banerjee, M. K. Levadala, N. Lazarova, L. Wei, J. F. Valliant, K. A. Stephenson, J. W. Babich, K. P. Maresca, J. Zubieta, *Inorg. Chem.*, 2002, **41**, 6417 – 6425.

15. J. Granifo, *Polyhedron*, 1999, **18**, 1061 – 1066.

16. J. F. G. A. Jansen, E. M. E. de Brabander-van den Berg, E. W. Meijer, *Science*, 1994, **266**, 1226 – 1269.

17. V. Fernandez-Moreira, F. L. Thorp-Greenwood, R. J. Arthur, B. M. Kariuki, R. L. Jenkins, M. P. Coogan, *Dalton Trans.*, 2010, **39**, 7493 – 7503.

18. M. M. Saw, P. Kurz, N. Agorastos, T. S. Andy Hor, F. X. Sundram, Y. K. Yan, R. Alberto, *Inorg. Chim. Acta*, 2006, **359**, 4087 – 4094.

19. S. A. Moya, J. Guerrero, R. Pastene, R. Schmidt, R. Sariego, R. Sartori, J. Sanz-Aparicio, I. Fonsceca, M. Martinez-Ripoll, *Inorg. Chem*., 1994, **33**, 2341 – 2346.

20. T. R. Hayes, B. B. Kasten, C. L. Barnes, P. D. Benny, *Dalton Trans.*, 2014, **43**, 6998 – 7000.

21. S. Mundwiler, S. M. Kundig, K. Ortner, R. Alberto, *Dalton Trans.,* 2004, 1320 − 1328.

22. A. Brink, H. G. Visser, A. Roodt, *Inorg. Chem.*, 2014, **53**, 12480 – 12488.

23. J. Xia, Y. Wang, J. Yu, J. Cao, C. Zhang, D. Yin, *J. Radioanalyt. Nucl. Chem*., 2005, **266**, 313 – 316.

24. A. Egli, K. Hegetschweiler, R. Alberto, U. Abram, R. Schibli, R. Hedinger, V. Gramlich, R. Kissner, P. A. Schubiger, *Organomet.,* 1997, **16**, 1833 – 1840.

25. N. Lazarova, S. James, J. Babich, J. Zubieta, *Inorg. Chem. Comm.,* 2004, **7**, 1023 – 1026.

26. R. Alberto, R. Schibli, P. A Schubiger, *Polyhedron*, 1996, **15**, 1079 – 1089.

27. P. V. Grundler, L. Helm, R. Alberto, A. E. Merbach, *Inorg. Chem.,* 2006, **45**, 10378 – 10390.

28. Bruker SAINT-PLUS (including XPREP). Version 7.12, Bruker AXS Inc., Madison, WI (2004).

29. Bruker SADABS. Version 2004/1. Bruker AXS Inc., Madison, WI (1998).

30. G. M. Sheldrick, *Acta Cryst*., 2008, **A64**, 112 – 122.

31. L. J. Farrugia, *J. Appl. Cryst*., 1999, **32**, 837 – 838.

32. K. Brandenburg, H. Putz, DIAMOND. Release 3.0e. *Crystal Impact GbR*, Postfach 1251, D-53002, Bonn, Germany (2004).

33. V. Wing Wa Yam, Y. Yang, J. Zhang, B. Wai-Kin Chu, N. Zhu, *Organometallics,* 2001, **20**, 4911 – 4918.

34. M. Schutte, G. Kemp, H. G. Visser, A. Roodt, *Inorg. Chem.*, 2011, **50**, 12486 – 12498.

Chapter 4

Substitution kinetic investigations

4.1. Rationale behind the study

This chapter forms part of a preliminary investigation into the intimate mechanism of the ligand substitution processes of dendritic complexes containing more than one rhenium metal centre. Herein, the intention is to find out if the metal ions 'communicate' with each other through dendrimer ligands and overall complex charge, in spite of being substantially removed from each other *via* the dendritic branches (in terms of distance). To perform this, a monomeric complex, **LM1** (**M1** = one *fac*-$[Re(CO)_3MeOH]^+$ core) was chosen as a model, after which dendritic complexes, **LM4** (four *fac*-$[Re(CO)_3MeOH]^+$ cores) and **LM8** (eight *fac*-$[Re(CO)_3MeOH]^+$ cores) were synthesized and the substitution of methanol with various ligands were attempted.

A systematic attempt to describe the kinetics, starting with the model complex **LM1** and moving towards the highest dendrimer generation will be discussed.

4.2. General introduction

The understanding of the dynamics of the Re–$MeOH/H_2O$ bond, bond substitution and stability in a controlled environment may give a predictive kinetic pattern of $[2 + 1]^1$ labeled metallodendrimers in biological environments. *In vivo*, nucleophiles of varying basicity are ubiquitous and can readily compete for the 'labile site' in *fac*-$[M(N,N\text{-bidentate})(CO)_3OH_2]^+$ (M = ^{99m}Tc or $^{188/186}Re$) systems. Kinetic studies give an indication of the rate at which a chemical reaction proceeds permitting the identification of the intimate mechanism (*i.e.* associative interchange (I_a) or dissociative interchange (I_d) mechanism) of the reaction. The labeling of biomolecules, such as dendrimers, with the isoLink® kit requires the substitution

of at least one of the relatively labile aqua ligands from *fac*-[^{99m}Tc(CO)$_3$(OH$_2$)$_2$]$^+$.[2] By far, the kinetic behaviour of Re(I) metallodendrimers (metal containing dendrimers) as models for ^{99m}Tc(I) labeled complexes and the rate of aqueous substitution on *fac*-[Re(*N,N*-dendrimer)(CO)$_3$OH$_2$]$^+$ complexes by different nucleophiles, has not been reported in the literature.

4.3. Experimental

4.3.1. Chemical reagents

All chemicals were purchased from Sigma-Aldrich and Merk and were used without further purification. MeOH was dried in calcium hydride. The synthesis of the aqua complexes is reported in **Chapter 3**, *Section 3.5.5.4 – 6.*

4.3.2. Spectroscopic methods

The kinetic measurements were initially performed on a Varian Cary 50 Conc UV/vis spectrophotometer equipped with a Julabo F12-mV temperature cell regulator (accurate within 0.1 °C). The kinetic reactions of coordinated methanol substitution were observed to occur rapidly under UV/vis. Thus, rapid kinetic reactions (reaction half-lives shorter than 20 seconds) were monitored at four different temperatures 5.00 °C, 15.0 °C, 25.0 °C and 35.0 °C (accurate within 0.1 °C) on Kinet Asyst™ Hi-Tech Scientific M300 SHU-615X2 Stopped Flow Spectrophotometer attached to a Julabo MPV thermostat water bath (accurate within 0.1 °C). The third generation stopped-flow system has a thermostatic sample handling unit and can be operated in the diode-array mode with a dead time < 5.00 microseconds, yielding 400 nm spectral width scans at < 5.00 microseconds per complete scan. The Scientist Micromath, Version 2.01 program and Microsoft Office Excel 2014 were used to fit the output data to the specific functions.

4.3.3. Data treatment

In all linear and non-linear plots, the individual experimental data points are correlated by the solid line representing the computer least-squares fits of data and the kinetic data points reported per concentration represent an average of 7 individual traces. All the kinetic runs were performed under *pseudo* first-order conditions with the ligand in excess.[3] It was assumed that all the aqua complexes (**C22**, **C23** and **C24** in **Chapter 3**) are converted to their corresponding methanol complexes (**LM1**, **LM4** and **LM8**, respectively) upon dissolution in methanol, as observed in previous studies.[2-7] Also, the UV/vis spectra of **LM1**, **LM4** and **LM8** are analogous to their corresponding large scale MeOH complexes, characterized by IR spectroscopy in **Chapter 3**.

The simple equilibrium for a monomeric complex undergoing substitution under *pseudo* first-order conditions is given in **Scheme 4.1**. The rate constants k_1 and k_{-1} are calculated from the graph of k_{obs} *vs* [L], where k_1 is the gradient and k_{-1} is the intercept as given by **Equation 4.2**.[4] The *pseudo* first-order observed rate constant, k_{obs}, is determined by a least square fit of the absorbance *versus* time for a corresponding reaction.[4] The stability constants, K_1, were kinetically determined using **Equation 4.1** in **Scheme 4.1**.[4]

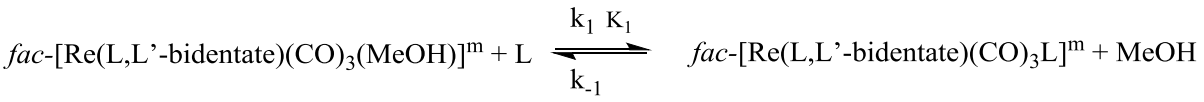

$K_1 = k_1/k_{-1}$ **Equation 4.1**

$k_{obs} = k_1[L] + k_{-1}$ **Equation 4.2**

Scheme 4.1: The parameters of a *pseudo* first-order reaction. K_1 represents the stability constant, k_1 denotes the rate constant and k_{obs} represents the 'observed' rate constant (obtained experimentally).[4]

The charge of the complex is represented by *m* and is dependent on the nature of the monodentate ligand (X) in the final product. Investigations under *pseudo* first-order conditions eliminate difficulties encountered when two reagents are investigated

simultaneously. The sum of the orders of the reactants gives the total order of the rate law. The order is the way in which the reaction rate varies with a change in concentration of one or both of the reacting species. These values can only be determined experimentally and it is often not trivial. Thus under *pseudo* first-order conditions, one reactant concentration is kept constant throughout the experiment and the other is varied (*i.e.* [L] >>> [Re]).[8,9] To obtain the standard entropy change of activation, $\Delta S^{\ddagger}$, and the standard enthalpy change of activation, $\Delta H^{\ddagger}$, the logarithmic form of the Eyring equation (**Equation 4.3**) is used.

$$\ln \frac{k}{t} = \ln \frac{K_B}{h} - \frac{\Delta H^{\ddagger}}{RT} + \frac{\Delta S^{\ddagger}}{RT} \quad \text{……Equation 4.3}$$

R is the gas constant, K_B is Boltzmann constant and h denotes Planck's constant. Thus, by plotting $\ln \frac{k}{t}$ *versus* $\frac{1}{T}$, a linear plot with the gradient $-\frac{\Delta H^{\ddagger}}{RT}$ and the intercept $\ln \frac{K_B}{h} + \frac{\Delta S^{\ddagger}}{RT}$ is obtained, hence $\Delta S^{\ddagger}$ and $\Delta H^{\ddagger}$ can be solved. The Eyring equation substantiates the type of substitution mechanism involved.

Since Re(I)-aqua complexes often polymerize in less acidic aqueous solutions,[4,10] and because they are able to form different species in solution (hydroxo *versus* aqua), the aqua ligand was substituted with MeOH ligand to eliminate the subtle uncertainties associated with pH factors. Furthermore, the dendritic complexes are not soluble in water, making comparison with the monomeric complex kinetics not viable (if different solvents are used). Therefore, the rates obtained in this study correspond to the Re(I)-methanol complexes which were characterized by IR spectroscopy (**Chapter 3**).

4.3.4. Substitution reactions of *fac*-[Re*N*-((pyridine-2-yl)methyl)propan-1-amine)$(CO)_3(OH_2)]^+$ (C22) in methanol with monodentate ligands.

The synthesis of **C22** was described in detail in **Chapter 3**. The stabilities of the complex as well as the entering ligands in methanol were tested and found to be stable for several hours by monitoring the solutions on a UV/vis spectrophotometer. The monodentate entering ligands chosen for the substitution reactions were pyridine (Py), bromide ion (Br^-) and 4-dimethylaminopyridine (DMAP). For these monodentate ligands, the reactions were followed at 5.0 °C, 15.0 °C, 25.0 °C and 35.0 °C to obtain the standard enthalpy change of activation ($\Delta H^{\ddagger}$) and standard entropy change of activation ($\Delta S^{\ddagger}$) for the reactions with DMAP and Py. The monomeric Re(I)-complex *fac*-[Re*N*-((pyridine-2-yl)methyl)propan-1-amine)$(CO)_3(OH_2)]^+$, **C22**, was dissolved in dry MeOH to afford the proposed corresponding Re(I)-methanol complex **LM1** in **Figure 4.1**.

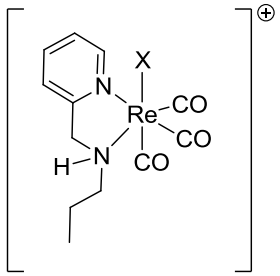

LM1

X = MeOH

[**LM1**] = 5.00 X 10^{-4} M

Figure 4.1: The proposed structure of *fac*-[Re*N*-((pyridine-2-yl)methyl)propan-1-amine)$(CO)_3(MeOH)]^+$ **LM1**.

Figure 4.2 represents a typical UV/vis spectrum shift for the slow reaction between *fac*-[Re*N*-((pyridine-2-yl)methyl)propan-1-amine)$(CO)_3(MeOH)]^+$ (**LM1**) and in this case pyridine. The insert in **Figure 4.2** represents the change in absorbance *versus* time.

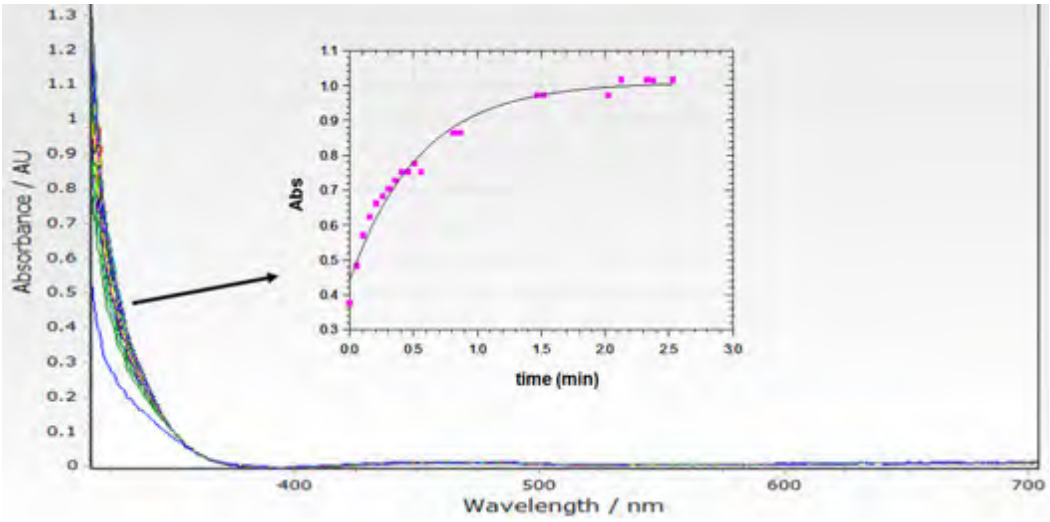

Figure 4.2: Typical UV/vis spectral change for the MeOH substitution reaction of *fac*-[Re*N*-((pyridine-2-yl)methyl)propan-1-amine)$(CO)_3(MeOH)]^+$ (**LM1**) with pyridine in MeOH at 15.0 °C. [**LM1**] = 5.00×10^{-4} M, [Pyridine] = 0.035 M, λ = 317 nm.

4.3.4.1. ***LM1*** *+ pyridine (Py)*

The methanol substitution reactions between *fac*-[Re*N*-((pyridine-2-yl)methyl)propan-1-amine)$(CO)_3(MeOH)]^+$ (**LM1**) and pyridine as entering ligand were investigated. The reactions were followed at 317 nm at four temperatures 5.0 °C, 15.0 °C, 25.0 °C and 35.0 °C. A k_{obs} *versus* [Py] plot yielded a straight line displayed in **Figure 4.3** and the data were fitted to **Equation 4.1** to obtain the rate data in **Table 4.1**.

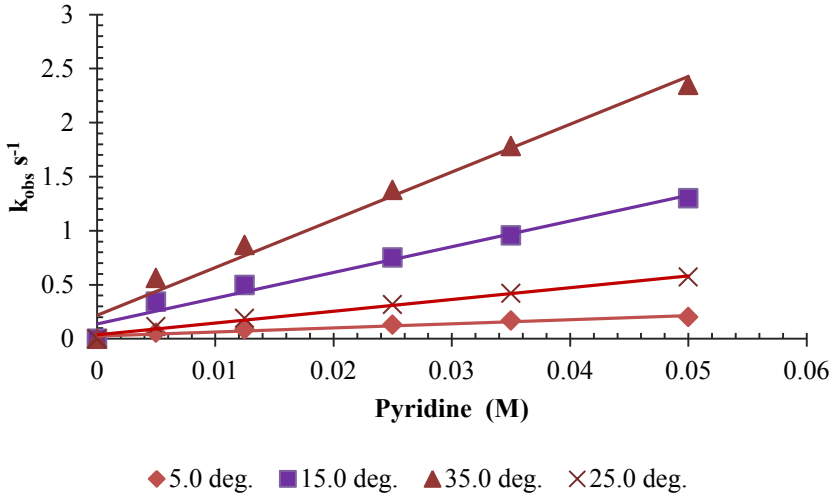

Figure 4.3: Plots of k_{obs} *versus* [Ligand] (Ligand = Pyridine) obtained using [**LM1**] = 5.00×10^{-4} M and [Pyridine] = 0.005 – 0.05 M.

The Eyring plot of $\ln \frac{k1}{t}$ *versus* $\frac{1}{T}$ to afford the activation parameters is illustrated in **Figure 4.4**. The solid line represents the best linear fit.

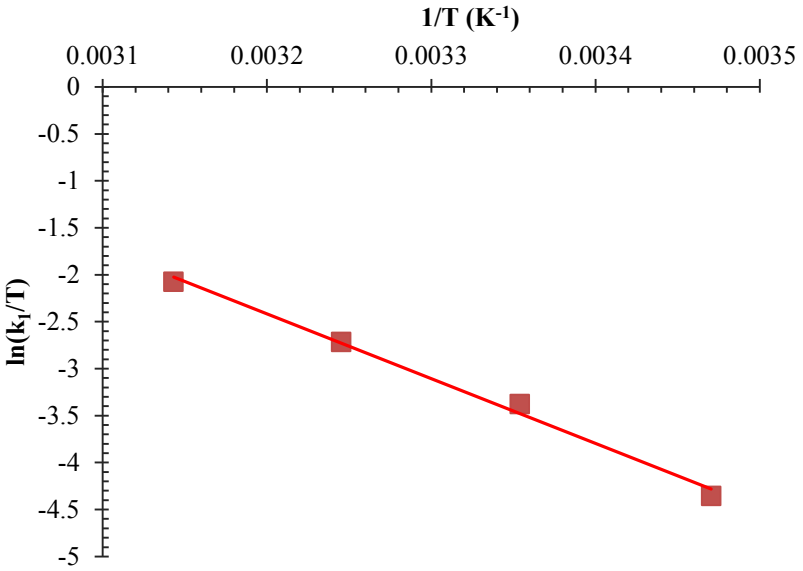

Figure 4.4: Erying plot of $\ln \frac{k1}{t}$ *versus* $\frac{1}{T}$ for the reaction between **LM1** and pyridine

The rate data were obtained from least square fits of the k_{obs} *vs* [Py] data to **Equation 4.2** while $\Delta S^{\ddagger}$ and $\Delta H^{\ddagger}$, in **Table 4.1**, were obtained from least square fits to **Equation 4.3**.

Table 4.1: Rate data for the reaction between **LM1** and Py between 5.0 – 35.0 °C.

Temperature	**5.0 °C**	**15.0 °C**	**25.0 °C**	**35.0 °C**
k_1 ($M^{-1}s^{-1}$)	1.80(1)	3.68(3)	10.2(1)	20.4(5)
k_{-1} (s^{-1})	0.025(7)	0.0382(1)	0.062(4)	0.24(3)
K_1 (M^{-1})	72(1)	96.3(6)	164(7)	85(3)

$\Delta S^{\ddagger}$	-34.1(10)$JK^{-1}mol^{-1}$
$\Delta H^{\ddagger}$	57(3) $KJmol^{-1}$

*4.3.4.2. **LM1** + 4-Dimethylaminopyridine (DMAP)*

Similarly, the MeOH substitution reactions between **LM1** and 0.005 – 0.05 M 4-dimethylaminopyridine (DMAP) were monitored between 5.0 – 35.0 °C. **Figure 4.5** represents the graph of k_{obs} *versus* [DMAP].

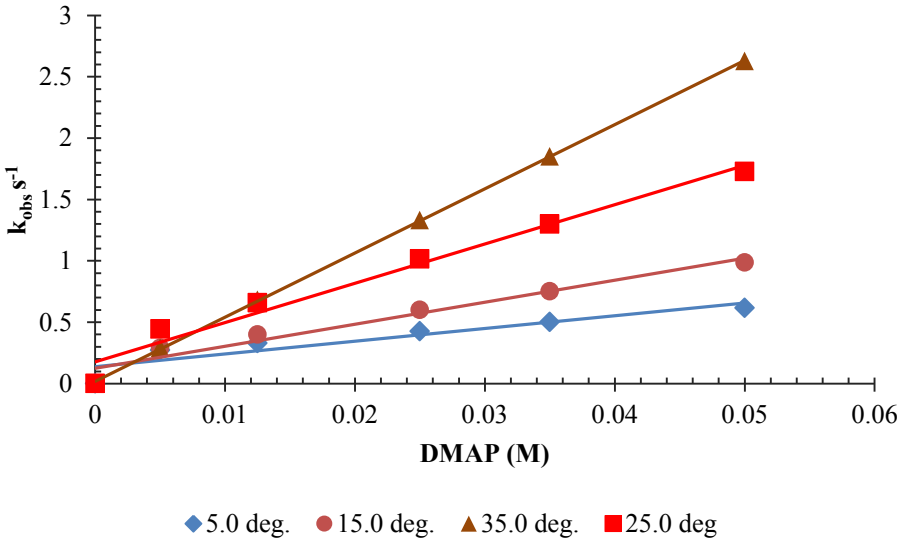

Figure 4.5: Plots of k_{obs} *versus* [Ligand] (Ligand = DMAP) obtained using [**LM1**] = 5.00 × 10^{-4} M and [DMAP] = 0.005 – 0.05 M.

Based on **Figure 4.5**, the experimental data to give k_{obs} *versus* [Ligand] plots is in accordance with the rate law. The Eyring plot of ln $\frac{k1}{t}$ *versus* $\frac{1}{T}$ to afford the activation parameters is shown in **Figure 4.6**. The solid line represents the best linear fit.

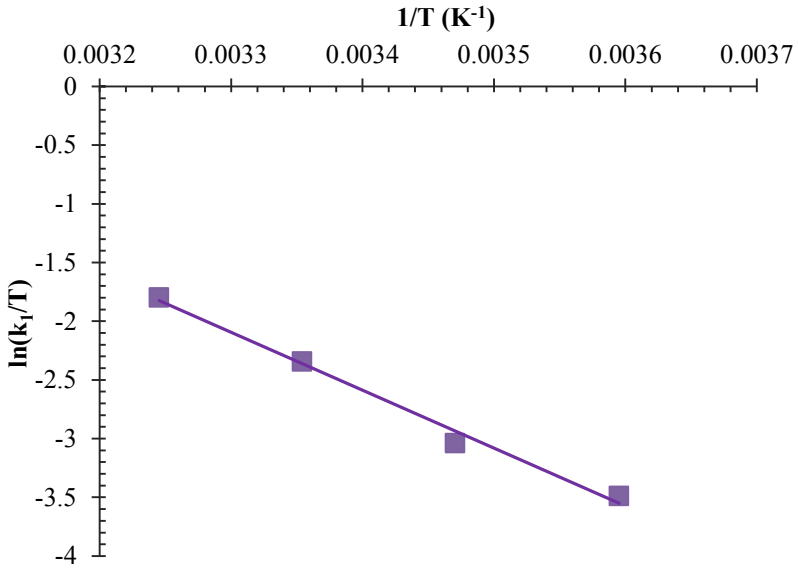

Figure 4.6: Erying plot of ln $\frac{k1}{t}$ *versus* $\frac{1}{T}$ for the reaction between **LM1** and DMAP at temperatures 5.0 °C, 15.0 °C, 25.0 °C and 35.0 °C.

The kinetic data was again fitted in **Equation 4.1** and the resulting rate constants were determined (summarized in **Table 4.2**).

Table 4.2: Summarized rate data for the reaction between **LM1** and DMAP between 5.0 – 35.0 °C.

Temperature	**5.0 °C**	**15.0 °C**	**25.0 °C**	**35.0 °C**
$k_1(M^{-1}s^{-1})$	8.57(7)	13.81(9)	28.7(1)	51.9(4)
k_{-1} (s^{-1})	0.202(8)	0.287(4)	0.301(3)	0.322(9)
$K_1(M^{-1})$	42.4(4)	48.0(9)	95.3(6)	161(9)

$\Delta S^{\ddagger}$	-79.1(9) $JK^{-1}mol^{-1}$
$\Delta H^{\ddagger}$	40(2) $KJmol^{-1}$

*4.3.4.3. **LM1** + Bromide ion (Br^-)*

The MeOH substitution kinetic reactions between 5.00×10^{-4} M **LM1** and 0.005 – 0.05 M tetraethylammonium bromide (Br^- ions) were monitored at 317 nm using a stopped-flow spectrophotometer. The Br^- ion was chosen to understand the influence of the anionic charge on cationic **LM1**. In **Figure 4.7**, the plot of k_{obs} *vs* [Br^-] at 25.0 ˚C, to afford the kinetic data summarised in **Table 4.3**, is displayed.

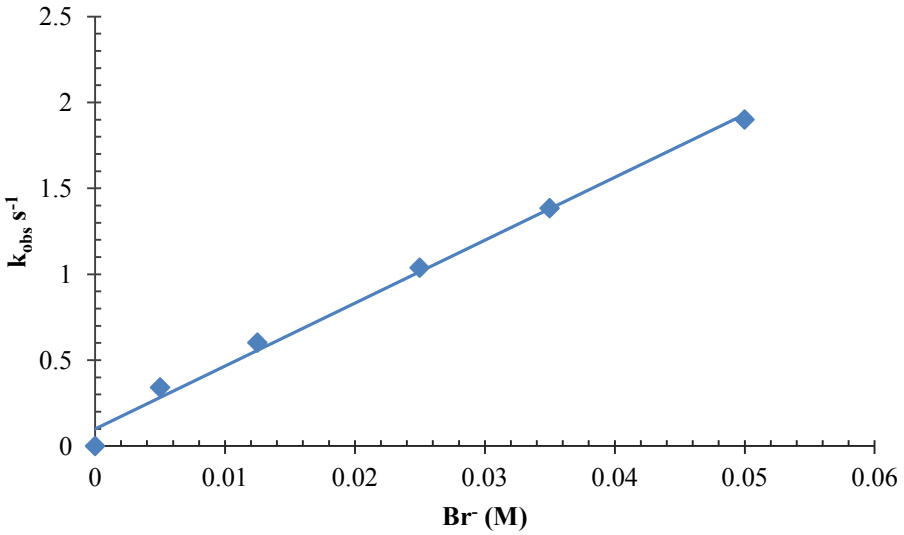

Figure 4.7: Plots of k_{obs} *versus* [Ligand] (Ligand = Br^-) at 25.0 ˚C obtained using [**LM1**] = 5.00×10^{-4} M and [Br^-] = 0.005 – 0.05 M.

Table 4.3: Reaction rate data for the reaction between **LM1** and Br^- at 25.0 °C.

Temperature	**25.0 °C**
$k_1(M^{-1}s^{-1})$	34.8(4)
k_{-1} (s^{-1})	0.165(1)
$K_1(M^{-1})$	211(2)

Since the reactions were monitored at a constant temperature, the activation parameters $\Delta S^{\ddagger}$ and $\Delta H^{\ddagger}$ were not determined.

4.3.4.4. Observations

At 25.0 °C, the second order rate constant, k_1, for the reactions of **LM1** with DMAP and Br^- are almost a factor of 3 faster than the comparative reactions with pyridine and is illustrated by **Figure 4.8**.

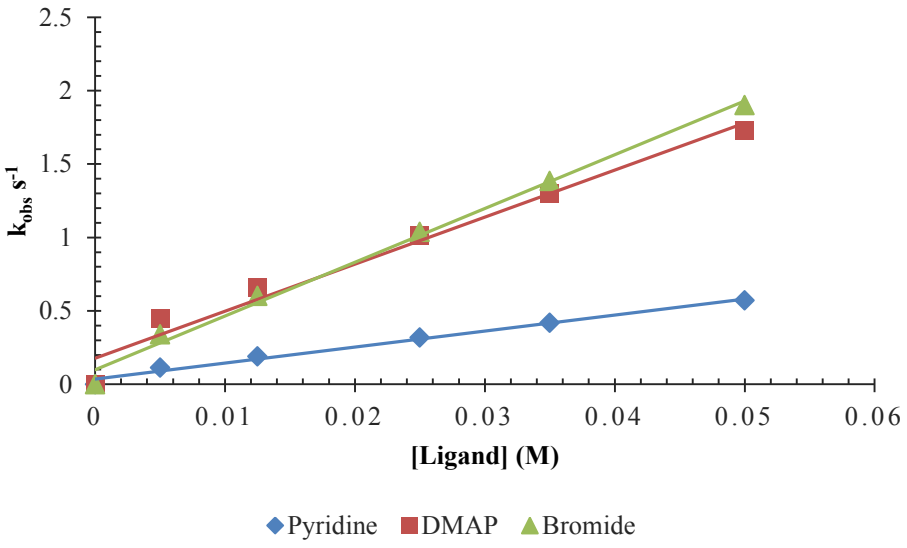

Figure 4.8: Plots of k_{obs} *versus* [Ligand] (Ligand = Pyridine, DMAP or Br^-) obtained using [**LM1**] = 5.00×10^{-4} M and [Ligand] = 0.005 – 0.05 M.

Such observations can be attributed to the favourable charge-charge interactions between the Br^- ion and the corresponding cationic complex **LM1**. Furthermore, the increased basicity of the entering ligand DMAP (pKa = 9.80[11]) than pyridine (pKa = 5.23[11]), suggests an increased ligand interaction with the Re(I) metal centre.[2]

In theory, the high negative entropy values obtained are associated with an associative (*A*) mechanism[8,9] and in this case -34.1(10) $JK^{-1}mol^{-1}$ and -79.1(9) $JK^{-1}mol^{-1}$ were obtained for the Py and DMAP reactions, respectively. However, more information using high pressure kinetic studies which investigate the activation volume, $\Delta V^{\ddagger}$, needs to be undertaken to achieve this.[12] The variations in k_{-1} and k_1 suggest that the reactions are dependent on the nucleophilicity of the entering ligand.

In general, it seems as if the kinetically obtained values for stability constants, K_1, for Py as entering ligand are slightly higher than that of DMAP. Due to the small absorbance changes observed under our reaction conditions, it was not possible to gather reliable data to determine K_1 also thermodynamically for comparison with the tabled values.

Having investigated the effect of the monomeric *N,N*-bidentate ligand around the *fac*-$[Re(CO)_3MeOH]^+$ core, the degree of the methanol labilising effect conferred by dendritic structures around the *fac*-$[Re(CO)_3MeOH]^+$ core was also of interest.

4.3.5. Substitution reactions of dendritic complexes C23 and C24 with monodentate ligands (Pyridine, DMAP and Br^-)

Preliminary stability and kinetic studies of *fac*-$[Re_4(N,N'\text{-G1picolyl})(CO)_{12}(OH_2)_4]^{4+}$ (**LM4**) and *fac*-$[Re_8(N,N'\text{-G2picolyl})(CO)_{24}(OH_2)_8]^{8+}$ (**LM8**) with Py, DMAP and Br^- ligands were performed in dry methanol. All the reactions were found to be too fast for conventional UV/vis spectroscopic studies and could only be followed on a stopped-flow apparatus. Under *pseudo*-first order conditions, only one reaction was observed for all the reactions studied and the rates of these reactions were increased systematically with the increase in ligand concentration.

In order to describe the general mechanism for the reaction of a dendrimer with monodentate entering ligands, the following simplified approach, **Scheme 4.2**, will first be followed in which the situation of a dendrimer containing two metal centres is used.

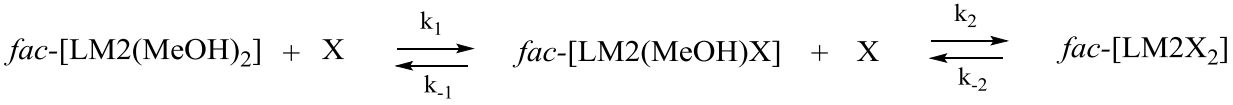

Scheme 4.2: Proposed MeOH substitution overall equilibrium for a complex with two *facial* metal cores.

The rate of the reaction is given below.

$$\text{Rate} = k_1\, fac\text{-}[LM2(MeOH)_2] + k_2\, fac\text{-}[LM_2(X)(MeOH)] - k_{-1}\, fac\text{-}[LM2(X)(MeOH)] - k_{-2}\, fac\text{-}[LM2X_2] \quad \textbf{Equation 4.4}$$

Where k_1, and k_2 represent the forward reactions and k_{-1} and k_{-2} the reverse. By employing the *pseudo* first-order conditions with [X] >>> [total metal concentration], **Equation 4.4** is reduced to **Equation 4.5**:

$$k_{obs} = (k_1 + k_2)[X] + (k_{-1} + k_{-2}) \quad \textbf{Equation 4.5}$$

From this, it means the overall rate second order constant, $k_{1'} = (k_1 + k_2)$, can be obtained from plots of k_{obs} *vs* [X].

Similarly, for a dendritic complex containing *n* number of metal centres, the overall second order rate constant can be obtained as:

$$k_n' = (k_1 + k_2 + \ldots + k_n) \quad \textbf{Equation 4.6}$$

In the current study, all rates and concentration dependencies correspond to the methanol substituted complexes **LM4** and **LM8** (**Figure 4.9**). The dendritic analogues 1.00×10^{-4} M **LM4** and 1.00×10^{-5} M **LM8**, and their substitution kinetic behaviour was investigated to determine the equilibrium constants and rate constants of the substitution of the

aqua/methanol ligand at the sixth coordination site by DMAP, pyridine and Br^- at 25.0 °C. All experiments were performed in dry methanol with the entering ligands having concentrations ranging from 0.005 – 0.05 M.

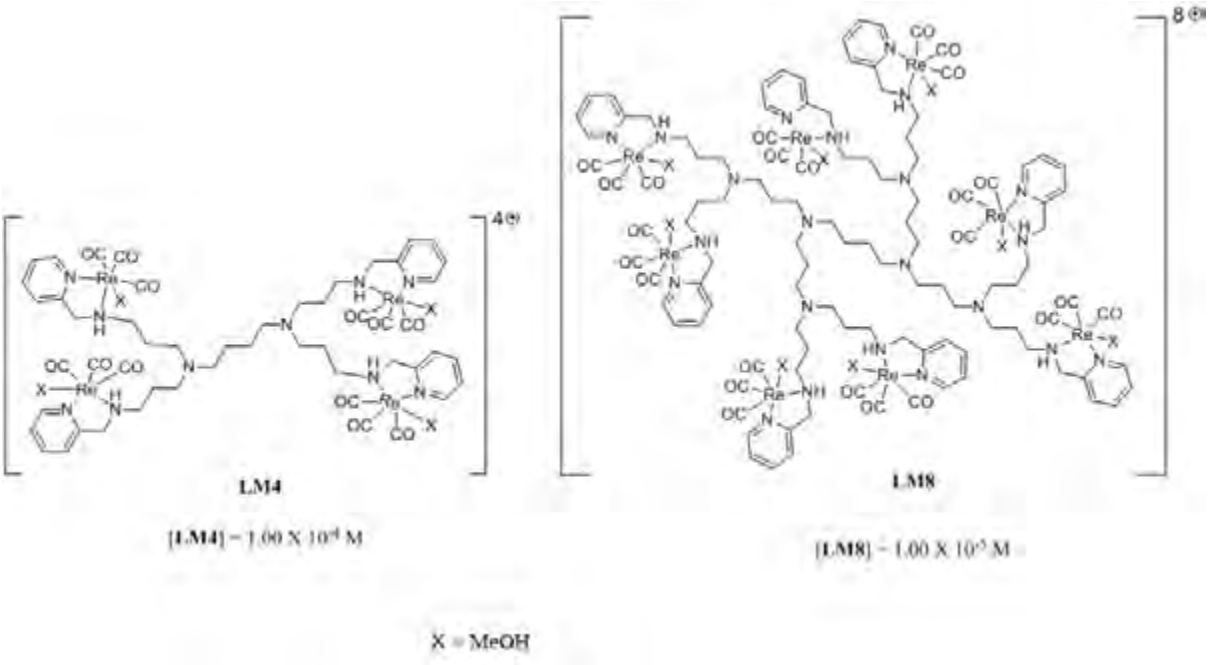

Figure 4.9: Schematic representation of methanol substituted complexes, **LM4** and **LM8**, studied in methanol substitution kinetics.

A UV/vis spectrum of the reaction between **LM4** and Br^- is shown in **Figure 4.10**. In the UV/vis spectra of **LM8**, a similar trend is observed.

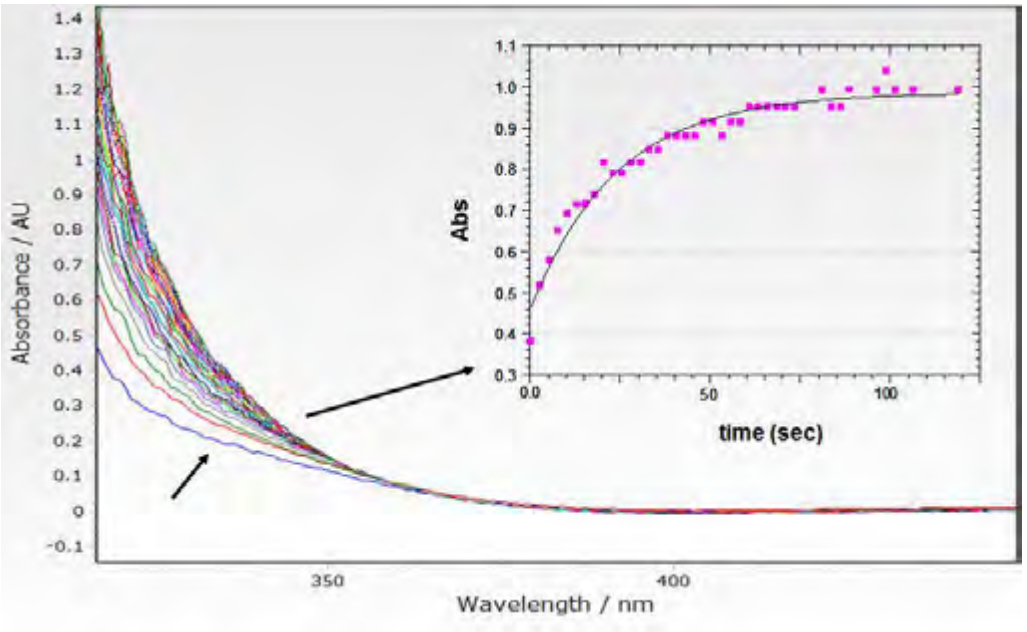

Figure 4.10: Typical UV/vis spectral change for the reaction between *fac*-[Re_4(*N,N*-G_1picolyl)$(CO)_3(MeOH)]^{4+}$ (**LM4**) and Br^- at 25.0 ºC. [**LM4**] = 1.00×10^{-4} M, [Br^-] = 0.025 M, λ = 317 nm.

The insert in **Figure 4.10** represents the absorbance change *versus* time at 317 nm, confirming the first order behaviour.

4.3.5.1. ***LM4*** *and* ***LM8*** *+ Pyridine at 25.0 ˚C.*

The evaluation of the substitution kinetics of methanol by pyridine for [Re_4(*N,N'*-G_1picolyl)$(CO)_{12}(MeOH)_4]^{4+}$ (**LM4**) and [Re_8(*N,N'*-G_2picolyl)$(CO)_{24}(MeOH)_8]^{8+}$ (**LM8**) supported by the plots of k_{obs} vs [Pyridine] in **Figure 4.11**.

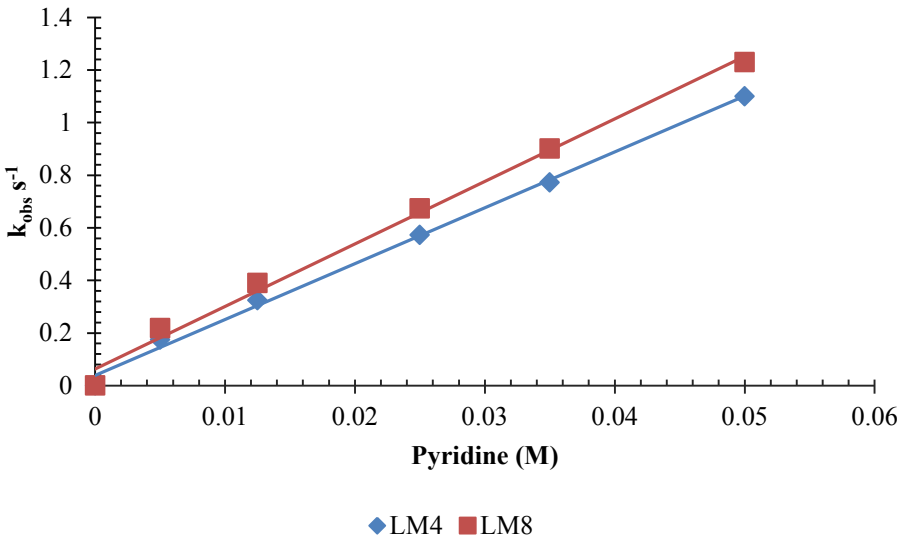

Figure 4.11: The plots of k_{obs} *versus* [Pyridine] for the reactions between 1.00×10^{-4} M *fac*-$[Re_4(N,N'\text{-}G_1\text{picolyl})(CO)_{12}(MeOH)_4]^{4+}$ (**LM4**) and 1.00×10^{-5} M *fac*-$[Re_8(N,N'\text{-}G_2\text{picolyl})(CO)_{24}(MeOH)_8]^{8+}$ (**LM8**). [Pyridine] = 0.005 – 0.05 M, λ = 317 nm.

The linear relationship of k_{obs} *vs* [Pyridine] suggests these reactions occur *via* a similar substitution mechanism as the monomeric analogue **LM1**, as illustrated by **Equation 4.5**. The kinetic data of the reactions represented in **Figure 4.11** is summarized in **Table 4.4**.

Table 4.4: Rate constants for the reactions between **LM4** and **LM8** with pyridine

Pyridine	**LM4 (n = 4)**	**LM8 (n = 8)**
$\mathbf{k_n}$ **($M^{-1}s^{-1}$)**	19.9(8)	22.7(4)
$\mathbf{k_{-n}}$ **(s^{-1})**	0.0749(2)	0.105(5)
$\mathbf{K_n}$ **(M^{-1})**	265(9)	216(4)

*4.3.5.2. **LM4** and **LM8** + 4-Dimethylaminopyridine at 25.0 ˚C*

The methanol substitution kinetics between DMAP and complexes **LM4** and **LM8** were performed using a stopped-flow spectrophotometer. The reactions were monitored at 312nm. The Re(I) metal concentrations were kept constant at 5.00×10^{-4} M **LM4** and 1.00×10^{-5} M **LM8**, whereas, the incoming ligand DMAP concentration was varied from 0.005 – 0.05 M. A plots of k_{obs} *versus* [DMAP] for the aforementioned reactions at 25.0 °C are reported in **Figure 4.12**.

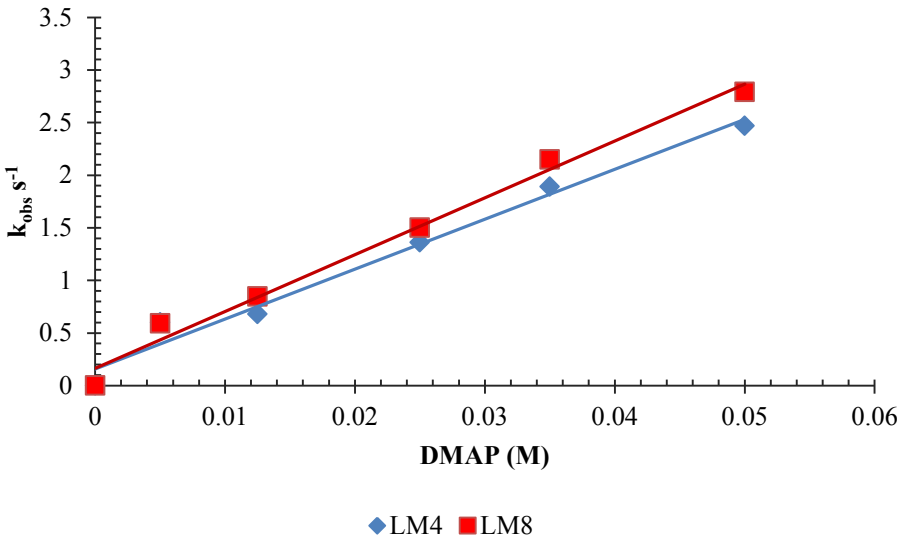

Figure 4.12: The plots of k_{obs} *versus* [DMAP] for the reactions between 1.00 X 10^{-4} M *fac*-[Re_4(*N,N'*-G_1picolyl)$(CO)_{12}(MeOH)_4]^{4+}$ (**LM4**) and 1.00 X 10^{-5} M *fac*-[Re_8(*N,N'*-G_2picolyl)$(CO)_{24}(MeOH)_8]^{8+}$ (**LM8**). [DMAP] = 0.005 – 0.05 M, λ = 312 nm.

The rate data are listed in **Table 4.5**.

Table 4.5: Rate constants for the reactions between **LM4** and **LM8** with DMAP at 25.0 °C

DMAP	LM4 (n = 4)	LM8 (n = 8)
k_n ($M^{-1}s^{-1}$)	46.0(2)	50.7(6)
k_{-n} (s^{-1})	0.205(2)	0.255(3)
K_n (M^{-1})	224(5)	199(1)

*4.3.5.3. **LM4** and **LM8** + Bromo- ion (Br^-) at 25.0 ˚C.*

The Br^- ligand was chosen to understand the influence of the anionic charge on cationic dendritic ligands. The bromide ions were obtained from Et_4NBr. In **Figure 4.13**, the plots of k_{obs} *vs* [Br^-] at 25.0 ˚C are displayed. These values afforded the kinetic data summarised in **Table 4.6**.

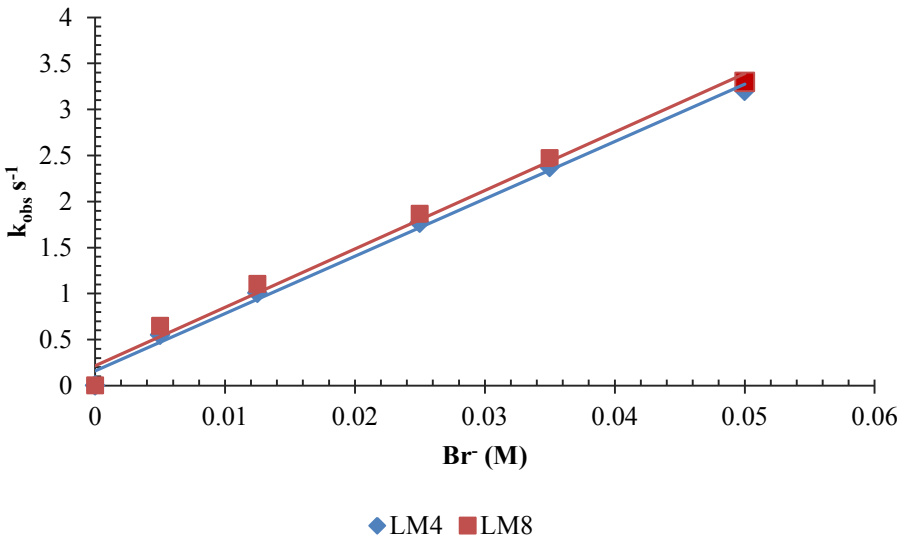

Figure 4.13: The plot of k_{obs} *vs* [Ligand] (Ligand = Br^-) obtained using *fac*-[Re_4(*N,N'*-G_1picolyl)$(CO)_{12}(MeOH)_4]^{4+}$ (**LM4**) = 1.00×10^{-4} M and *fac*-[Re_8(*N,N'*-G_2picolyl)$(CO)_{24}(MeOH)_8]^{8+}$ (**LM8**) = 1.00×10^{-5} M [Br^-] = 0.005 – 0.05 M and T = 25.0 ˚C.

The second generation dendritic complex has an increased k_{obs} value compared to the other complexes and the linear plots is a good indication that the correct mechanism is assigned (**Equation 4.6**).

Table 4.5: Rate data for the reaction between **LM4** and **LM8** with Br^- at 25.0 ˚C

Br^-	**LM4 (n = 4)**	**LM8 (n = 8)**
k_n ($M^{-1}s^{-1}$)	60.8(2)	60.7(2)
k_{-n} (s^{-1})	0.274(4)	0.346(7)
K_n (M^{-1})	222(3)	175(6)

The increase in the polydispersity of a complex results in a faster reaction rate, however, the k_1 values for **LM4** and **LM8** are comparable. This may be attributed to the increased inductive effect, by virtue of the dendritic arms, which influences the electron density around the Re(I) metal centre through the π-back bonding effect.

4.4. Discussion and conclusions

Table 4.6 summarizes the rate data for the reactions of **LM1**, **LM4** and **LM8** with various nucleophilic ligands at 25.0 ºC.

Table 4.6: Rate data for the reactions between **LM1**, **LM4** and **LM8** with various entering monodentate nucleophiles at 25.0 ˚C.

LM1 (n = 1)	**k_n ($M^{-1}s^{-1}$)**	**k_{-n} (s^{-1})**	**K_n (M^{-1})**
Py	10.2(1)	0.062(4)	164(7)
DMAP	28.7(1)	0.301(3)	95.3(6)
Br^-	34.8(4)	0.165(1)	211(2)
LM4 (n = 4)	**k_n ($M^{-1}s^{-1}$)**	**k_{-n} (s^{-1})**	**K_n (M^{-1})**
Py	19.9(8)	0.0749(2)	265(9)
DMAP	46.0(2)	0.205(2)	224(5)
Br^-	60.8(2)	0.274(4)	222(3)
LM8 (n = 8)	**k_n ($M^{-1}s^{-1}$)**	**k_{-n} (s^{-1})**	**K_n (M^{-1})**
Py	22.7(4)	0.105(5)	216(4)
DMAP	50.7(6)	0.255(3)	199(1)
Br^-	60.7(2)	0.346(7)	175(6)

Based on the second order rate constants (k_n) in **Table 4.6**, the **LM1** reactions are slower than **LM4** and **LM8** reactions by a factor of ~2, hence, as the number of metal centres increase the reaction rate increases. Twala and co-workers investigated the formation of monomeric *fac*-$[Re(CO)_3(N,N\text{-bidentante})Py]^+$ type complexes at 25.0 ºC and obtained rate constants of $2.93(9) \times 10^{-3}$ and $2.39(5) \times 10^{-3}$ $M^{-1}s^{-1}$ (typical metal concentration 4.00×10^{-4} M – 1.00×10^{-4} M).[5] These rate constants are significantly lower (the reactions are ~6000 – 8000 times slower) than those obtained in the current study for the substitution of MeOH by Py in dendritic complexes **LM4** (19.9(8) $M^{-1}s^{-1}$) and **LM8** (22.7(4) $M^{-1}s^{-1}$). The increase in the rate accentuates the strong labilising effect of the dendritic *N,N*-bidentate ligands than the monomeric *N,N*-bidentate ligands. Therefore, the dendritic architecture on *N,N*-picolylamino moieties in complexes **LM4** and **LM8**, has labilising effect on the generally inert Re(I)-tricarbonyl core.

The second order rate constants (k_1) for **LM4** and **LM8** with Br^- as the entering ligand (~60.0 $M^{-1}s^{-1}$, **Table 4.6** and **Figure 4.14**) are comparable and the pre-equilibrium constants (K_1) are almost similar (**LM4** = 222(3) M^{-1} and **LM8** = 175(6) M^{-1}).

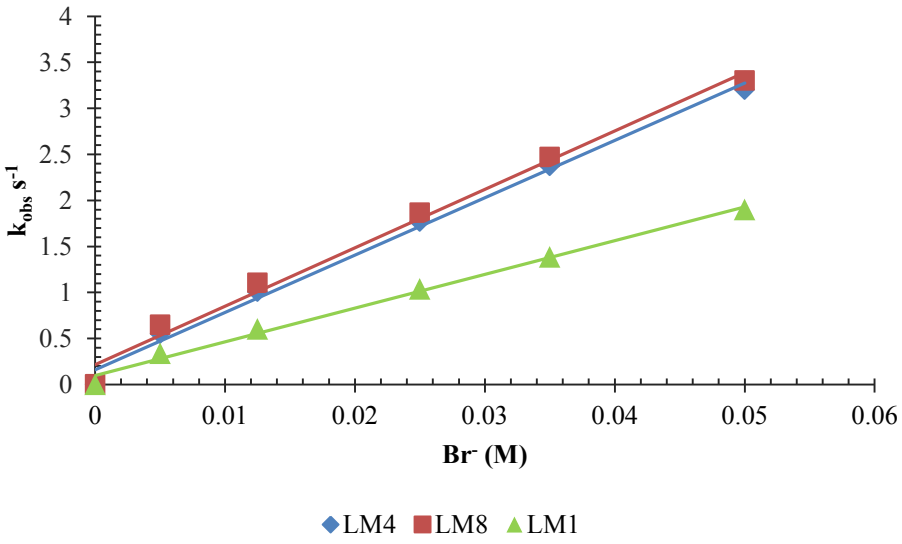

Figure 4.14: Overlap plot of k_{obs} *vs* [Br^-] for the reactions between **LM1**, **LM4** and **LM8** with Br^- ion at 25.0 ºC.

Therefore, it can be postulated that the k_1 values for **LM4** account for all four steps involved when the MeOH ligand is substituted by the monodentate nucleophiles. This demonstrates the ability of the dendritic arms to 'communicate' with each other. As the metal concentration increases, the rate increases by a factor of 2 (**LM1** to the dendritic complexes), however a limit is reached thereafter (supported by comparable rate constants of **LM4** and **LM8**) and this phenomenon will have to be investigated further.

At 25.0 ˚C, the k_1 value corresponding to **LM1** brominated complex (**Table 4.6**) is 34.8(4) $M^{-1}s^{-1}$ comparable to 28.7(1) $M^{-1}s^{-1}$ in the presence of DMAP. However, the stability constant, K_1, in the presence of Br^- ions increases to 211(2) M^{-1} compared to 95.3(6) M^{-1} in DMAP. The great increase in K_1, compared to the constants shown in **Table 4.1 – 4.2** at varying temperatures, is attributed to the favourable charge-charge interactions between the

Br^- ion and corresponding cationic complexes. This suggest an associative mode of activation to form neutral complexes as the Br^- ions have a greater affinity for the electrophilic Re(I)tricabornyl core.

The flexibility of the dendritic arms permit faster reaction rates as the second order equilibrium constants increase with the dendrititc generations. When there is greater deviation on the k_{-1} values than the k_1 values, there is less dependence on the entering ligand suggesting a dissociative type reaction mechanism.[14,15] In the current study, the IR data corresponding to **LM4** in DMAP (**C23** + DMAP[a] in **Chapter 3**) cannot distinguish between single steps of substitution, therefore, it is proposed that the measured substitution rate of MeOH by 4 equivalents of DMAP is the overall rate of the reaction.

4.5. Summary

The preliminary kinetic studies of the monomeric and dendritic complexes 5.00×10^{-4} M *fac*-[Re*N*-((pyridine-2-yl)methyl)propan-1-amine)$(CO)_3$(MeOH)]$^+$ (**LM1**), 1.00×10^{-4} M *fac*-[Re_4(*N,N'*-G_1picolyl) $(CO)_{12}(MeOH)_4]^{4+}$ (**LM4**) and 1.00×10^{-5} M *fac*-[Re_8(*N,N'*-G_2picolyl)$(CO)_{24}(MeOH)_8]^{8+}$ (**LM8**) with varying ligands (Br^- ions, Py and DMAP) were investigated. By comparing the rate constants at 25.0 °C, the following can be deduced:

- The second order rate constants for the reactions with Br^- ions are greater than those of *N*- donor ligands (**Table 4.6**).
- The second order rate constants for the reactions **LM1**, **LM4** and **LM8** with DMAP (**Table 4.6**) are ~2 times higher than in the case where pyridine is used (**Table 4.6**).
- The increase in rate constants from **LM1** to **LM4/8** indicates that the DAB-PPI dendrimer architecture does influence the rate of substitution reactions, but this effect is less

dramatic as the generation increases from **LM4** to **LM8** (the reason for this is unknown but more studies are necessary to investigate this)

- The stability constants K_1 of the reactions at 25.0 ºC do not show a definite trend moving from a charged ligand to a neutral ligand. However, the dendritic complexes are notably stable in the presence of N-donating ligands.
- Since the activation parameters for the complexes **LM4** and **LM8** with the ligands at varying temperatures were not investigated, high pressure studies are required in order to investigate the mode of activation of these complexes as it becomes more obvious whether the rate increases or decreases as the pressure in varied *i.e.* whether the activation volume $\Delta V^{\ddagger}$ is positive or negative.[16]
- The activation entropy values for **LM1** reacted with pyridine and DMAP are negative but are not as high enough to infer pure associative mechanism.[3] Entropy decreases as the entering ligand and complex come together in the rate-determining step (indicative of less disorder in the transition state). In a *D* process, the loss of the leaving ligand in the rate-determining step increases entropy, resulting in positive entropy of activation. Experimental errors are inherent in the long extrapolation needed to estimate $\Delta S^{\ddagger}$ values from plots.[16]
- Previous substitution kinetic studies involving the *fac*-$[Re(CO)_3(H_2O)_3]^+$ complex—in other instances the two aqua ligands substituted by *O,O'*- , *N,O* – and *N,N'*- bidentate ligands—in the presence of Br^- ions, pyridine or DMAP suggested a dissociative interchange mechanism.[2,3,8,14,17]
- The IR data of the complexes attests that the kinetic reactions observed corresponded to the MeOH substitution and not the dissociation of the bidentate ligand.

4.6. References

1. S. Mundwiler, S, M. Kundig, K. Ortner, R. Alberto, *Dalton Trans.,* 2004, 1320 − 1328.
2. M. Schutte, G. Kemp, H. G. Visser, A. Roodt, *Inorg. Chem.*, 2011, **50**, 12486 – 12498.
3. A. Brink, H. G. Visser, A. Rood,. *Inorg. Chem*., 2013, **52**, 8950 − 8961.
4. M. Schutte, A. Roodt, H. G. Visser, *Inorg. Chem.*, 2012, **51**, 11996 – 12006.
5. T. N. Twala, N. Schutte-Smith, A. Roodt, H. G. Visser, *Dalton Trans.*, 2015, **44**, 3278 – 3288.
6. P. V. Grundler, B. Salignac, S. Cayemittes, R. Alberto, A. E. Merbach, *Inorg. Chem*., 2004, **43**, 865 − 873.
7. A. Brink, H. G. Visser, A. Roodt, *J. Coord. Chem.*, 2011, **64**, 122 – 133.
8. Benson, *Mechanism of Inorganic Reactions in Solution*, McGrawHill, London, 1968.
9. R. G. Wilkins, *Kinetics and Mechanism of Reactions of Transition Metal Complexes*, 2nd ed.; VCH Publishers, Inc.: New York, 2002.
10. M. Schutte, PhD Thesis, University of the Free State, 2011.
11. D. D. Perrin, *Dissociation Constants of Organic Bases in Aqueous Solution*; Butterworths: London, 1965; Supplement, 1972.
12. P. V. Grundler, B. Salignac, S. Cayemittes, R. Alberto, A. E. Merbach, *Inorg. Chem.,* 2004, **43**, 865 − 873.
13. S. Mundwiler, R. Waibel, B. Springler, S. Kunze, R. Alberto, *Nucl. Med. Bio.*, 2005, **32**, 473 – 484.
14. D. D. Perrin, *Dissociation Costants of Organic Bases in Aqueous Solution,* Butterworths, London, 1965, Supplement, 1972.
15. M. Schutte, PhD Thesis, University of the Free State, 2011.

16. B. Salignac, P. V. Grundler, S. Cayemittes, U. Frey, R. Scopelliti, A. E. Merbach, *Inorg. Chem*., 2003, **42**, 3516 − 3526.

17. T. W. Swaddle, *Adv. Inorg. Bioinorg. Mech.,* 1983, **2**, 95 – 138.

Chapter 5

Technetium-99m and gallium-68 radiolabeling studies

5.1. General introduction

Dendrimers are known to encapsulate multitude species such as metal ions[1-5], anions[6,7] and solvent molecules (neutral substrates[8,9]). Stephen and co-workers investigated the extraction of sodium pertechnetate ($Na^{99m}TcO_4$), a common nuclear waste contaminant[10], by benzo-crown-modified poly(propylene amine) (POMAM) dendrimers of varying generations (**Figure 5.1**) in chloroform.[3]

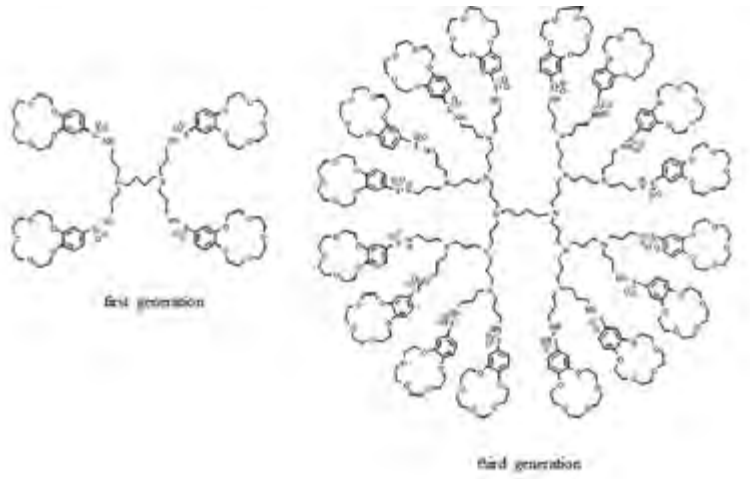

Figure 5.1: Constitution of the benzo-crown-modified poly(propyleneamine) dendrimers of different generations.[3]

The metal-binding affinity results demonstrated an increased $[^{99m}TcO_4]^-$ binding efficiency with increasing dendrimer generation.[3] Also, during liquid-liquid extraction processes the analysis of the organic phase under basic conditions revealed low binding affinity of $[^{99m}TcO_4]^-$,[3] reflecting a pH dependent factor of dendrimer-based radiochemical interactions.

Technetium-99m (**Chapter 1**, *Section 1.4.2.*) is a gamma (γ)-emitting radionuclide commonly used in imaging medical conditions using Single Photon Emission Computed Tomography (SPECT) scan, a nuclear imaging methodology that allows real-time monitoring of organ function *in vivo*, diagnose medical conditions and follow up disease progression.[11,12] The 6 hour half-life of ^{99m}Tc is favourable for monitoring the disease hours post injection with a radiopharmaceutical. Gallium-68 (^{68}Ga, β+, 88.9%, half-life = 68 minutes) emits two divergent gamma-photons per decay allowing for the construction of three dimensional (3D)–diagnostic images through a Positron Emission Tomography (PET) scan.[12,13] The 68 minutes half-life is favourable for radiolabeling, and for the biodistribution of small molecules and biomolecules such as peptides.[12] The PET scans are more sensitive but expensive than SPECT scans.

The unique topology of dendrimers permits various possibilities of metal-binding behaviour within the dendritic framework or functionalized periphery.[3] In nuclear imaging, the radiolabeling of higher generation dendrimer ligands with radiotracers such as ^{99m}Tc and ^{68}Ga for disease diagnosis is of current interest. The multivalent nature, 'enhanced and permeability retention' effect[14] and favourable generation-dependent biodistribution profiles of dendrimers in diseased tissues[15-17], may enhance the sensitivity of imaging modalities through multitude attachment of diagnostic radioisotopes per dendrimer (lowering the injection dose to a patient) leading to enhanced image quality and resolution.

In the current study, the ^{99m}Tc and ^{68}Ga radiolabeling of first generation diaminobutane poly(propylene amine) (DAB-PPI) dendrimers grafted with 2-picolylamino (**Figure 5.2**) moieties at the periphery is reported.

5.2. Preliminary studies: radiolabeling of L5 using ^{99m}Tc

Labeling of the first generation 2-picolylamino functionalized DAB-PPI dendrimer with ^{99m}Tc radiotracer was performed using direct labeling ($[^{99m}TcO_4]^-$), and 'kit' methods (*fac*-$[^{99m}Tc(CO)_3(H_2O)_3]^+$ obtained from the isoLink® kit). The first generation dendritic ligand **L5** (**Figure 5.2**) was purposely selected for direct labeling studies as a result of its water solubility.

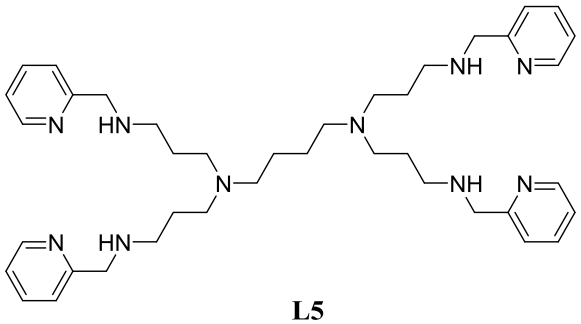

L5

Figure 5.2: Proposed structure of **L5**.

5.2.1. Direct radiolabeling studies using $[^{99m}TcO_4]^-$

The feasibility of labeling ligand **L5** (**Figure 5.2**) was investigated using modified literature methods.[18-21] In preparation of the labeling formulation, a generator eluted solution of $Na^{99m}TcO_4$ (22.2 mCi) was reduced with a 0.1 M solution of stannous chloride ($SnCl_2$) in the presence of **L5**. Different dendritic formulations at pH 4.5, 5.5, 6.0 and 7.0 were investigated. The labeling pH was adjusted using a buffer solution ($NaHPO_4$/citric acid). Other experimental parameters such as the amount of $SnCl_2$ (reduces the inert +7 oxidation state of ^{99m}Tc in $[^{99m}TcO_4]^-$ to reactive oxidation states < +7), incubation temperature (80.0 ˚C) and radiochemical reaction time (15 minutes) were kept constant.

The labeling efficiency of the radioactive dendritic formulations were measured through a gamma detector using instant thin-layer chromatograpy silica gel (iTLC-SG) and Whatmann cellulose fibre sheets passed through saline and acetone, respectively (**Figure 5.3**).

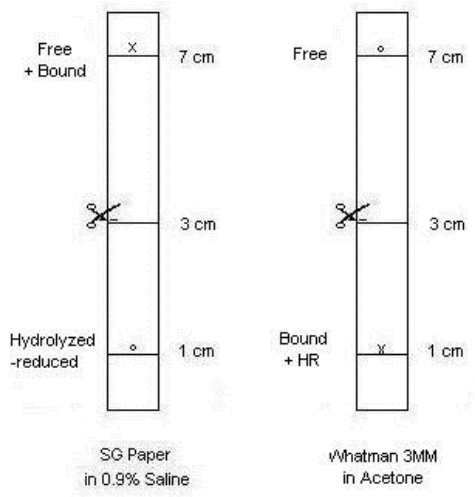

$$F\ (\%) = \frac{F \times 100}{H+B+F}$$

$$H\ (\%) = \frac{H \times 100}{H+B+F}$$

$$B\ (\%) = 100 - F\ (\%) - H\ (\%)$$

Figure 5.3: A chromatographic system for analysing radiochemical purity of ^{99m}Tc-radiopharmaceuticals.[22-24] When the mobile phase reaches the solvent front line, the chromatogram is cut into two equivalent halves. Thereafter, each segment is placed in a gamma detector to measure the radioactivity.

The available literature reports suggest that the amount of $SnCl_2$ as a reducing agent influences the labeling efficiency and the formation of ^{99m}Tc colloids.[18,19] The iTLC-SG gives an estimate of bound and hydrolized ^{99m}Tc at the origin and free ^{99m}Tc at the solvent front.[22,23] Copious amounts of $SnCl_2$ influence the formation of adverse radiocolloids as a result of free, reduced or hydrolysed $[^{99m}TcO_4]^-$.[18] Moreover, inadequate amounts of $SnCl_2$ result in poor labeling efficiency as a result of incomplete reduction of $[^{99m}TcO_4]^-$ from its inert heptavalent oxidation state.[18,19]

In **Figure 5.3**, on the iTLC-SG paper base line the radiocolloids (hydrolized/reduced) are retained, whereas, the labeled complex (bound) together with 'free' $[^{99m}TcO_4]^-$ migrate towards the solvent front.[18] In order to obtain the amount of labeled complex (*bound*), the activity migrating with acetone towards the solvent front corresponds to the 'free' $[^{99m}TcO_4]^-$

and is subtracted from the activity corresponding to the labeled formulation comprising **L5** and $[^{99m}TcO_4]^-$ (**Figure 5.3**, *free* + *bound*) on iTLC-SG paper.[18] The obtained activity amounts (in mCi units) are substituted in the equations revealed in **Figure 5.3** to obtain the F ('free' ^{99m}Tc), H (hydrolysed or reduced ^{99m}Tc/ colloids) and B (**L5** bound ^{99m}Tc) variables.[18,19,22] The retention factor (R_f) values were not measured. The properties of **L5** labeled at pH 4.5 – 7.0 using the direct method are summarized in **Table 5.1**.

Table 5.1: Effect of pH on labeling efficiency of **L5** at *T = 80.0 ˚C* and *time = 15 min.*

Labeling pH	% Label (^{99m}Tc-**L5**) B	% Radiocolloids ($^{99m}TcO_2$) H	Free % ^{99m}Tc F
4.5	60	40	0
5.5	72.1	27.9	0
6.5	21	79	0
7.0	21	74	5

From **Table 5.1**, at labeling pH 4.5 the labeling yield is 60% and the 40% difference is attributed to the radiocolloids. At pH 6.5 and 7.0, the labeling efficiency decreases to 21% attesting that the pH needs to be critically controlled in radiolabeling of **L5**. At pH 7, colloidal ^{99m}Tc precipitated in the reaction mixture. The highest labeling efficiency of 72.1% is obtained at pH 5.5.

In the work done by Stephen and co-workers, the liquid-liquid extraction studies of $[^{99m}TcO_4]^-$ by third generation crown ether PPI dendrimer (**Figure 5.1**) revealed a highest metal-binding efficiency of 54.1% at pH 5.4, independent of the buffer composition.[3] This group reasoned that the decrease in $[^{99m}TcO_4]^-$ binding affinity to the dendrimers at higher pH occurs as a result of low protonation state of the interior tertiary amine groups within the polyamine framework[25], which render the coordination to $[^{99m}TcO_4]^-$ *via* electrostatic interactions possible.[3] Based on their experimental findings, Stephen *et al*. reported the crown

ether functionalities to have lower binding affinity to Na^+ and $[^{99m}TcO_4]^-$.[3] Thus, in the present study it is possible that at pH 5.5, all the nitrogen atoms in **L5** including the periphery moieties get protonated with the possibility to coordinate anionic ^{99m}Tc species.

The radio-HPLC analysis gamma ray (Gina star, Raytest Gabi) of the aliquot at pH 5.5 afforded the chromatogram in **Figure 5.4** with a peak having retention time ranging from 1.92 – 2.01 minutes (mobile phase: acetonitrile(ACN)/H_2O – 55/45%, stationary phase: Phenomenex Luna C18 100 Å (4 × 250 mm × 5 µm), flow rate: 0.5 mL/min). Such results are inconclusive as 'free' $[^{99m}TcO_4]^-$ was found to elute around 2.00 minutes, possibly co-eluting with the ^{99m}Tc+**L5** complex formulation. Although the formulation at pH 5.5 was not used for further studies, the current study elucidates the feasibility of labeling **L5** with ^{99m}Tc.

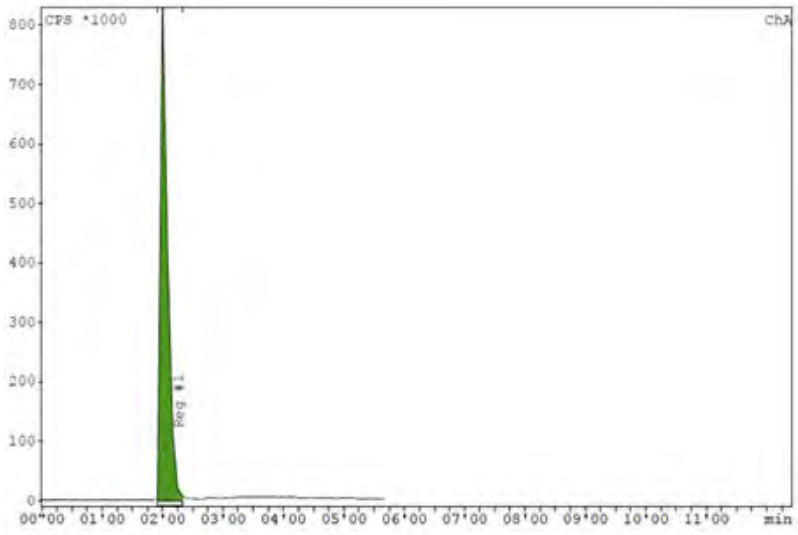

Figure 5.4: radio-HPLC chromatogram of **L5** in pertechnetate $[^{99m}TcO_4]^-$ using a Luna C18 column. **Mobile phase**: acetonitrile(ACN)/H_2O – 55/45%, **stationary phase**: Phenomenex Luna C18 100 Å (4 × 250 mm × 5 µm) column and **flow rate**: 0.5 mL/min

It is important that a radiopharmaceutical has a radiolabeling efficiency of 95% and above.[22,23] Also, the ideal pH of a radiopharmaceutical is 7.4, which corresponds to the blood pH. However, due to the buffer capacity of the blood, the ideal pH can vary between 2 and 9.[23]

5.2.2. Radiosynthesis studies using the *fac*-[^{99m}Tc(CO)$_3$(OH$_2$)$_3$]$^+$

5.2.2.1. isoLink® kit activation

The combination of boranocarbonate (carbonylation reagent), disodium tartrate dehydrate and borax decahydrate under elevated temperatures reduces the heptavalent oxidation state of [^{99m}TcO$_4$]$^-$ to a univalent oxidation state leading to the synthesis of *fac*-[^{99m}Tc(CO)$_3$(OH$_2$)$_3$]$^+$ complex (isoLink® kit).[26] The lyophilized isoLink® kit was activated as described in the literature[27-29] and kit protocol (Centre of Radiopharmaceutical Research at the Paul Scherrer Institute in Switzerland). The kit activation was monitored using ultrahigh-performance liquid chromatography (UHPLC) Ultimate 3000 Thermofisher Dionex equipped with a UV spectrophotometer and a Berthold LB509 radiodetector. The chromatogram is displayed in **Figure 5.5**. The retention time of *fac*-[^{99m}Tc(CO)$_3$(OH$_2$)$_3$]$^+$ was found to be 2.02 ± 0.2 minutes, possibly co-eluting with minute traces of [^{99m}TcO$_4$]$^-$.

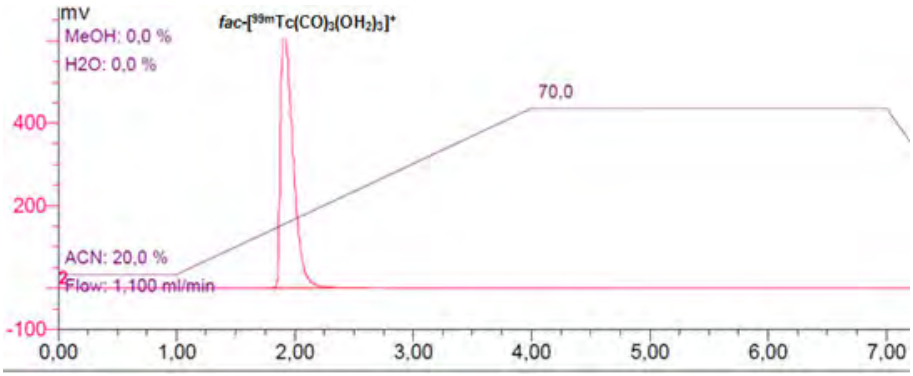

Figure 5.5: Radiometric analysis (UHPLC-Gamma detector) of the active isoLink® kit has a retention time of 2.13 minutes corresponding to *fac*-[^{99m}Tc(CO)$_3$(OH$_2$)$_3$]$^+$ co-eluting with [^{99m}TcO$_4$]$^-$. **Stationary phase**: Phenomenex Luna C18 column (4.6 × 250 mm × 5 µm). **Gradient mobile phase**: acetonitrile (ACN)/water (20/80 – 70/30%). **Flow rate**: 1.1 mL/min

In radiopharmaceutical developmental chemistry of *fac*-[^{99m}Tc(CO)$_3$]$^+$ isomer containing complexes, non-radioactive ('cold') *fac*-[Re(CO)$_3$]$^+$ adducts are used as characterization surrogates on account of corresponding isostructural properties of the two metal cores.[12] In the framework of the current study, the synthesis and characterization of first generation (G1)

DAB-PPI *fac*-[^{99m}Tc(CO)$_3$(*N,N*-G1DAB-PPI)OH$_2$]$^+$ complexes is reported. The 'cold' *fac*-[Re(CO)$_3$OH$_2$]$^+$ DAB-PPI analogues, **C20** and **C23** complexes, have been synthesized and characterized using spectroscopic and analytical techniques as reported in **Chapter 3**. These non-radioactive Re(I) complexes served as models in characterization of the radioactive ^{99m}Tc(I) dendritic complexes by ultra-high performance liquid chromatography (UHPLC Ultimate 3000 Thermofisher Dionex).

*5.2.2.2. Radiolabeling experiment of **L5** using fac-[^{99m}Tc(CO)$_3$(OH$_2$)$_3$]$^+$ and structural elucidation of the radiosynthesis product*

(Poly/di)Picolylamines are commonly reported as stable tridentate chelates orientated in a di(2-picolyl)-amine framework around *fac*-[^{99m}Tc(CO)$_3$]$^+$ isomer, displacing three aqua ligands from *fac*-[^{99m}Tc(CO)$_3$(H$_2$O)$_3$]$^+$.[30-35] The di(2-picolyl)-amine frameworks are known to facilitate facile radiochemical synthesis of ^{99m}Tc complexes. In the current study, the picolylamine type dendritic ligand **L5** was used as a bidentate chelate in the radiochemical synthesis of *fac*-[^{99m}Tc(*N,N*-**L5**)(CO)$_3$OH$_2$]$^+$ (**C23***, * = a radioactive ^{99m}Tc complex) complex. The UHPLC UV/vis (Ultimate 3000 Thermofisher Dionex equipped with a UV spectrophotometer and a Berthold LB509 radiodetector) chromatogram of the free ligand **L5** is shown in **Figure 5.6** and **L5** has a retention time of 3.20 ± 0.2 minutes using a Luna C18 column using acetonitrile/H$_2$O mixture as gradient mobile phase (20/80% – 70/30%).

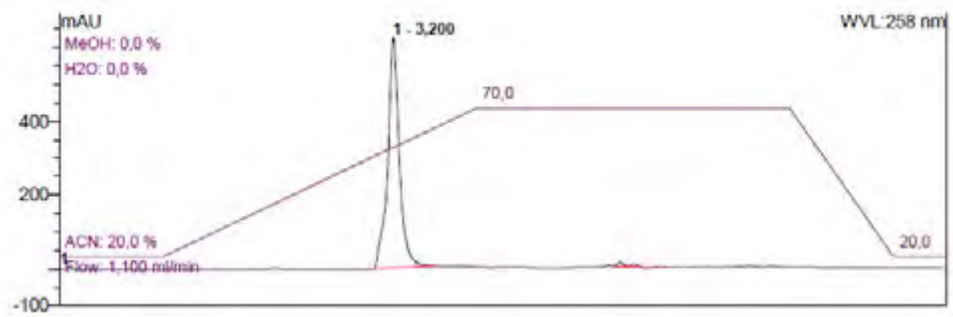

Figure 5. 6: UHPLC UV-vis trace of **L5** (R_t = 3.20 min). **Stationary phase**: Phenomenex Luna C18 (4.6 × 250 mm × 5 µm) column. **Gradient mobile phase**: acetonitrile (ACN)/H$_2$O (20/80% – 70/30%). **Flow rate**: 1.1 mL/min.

The radiosynthesis of the radioactive complex **C23*** was performed using a devised procedure. Briefly, a 100 µL solution of *fac*-[^{99m}Tc(CO)$_3$(H$_2$O)$_3$]$^+$ (654 MBq) precursor was added to 0.21µmol solution of **L5** in H_2O. At pH 6, radioactive mixture was heated to 100 °C for 15 minutes to afford a 210 MBq radiochemical formulation. This experiment was performed in triplicate by varying only the pH to pH 2 and pH 8 in the other two vials using a PBS/HCl buffer. The formulation at pH 6 gave interpretable results. The activity at pH 2 and 8 was 158 and 142 MBq, respectively.

Purification of the **L5**-isoLink® kit formulations through a Sep-Pack C18 Light Cartridge (GE Healthcare) using EtOH/H_2O gradient mobile system resulted in loss of radioactivity and some of the activity was retained in the column (~21.7 MBq at pH 2 and 6; ~ 50.3 MBq at pH 8). The co-elution of the undesired impurities with the product(s) was also observed upon UHPLC analysis and this can be attributed to the enhanced lipophilicity of **L5** or ^{99m}Tc-**L5** labeled complex and the hydrophilic mobile system. The use of the appropriate purification method is important for accurate radiochemical purity, specific activity and labeling reproducibility.[13] Furthermore, radiolabeling of **L5** is pH dependent.

In **Figure 5.7**, the degree of radiochemical synthesis of **C23*** was verified by separately injecting the *fac*-[Re(CO)$_3$(OH$_2$)$_3$]$^+$ medium (the **top** chromatogram in mAU units), the 'cold' Re(I) analogue **C23** (the **middle** chromatogram in mAU units) and the crude **L5**-isoLink® kit formulation at pH 6 (the **bottom** chromatogram in mV units) in a UHPLC equipped with UV-vis and a gamma-ray detector.

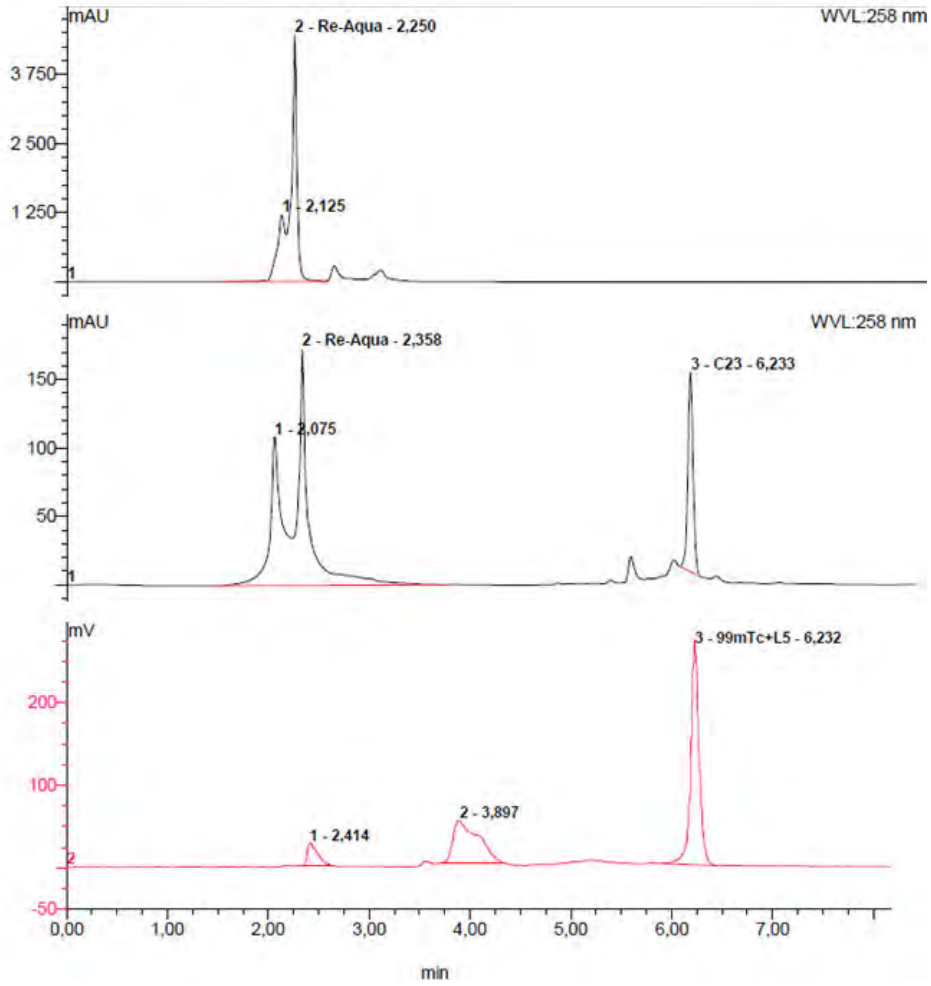

Figure 5.7: Comparative chromatograms of Re(I)-aqua precursor *fac*-$[Re(CO)_3(H_2O)_3]^+$ (**top**), R_t = 2.25 ± 0.2 minutes and λ = 238 nm; the rhenium model complex **C23** (**centre**), R_t = 6.23 ± 0.2 minutes and λ = 258 nm; and the technetium-99m formulation, desired **L5**-isoLink® kit formulation (bottom), at R_t = 6.23 ± 0.2 minutes (λ = 258 nm). **Stationary phase**: Phenomenex Luna C18 (4.6 × 250 mm × 5 µm) column**. Gradient mobile phase**: acetonitrile/H_2O (20/80% – 70/30%). **Flow rate**: 1.1 mL/min.

The chromatogram corresponding to the *fac*-$[Re(CO)_3(H_2O)_3]^+$ complex (**Figure 5.7**, **top** chromatogram) has two peaks at 2.07 ± 0.2 and 2.25 ± 0.2 minutes assigned to Et_4N^+ and *fac*-$[Re(CO)_3(H_2O)_3]^+$, respectively. The chromatogram at the centre, in **Figure 5.7**, corresponds to the crude complex **C23** (**Figure 5.8** and **Chapter 3**).

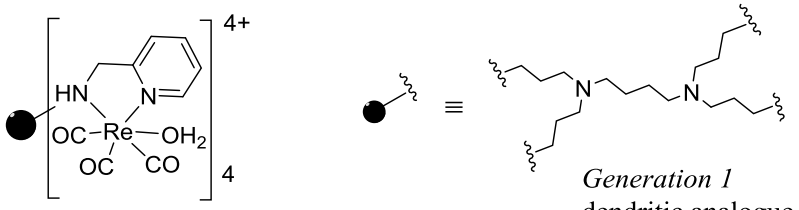

C23

Figure 5.8: Proposed structure of **C23**.

In the second chromatogram (**Figure 5.7**, **middle** chromatogram), a peak with a retention time of 6.23 ± 0.2 minutes is assigned to the complex **C23** (characterization data in **Chapter 3**), where four equivalents of the *fac*-$[Re(CO)_3]^+$ core coordinated at the periphery of the dendritic arms. Other peaks are attributed to the unreacted metal precursor and impurities from the crude mixture injected.

At least, three radioactive species are detected in the radio-UHPLC chromatogram (in mV units) of the **L5**-isoLink® kit formulation (**Figure 5.7**, **bottom** chromatogram). The peak with the retention time of 2.41 ± 0.2 minutes is assigned to the unreacted metal precursor, identified as either *fac*-$[^{99m}Tc(CO)_3(H_2O)_3]^+$ or $^{99m}TcO_4^-$. The possible slow conversion of *fac*-$[^{99m}Tc(CO)_3(OH_2)_3]^+$ *via* oxidation to form $[^{99m}TcO_4]^-$ over the duration of experimentation, is reported in the literature.[36] The gamma detector chromatogram displays a peak at 6.23 ± 0.2 minutes assigned to the target complex **C23*** wherein four equivalents of the *fac*-$[^{99m}Tc(CO)_3]^+$ core are coordinated at the periphery of the dendritic arms *via* the *N,N*-picolylamine donor atoms. The radioactive species between 4.00 – 6.50 minutes, although unexpected, may correspond to ^{99m}Tc-**L5** labeled complexes of different nuclearity, based on the capability of the dendritic periphery (picolyl pendants) and framework (**Chapter 1**, **Figure 1.11**) to compete for the *fac*-$[^{99m}Tc(CO)_3OH_2]$+ precursor.

Based on the comparative chromatographic retention times of the 'cold' Re(I) complex **C23** (6.23 ± 0.2 min) and the radioactive ^{99m}Tc(I) complex **C23*** at 6.23 ± 0.2 minutes (**Figure**

5.7, **bottom** chromatogram in mV units), the translation of Re chemistry to ^{99m}Tc at a radiotracer level using a dendritic *N,N*-picolyamine type ligand was successful. The proposed molecular structure of the radioactive complex at 6.23 ± 0.2 minutes considers the possibility of forming a mixture of bridged dimeric or oligomeric hydroxy complexes *via* the aqua ligand and substitution of the aqua ligand by nucleophilic solvent molecules.

5.3. Preliminary studies: radiolabeling experiment of L2 using *fac*-[^{99m}Tc(CO)$_3$(OH$_2$)$_3$]$^+$ and structural elucidation of the radiosynthesis product

The radiolabeling of the ligand **L2** (**Figure 5.9** and ***Chapter 2***) was performed analogous to the **L5**-isoLink® kit formulation.

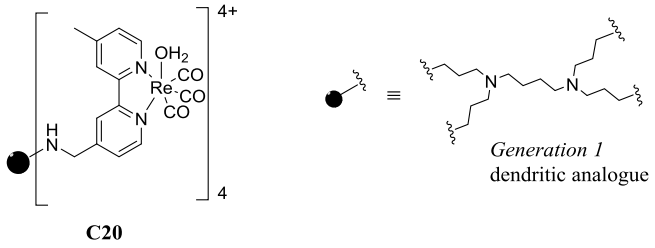

C20

Figure 5.9: Constitution of **C20**

In acetonitrile/H_2O (50/50% – 80/20%) gradient mobile phase system, the 'cold' complex **C20** (**Chapter 3**) has a retention time of 7.15 ± 0.2 min. This retention time does not correlate with that of the radioactive *fac*-[^{99m}Tc(*N,N*-**L2**)(CO)$_3$OH$_2$]$^+$ complex which is 4.01 ± 0.2 minutes. The differences in retention times are not attributed to the sequential configuration of the UV-vis and gamma ray detectors. As in most cases, the deviation in the HPLC retention factors of ^{99m}Tc radiolabeled complexes from Re complexes is due to the dead time as the analyte migrates in the pipe line to the ultraviolet and gamma-ray detectors.[37] These adverse radiosynthesis results may be attributed to the poor solubility of

L2 in labeling aqueous media, reaction time or pH, resulting in inefficient labeling of the dendrimer. Also, the purification of the crude formulation by a Sep-Pack C18 Light Cartridge using EtOH/H_2O gradient mobile system resulted in a drastic loss of radioactivity from the collected fractions. The activity post purification, was found to be retained in the cartridge, possibly radioactive degradation products.

Based on the translatable radiolabeling results on **L5** + technetium-99m preliminary studies, the radiolabeling of **L5** in aqueous media was further attempted using radioactive gallium(III)chloride, [^{68}Ga]$GaCl_3$.

5.4. Preliminary studies: ^{68}Ga radiolabeling experiment of L5

Figure 5.10 displays UHPLC-UV/vis and gamma-detector chromatograms of **L5** (**top** chromatogram), 'free' [^{68}Ga]$GaCl_3$ (**centred** chromatogram), **L5**-[^{68}Ga]$GaCl_3$ purified formulation (bottom chromatogram).

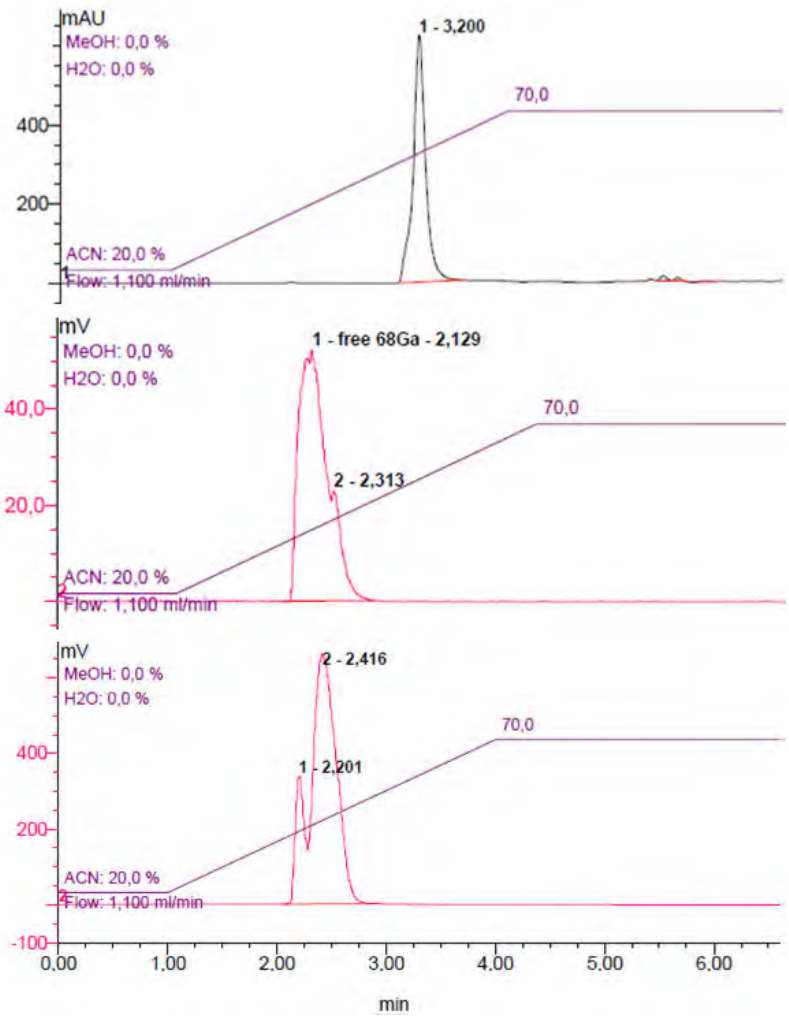

Figure 5.10: **Top**: UV/vis chromatogram of **L5**, Rt = 3.20 ± 0.2 min. **Centre**: radio-UHPLC chromatogram of purified $^{68}Ge/^{68}Ga$ generator eluted [^{68}Ga]$GaCl_3$, Rt = 2.12 ± 0.2 min. **Bottom**: radio-UHPLC chromatogram of the reaction mixture post purification. **Stationary phase**: Phenomenex Luna C18 (4.6 × 250 mm × 5 µm) column. **Gradient mobile phase**: ACN/H_2O (20/80% - 70/30%). **Flow rate**: 1.1 mL/min.

The generator-eluted [^{68}Ga]$GaCl_3$ was purified using a cation ion exchange cartridge (CHROMABOND® PS-H+). In **Figure 5.10** (**middle** chromatogram) The radiodetector chromatogram of [^{68}Ga]$GaCl_3$, after purification, displays a peak with a retention time of 2.12 ± 0.2 minutes assigned to [^{68}Ga]$GaCl_3$. In this chromatogram, there is peak broadening and splitting, possibly as a result of adverse chromatographic parameters (flow rate, stationary phase and mobile phase).

Currently, no work has been reported on the radiolabeling of 2-picolylamine functionalized PPI dendrimers using ^{68}Ga. The radioactive **L5**-^{68}Ga formulation was purified through a Sephadex® G-10 cartridge (molecules of ≤ 700 g/mol are retained within the cartridge). The chromatogram at the bottom in **Figure 5.10** corresponds to the fraction with the highest radioactivity (30.7 MBq) after purification which was eluted from the cartridge using 0.6 M PBS mobile phase. This chromatogram is inconclusive to whether the free [^{68}Ga]$GaCl_3$ is not present or its peak signal overlaps with the signal at 2.41 ± 0.2 minutes. Thus, injection of the crude medium prior to purification might give interpretable results.

Since this is a nascent study, the challenge within this work was to find optimum reaction conditions for a successful radiolabeling of the dendritic ligand **L2** using [^{68}Ga]$GaCl_3$. Labeling parameters like incubation temperature, labeling pH, reaction time duration, starting materials concentration, choice of buffer solutions and UHPLC mobile phase will have to be investigated for optimum labeling efficiency. Ebenhan *et al.*, radiolabeled NOTA conjugated peptides (~10mg/ml) using ^{68}Ga and the radiolabeling method used is partially similar to the current study.[13] Radiolabeling adjustments in the current study are most likely to yield sufficient radiolabeling yields. Alternatively, the labeling of DAB-PPI dendrimers with bifunctional chelators at the periphery (as opposed to *N,N*-chelates in the current study) will have to be investigated as it has been reported in the literature that bi-functional chelators chelate the ^{68}Ga(III) ion with greater affinity and stability.[13,37,38]

5.5. Summary

In the current study, the first generation DAB-PPI dendrimers, with different functionality at the periphery, were radiolabeled with ^{99m}Tc. The direct labeling procedure demonstrated pH dependent radiolabeling of PPI type dendrimers. Among the different options investigated in optimizing labeling conditions, successful labeling of **L5** using the isoLink® kit was obtained.

The 'cold' Re(I) surrogate **C23** was used to elucidate the structure of the *fac*-[^{99m}Tc(CO)$_3$(*N,N*-**L5**)OH$_2$]$^+$ complex, **C23***. The characterization of **C23*** (^{99m}Tc complex) was performed by UHPLC-Gamma detector and the desired complex was found to have a retention time of 6.23 ± 0.2 minutes (comparable to 'cold' Re(I) complex **C23** at 6.23 ± 0.2 minutes). These results attest the similarity in *fac*-[^{99m}Tc(CO)$_3$]$^+$ and *fac*-[Re(CO)$_3$]$^+$ containing complexes. Furthermore, the results show that the *N,N*-2-picolylamine type ligands selectively coordinate to ^{99m}Tc and Re in a similar manner. The major divergences in 'cold' and radioactive *N,N*-bipyridyl complexes were observed with respect to the different retention times of the 'cold' complex **C20** and the radioactive ^{99m}Tc complex(es). This may be attributed to the inadequate labeling reaction time and/or poor solubility of **L2** in aqueous labeling solution. Such findings highlight the difference in experimental conditions for chemical and radiolabeling reactions. The [^{68}Ga]GaCl$_3$ labeling study on **L5** was a challenge and optimum reaction conditions for a successful radiolabeling are required. Labeling parameters like incubation temperature, labeling pH, reaction time duration, starting materials' concentration and choice of buffer solutions will have to be investigated for optimum labeling efficiency. The simple organometallic labeling studies performed accentuate the possibility of labeling higher generation dendrimers of **L5** type with ^{99m}Tc—if purification, prominent labeling yields and purity can be achieved—and test such metallodendrimers as potential diagnostic ^{99m}Tc radiopharmaceuticals.

5.6. Experimental

5.6.1. Materials and methods

5.6.1.1. Direct radiolabeling studies

The solvents used were of high performance liquid chromatography (HPLC) grade and were purchased from Sigma-Aldrich. Analytical reverse phase HPLC was carried out on an Agilent Series 1200 instrument coupled to a diode array UV/vis detector and radiodetector (Gina star, Raytest Gabi Gamma Detector Benzstrasse 4, D-75334 Straubenhard) using Phenomenex Luna C18 column (4 × 250 mm × 5 μm) with a flow rate of 0.5 mL/min. All HPLC procedures isocratic mobile phase system comprised 45% H_2O and 55% acetonitrile (ACN). HPLC-grade water was produced in-house using a Simplicity 185 Millipore system (resistivity = 18.2 MΩcm). Instant thin layer chromatography silica gel (iTLC-SG) was purchased from PALL Life Science. $[^{99m}TcO_4]^-$ was obtained from an in-house generator at South African Nuclear Energy Corporation (Necsa, NTP). The activity was measured in a Scionix 25B25/1.5-E2 gamma counter. All vials were evacuated with argon.

5.6.1.2. isoLink® kit radiolabeling studies

The analytical solvents were purchased from Advanced Biochemical Compounds (ABX) and used as received. The isoLink kit was purchased from Centre of Radiopharmaceutical Research at the Paul Scherrer Institute, Switzerland. The ultrahigh performance liquid chromatography (UHPLC) chromatograms were obtained from a Thermofisher Dionex equipped with a UV/vis spectrophotometer and a Berthold LB509 radioactivity detector using a Phenomenex Luna C18 column 100 Å (4.6 × 250 mm × 5 μm) and a flow rate of 1.1 mL/min. Sep-Pack C18 Light Cartridges (78.6 μm) were obtained from GE Healthcare. The pH test papers were purchased from MACHEREY-NAGEL. Radiolabeling and purification

experiments were performed in a LEMER PAX INNOVATIVE glove box integrated with a dose calibrator. $[^{99m}TcO_4]^-$ used was obtained from a 4 GBq Generator purchased from Cis-Bio IBA.

5.6.1.3. ^{68}Ga radiolabeling studies

The radiolabeling studies were performed in an automated General Electric Medical Systems (Tracelab FX F-N) radiosynthesizer. $[^{68}Ga]GaCl_3$ was eluted from a 1GBq SnO_2-based $^{68}Ge/^{68}Ga$ generator (iThemba LABS, SA) and purified through a CHROMABOND® PS-H^+ cartridge purchased from MACHEREY-NAGEL. The pH test papers were purchased from MACHEREY-NAGEL. The analytical solvents were purchased from Advanced Biochemical Compounds (ABX). The crude dendritic formulation was purified using 0.6 M PBS, as the mobile phase, through a Sephadex® G-10 Medium (55 – 165 μm, 1.3 × 4.0 cm, 5.3 mL) size exclusion cartridge purchased from GE Healthcare. Purification processes were performed in a LEMER PAX INNOVATIVE glove box integrated with a dose calibrator. UHPLC chromatograms were obtained from a Thermofisher Dionex equipped with a UV/vis spectrophotometer and a Berthold LB509 radioactivity detector using a Phenomenex Luna C18 column 100 Å (4.6 × 250 mm × 5 μm) and a flow rate of 1.1 mL/min.

5.6.2. Direct radiolabeling protocol

5.6.2.1. Buffer preparation

The reagents sodium phosphate ($NaHPO_4$) and citric acid were weighed for the preparation of buffer solutions of pH 4.0, 5.5, 6.5 and 7.0. In all preparations, 200 μL of ultrapure water collected at 18.2 MΩcm was used to dissolve the reagents using a vortex.

5.6.2.2. Sample preparation

In a vial, **L5** (1.00 mg, 0.210 µmol) was dissolved in 250 µL ultrapure water (collected at 18.2 MΩcm resistance) to afford a pH 10 solution. The solution was adjusted to pH 4.0 by a 200 µL $NaHPO_4$/citric acid buffer solution.

5.6.2.3. Preparation of the reducing agent

To a vial containing $SnCl_2$ (10.0 mg, 0.0527 mmol), a 100 µL solution of 0.1 M HCl was added. Subsequently, 9.90 mL of ultrapure water was introduced.

5.6.2.4. 'Kit' formulation

The evacuated vial containing the reducing agent was further pipetted with 250 µL solution of **L5** in ultrapure water. Contents were vortexed. Thereafter, 100 µL aliquot of the solution was pipetted into a shielded vial for radiolabeling studies.

5.6.2.5. Radiolabeling of the dendritic formulation

A direct labeling method using sodium pertechnetate ($Na^{99m}TcO_4$) was formulated at varying pH values of the 'kit' formulation. Briefly, 500 µL of $[^{99m}TcO_4]^-$ (22.2 mCi; obtained from an in-house $^{99}Mo/^{99m}Tc$ generator) in saline was added to 100 µL (1.00 mg/mL) of each 'kit' formulation. The resulting solutions were heated at 80.0 °C for 15 minutes and stored in sterile evacuated sealed vials for labeling efficiency studies.

5.6.2.6. Determination of radiochemical labeling efficiency and colloid forming by iTLC-SG

Whatmann paper and Instant Thin-Layer Chromatograpy-silica gel (iTLC-SG)

Radiochemical purity of the radiolabeled material was evaluated using a Whatmann cellulose and iTLC-SG paper strips (dimensions: 1 cm × 10 cm, both stationary phases). Briefly, each crude radioactive formulation (3 – 6 µL) was spotted at the baseline of iTLC

impregnated silica gel paper (iTLC-SG) and Whatmann cellulose strip using an insulin needle (Hamilton). Following 4 – 5 minutes exposure to mobile phase, acetone for Whatmann cellulose strip and saline for iTLC-SG, the strips were immediately dried and. divided into two segments, demarcating the solvent front from the solvent origin. Subsequently, the activity in each segment was measured using a gamma radiation counter (Scionix 25B25/1.5-E2).

5.6.3. Synthesis of *fac*-$[^{99m}Tc(CO)_3OH_2]^+$ core complexes

5.6.3.1. 'Kit' activation

The isoLink® kit was activated according to the protocol packaged with the kit. The activity of the generator-eluted $[^{99m}TcO_4]^-$ used to activate the kits ranged betweem 5.00 – 4.00 GBq.

*5.6.3.2. Radiolabeling of **L2** using the isoLink® kit to afford **C20****

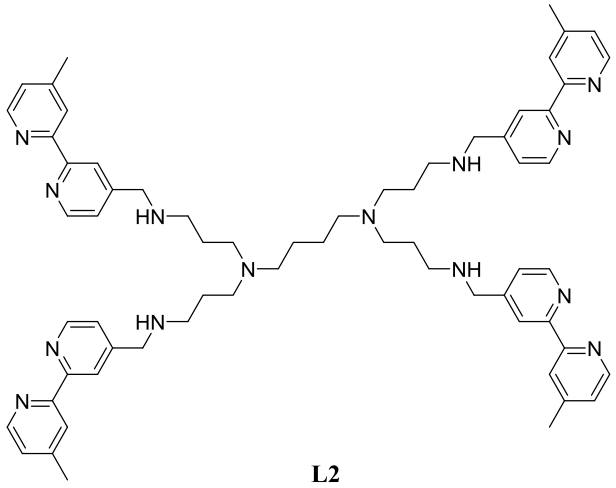

L2

A 100 µL aliquot of $[^{99m}Tc(CO)_3(H_2O)_3]^+$ (858 MBq) was added into a vial containing 224 µL **L2** (0.21 µmol, 1 mg/mL) in acetonitrile and 350 µL of 0.6 N HCl/PBS buffer solution (3:2). The mixture was heated to a 100 °C for 15 minutes where a 20 µL aliquot of the reaction mixture was analysed using UHPLC-Gamma photon detector every 5 minute time interval. The spectra obtained by HPLC have shown that the labelling reaction is achieved

after 15 min. The crude reaction mixture (~500 µL, 108 MBq, pH 6) was then passed through a 3.5 mL short cartridge (Sep-Pack C18 Light Cartridge) where 2 – 3 mL of 100% H_2O, EtOH/H_2O (1:1) and 100% EtOH were used as mobile phase. Following the purification, the fractions collected (0.2 mL per vial) were analysed using a γ-ray detector and those with higher activity (~30 MBq) were further analysed by UHPLC-Gamma photon detector.

C20: Rt = 7.15 ± 0.2 min. **C20*:** Rt = 4.02 ± 0.2 min. **Gradient mobile phase**: acetonitrile/H_2O (50/50% - 80/20%). **Stationary phase**: Phenomenex Luna C18 column (100 Å, 4.6 × 250 mm × 5 µm). **Flow rate:** 1.1 mL/min.

*5.6.3.3. Radiolabeling of **L5** using the isoLink® kit to afford **C23****

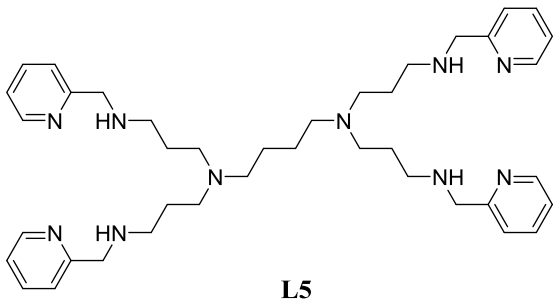

L5

A 100 µL solution of $[^{99m}Tc(CO)_3(H_2O)_3]^+$ (654 MBq) was added into a vial containing 146 µL **L5** (0.21 µmol, 1 mg/mL) in water and 350 µL of 0.6 N HCl/PBS buffer solution (3:2). The mixture was heated to 100 °C for 15 minutes. After 15 minutes, the crude reaction mixture (~500 µL, 210 MBq, pH 6 - 7) was then passed through a 3.5 mL short cartridge (Sep-Pack C18 Light Cartridge) where 2 – 3 mL of 100% H_2O, EtOH/H_2O (1:1) and 100% EtOH were used as the mobile phase. Following the purification, the fractions collected (0.2 mL per vial) were analysed using a γ-ray detector and those with higher activity (>25.5 MBq) were further analysed by UHPLC-Gamma photon detector.

C23: Rt = 6.23 ± 0.2 min. **C23*:** Rt = 6.23 ± 0.2 min. **Gradient mobile phase**: acetonitrile/H_2O (20/80% - 70/30%). **Stationary phase**: Phenomenex Luna C18 column (100 Å, 4.6 × 250 mm × 5 µm). **Flow rate:** 1.1 mL/min.

5.6.4. Preliminary radiolabeling studies on L5 using ^{68}Ga

5.6.4.1. Reagents preparation

L5 (0.21 µmol, 1mg/ml) was dissolved in 1.00 mL solution of 2.5 M sodium acetate buffer to give a final solution of pH 5 – 6. Under acidic conditions, 2.00 – 3.00 mL 0.6 N HCl was used to elute ^{68}Gallium(III)chloride (^{68}Ga) (571.1 MBq) from a SnO_2-based ^{68}Ge/^{68}Ga generator. The initial eluent collected at 1.00 mL 0.6 N HCl was discarded in a waste vial. The [^{68}Ga]$GaCl_3$ solution was passed through a CHROMABOND® PS-H^+ (200 mg. cation exchange cartridge) and ^{68}Ga desorbed using 1.00 mL 0.5 M saline as the mobile phase for pH adjustment and preliminary purification from potentially co-eluted ^{68}Ge.

5.6.4.2. ^{68}Ga radiolabeling procedure

In the automated radiosynthesize, 146 µL **L5** was injected in a reactor containing 1.00 mL [^{68}Ga]$GaCl_3$ (111.4 MBq) in 0.5 M NaCl. The reaction proceeded at room temperature for 20 minutes. An aliquot of the reaction mixture was retained for UHPLC-Gamma ray detector analysis prior to the purification step.

[^{68}Ga]$GaCl_3$: Rt = 2.12 ± 0.2 min. **Gradient mobile phase**: acetonitrile/H_2O (20/80% - 70/30%). **Stationary phase**: Phenomenex Luna C18 column (100 Å, 4.6 × 250 mm × 5 µm). **Flow rate:** 1.1 mL/min.

5.6.4.3. Purification procedure

The crude reaction mixture (104.9 MBq) was passed through a Sephadex® G-10 Medium (55 – 165 μm, 1.3 × 4.0 cm, 5.3 mL) size exclusion cartridge using 0.6 M PBS as the mobile phase. The collected fractions (pH 2, 0.200 mL each) with radioactivity ≤ 20.0 MBq were evaluated for small scale sample purification using UHPLC-Gamma ray detector.

[^{68}Ga]$GaCl_3$ + **L5**: Rt = 2.12 – 2.41 ± 0.2 min. **Gradient mobile phase**: acetonitrile/H_2O (20/80% - 70/30%). **Stationary phase**: Phenomenex Luna C18 column (100 Å, 4.6 × 250 mm × 5 μm). **Flow rate:** 1.1 mL/min.

5.7. References

1. M. Zhao, R. M. Crooks, *J. Am. Chem. Soc.* 1998, **120**, 4877 – 4878.
2. F. Vögtle, S. Gestermann, C. Kauffmann, P. Ceroni, V. Vicinelli, V. Balzani, *J. Am. Chem. Soc.,* 2000, **122**, 10398 – 10404.
3. H. Stephan, H. Spies, B. Johannsen, K. Gloe, M. Gorka, F. Vögtle, *Eur. J. Inorg. Chem.*, 2001, 2957 – 2963.
4. Z. Qiaoa, X. Shi, *Prog. Polym. Sci*., 2015, **44**, 1 – 27.
5. A. Ghai, B. Singh, P. P. Hazari, M. K. Schultz, A. Parmar, P. Kumar, S. Sharma, D. Dhawan, A. Kumar Mishra, *Appl. Radiat. Isotopes,* 2015, **105**, 40 – 46.
6. A. M. Naylor, W. A. Goddard III, G. E. Kiefer, D. A. Tomalia, *J. Am. Chem. Soc.,* 1989, **111**, 2339 – 2341.
7. H. Stephan, H. Spies, B. Johannsen, C. Kauffmann, F. Vögtle, *Org. Lett.*, 2000, **2**, 2343 − 2346.
8. J. F. G. A. Jansen, E. M. E. de Brabander-van den Berg, E. W. Meijer, *Science*, 1994, **266**, 1226 – 1269.
9. G. R. Newkome, B. D. Woosley, E. He, C. N. Moorefield, R. Güther, G. R. Baker, G. H. Escamilla, J. Merrill, H. Luftmann, *Chem. Commun.,* 1996, 2337 – 2338.
10. K. L. Nash, R. E. Barrans, R. Chiarizia, M. L. Dietz, M. P. Jensen, P. G. Rickert, B. A. Moyer, P. V. Bonnesen, J. C. Bryan, R. A. Sachleben, *Solv. Extr. Ion Exch.*, 2000, **18**, 605 – 631.
11. M. C. Parrott, S. R. Benhabbour, C. Saab, J. A. Lemon, S. Parker, J. F. Valliant, A. Adronov, *J. Am. Chem. Soc.,* 2009, **131**, 2906 – 2917.
12. P. J. Blower, *Dalton Trans*., 2015, **44**, 4819 – 4844.
13. T. Ebenhan, N. Chadwick, M. M. Sathekge, P. Govender, T. Govender, H. G. Kruger, B. Marjanovic-Painter, J. R. Zeevaart, *Nucl. Med. Bio.,* 2014, **41**, 390 – 400.

14. D. F. Baban, L. W. Seymour, *Adv. Drug Delivery Rev.,* 1998, **34**, 109 – 119.

15. B. H. Zinselmeyer, S. P. Mackay, A. G. Schatzlein, I. F. Uchegbu, *Pharm. Res.,* 2002, **19**, 960 – 967.

16. N. Malik, R. Wiwattanapatapee, R. Klopsch, K. Lorenz, H. Frey, J. W. Weener, E. W. Meijer, W. Paulus, R. Duncan, *J. Controlled Release*, 2000, **68**, 299 – 302.

17. K. Sadler, J. P. Tam, *J. Biotechnol*., 2002, **90**, 195 – 229.

18. H. B. Agashe, A. K. Babbar, S. Jain, R. K. Sharma, A. K. Mishra, A. Asthana, M. Garg, T. Dutta, N. K. Jain, *Nanomed.:Nanotechnol., Biol. Med*., 2007, **3**, 120 – 127.

19. L. H. Reddy, R. K. Sharma, K. Chuttani, A. K. Mishra, R. R. Murthy, *AAPS J*., 2004, **6**, 1 – 10.

20. N. Arulsudar, N. Subramanian, P. Mishra, R. K. Sharma, R. S. R. Murthy, *J. Drug Target*, 2003, **11**, 187 – 196.

21. V. J. Richardson, K. Jeyasingh, R. F. Jewkes, *Biochem. Soc Trans*., 1977, **5**, 290 – 291.

22. G. B. Saha Jr., *Fundamentals of nuclear pharmacy 4th edition*, Springer-Verlag New York, Inc., USA, 1998, 148 – 172.

23. I. Zolle, *Technetium-99m pharmaceuticals: Preparation and Quality Control in Nuclear Medicine*, Springer, Berlin Heidelberg, 2007, 134 – 204.

24. D. Djoki, D. Jankovi, T. Maksin, *J. Serb. Chem. Soc*., 2002, **67**, 573 – 579.

25. G. J. M. Koper, M. H. P. van Genderen, C. Elissen-Roman, M. W. P. L. Baars, E. W. Meijer, M. Borkovec, *J. Am. Chem. Soc.* 1997, **119**, 6512 – 6521.

26. G. E. Kodina, A. O. Malysheva, O. E. Klement'eva, A. A. Inkin, N. I. Gorshkov, A. A. Lumpov, D. N. Suglobov, *J. Nucl. Radiochem. Sci.,* 2005, **6**, 183 – 185.

27. M. R. Tassano, P. F. Audicio, J. P. Gambini, M. Fernandez, J. P. Damian, M. Moreno, J. A. Chabalgoity, O. Alonso, J. C. Benech, P. Cabral, *Bioorg. Med. Chem. Lett.,* 2011, **21**, 5598 – 5601.

28. A. Badar, J. Williams, R. T. M. de Rosale, R. Tavaré, F. Kampmeier, P. J Blower, G. E. D Mullen, *EJNMMI Research*, 2014, **4**,1 – 8.

29. S. Mundwiler, R. Waibel, B. Springler, S. Kunze, R. Alberto, *Nucl. Med. Bio.*, 2005, **32**, 473 – 484.

30. S. R. Banerjee, M. K. Levadala, N. Lazarova, L. Wei, J. F. Valliant, K. A. Stephenson, J. W. Babich, K. P. Maresca, J. Zubieta, *Inorg. Chem.,* 2002, **41**, 6417 − 6425.

31. T. Ganguly, B. B. Kasten, D. K. Bučar, L. R. Macgillivray, C. E. Berkman, P. D. Benny, *Chem. Commun.,* 2011, **47**, 12846 − 12848.

32. M. Bartholomä, J. Valliant, K. P. Maresca, J. Babich, J. Zubieta, *Chem. Commun*., 2009, 493 − 512.

33. J. Wang, X. Zheng, W. Wu, W. Yang, Y. J. Liu, *Radioanal. Nucl. Chem*., 2014, **300**, 1013 − 1020.

34. M. Sagnou, S. Tzanopoulou, C. P. Raptopoulou, V. Psycharis, H. Braband, R. Alberto, I. C. Pirmettis, M. Papadopoulos, M. Pelecanou, *Eur. J. Inorg. Chem*., 2012, **27**, 4279 – 4286.

35. J. Giglio, G. Patsis, I. Pirmettis, M. Papadopoulos, C. Raptopoulou, M. Pelecanou, E. Leon, M. Gonzalez, H. Cerecetto, A. Rey, *Eur. J. Med. Chem*., 2008, **43**, 741 – 748.

36. L. Fuks, E. Gniazdowska, P. Kozminski, M. Lyczko, J. Mieczkowski, J. Narbutt, *Appl. Radiat. Isot*., 2010, **68**, 90 − 95.

37. C. L. Ferreira, E. Lamsa, M. Woods, Y. Duan, P. Fernando, C. Bensimon, M. Kordos, K. Guenther, P. Jurek, G. E. Kiefer, *Bioconjug. Chem.,* 2010, **21**, 531 – 536.

38. J. Notni, K. Pohle, H.-J Wester, *EJNMMI Res.*, 2012, **2**, 28.

Chapter 6

General Conclusions and Future Work

6.1. Conclusions

The *N,N*-bidentate monomeric and dendritic (DAB-PPI) ligands integrated with 2,2'-bipyridyl and 2-picolylamino entities, **L1 – L6**, were synthesized using a reductive amination reaction. The 2-picolylamino functionalized ligands, **L4 – L6**, were found to be water soluble, $\boldsymbol{S_{25\,^{\circ}C}}$ = 0.01 mg/µL.

Subsequently, Re(I) complexes were synthesized from three Re(I) precursors $Re(CO)_5Cl$, *fac*-$(Et_4N)_2[Re(CO)_3Br_3]$ and *fac*-$[Re(CO)_3(OH_2)_3]^+$ to afford complexes **C7-C24**. Several complexes were characterized using spectroscopic and analytical methods. The molecular structure of **C16**, a Re(I) *bromo*- complex, was further confirmed by X-ray diffraction analysis to investigate the mode of bidentate ligands coordination in macromolecular structures of the same family. The XRD structure of **C16** revealed the mode of coordination of CO ligands around the Re(I) centre as being *facial*. Also, the crystal structure confirmed the *pseudo* octahedral conformation, supported by the bite angles of the *N,N*-donor atom chelates.

The dissolution of *fac*-$[Re(CO)_3$(*N,N*-2-picolylamino)$OH_2]^+$ type complexes, **C22, C23** and **C24**, in MeOH to afford *fac*-$[Re(CO)_3$(*N,N*-2-picolylamino)MeOH$]^+$ type complexes, **LM1**, **LM4** and **LM8**, respectively. The Re(I) methanol complexes were investigated in substitution kinetic studies. The incredible reactivity of the MeOH ligand in dendritic Re(I) complexes **LM4** and **LM8** towards nucleophilic substitution by monodentate ligands (Br^-, Py and DMAP) in solution indicate prominent prospects for the '2+1' radiolabeling of these macromolecules. It was observed that the dendrimer labilizing effect did not increase with the ligand generation. Therefore, the DAB-PPI dendrimer architecture does influence the rate of

MeOH substitution; however, to a certain extent, in spite of the metals being substantially removed from each other *via* the dendritic branches.

In the preliminary radiolabeling studies, the first generation dendritic ligands **L2** and **L5** were tested for their regioselective radiolabeling ability with ^{99m}Tc in aqueous media. The direct labeling studies of **L5** using $[^{99m}TcO_4]^-$ accentuated the feasibility of chelating ^{99m}Tc with *N,N*-donor atoms present in macromolecular structures, a confirmed by labeling efficiency analysis using iTLC-SG and Whatmann cellulose strips. In this study, pH and the amount of $SnCl_2$ used may have contributed in the formation of the undesired ^{99m}Tc radiocolloids. Furthermore, the radiolabeling of **L5** with *fac*-$[^{99m}Tc(CO)_3(OH_2)_3]^+$, a *fac*-$[Re(CO)_3(OH_2)_3]^+$ congener, was successfully achieved and the comparison of the chromatographic results corresponding to the 'cold' Re(I) complex **C23** and radioactive ^{99m}Tc analogue **C23*** suggested a similar mode of metal coordination, at the periphery. However, efficient purification of the labeled formulation could not be achieved as a result of similar enhanced lipophilicity of the product(s) and impurities in the mobile phase.

Translatable chromatographic results for the radiolabeling of **L2** with *fac*-$[^{99m}Tc(CO)_3(OH_2)_3]^+$ and **L5** with $[^{68}Ga]GaCl_3$ were not observed, supporting the need to explore different experimental parameters when radiolabeling macromolecular structures (as opposed to chemical reactions), in general.

6.2. Future Work

Since the activation parameters for the complexes **LM4** and **LM8**, in the presence of Py, DMAP and Br^-, at varying temperatures were not investigated, high pressure stopped-flow studies are required in order to investigate the mode of activation of these complexes, as it becomes more obvious whether the rate increases or decreases as the pressure in varied (*i.e.* whether the activation volume $\Delta V^{\ddagger}$ is positive or negative). In addition, investigate the

phenomenon that results in negligible increase of rate constants with increasing generation number (**LM4** to **LM8**). In radiolabeling studies, an effective purification method must be devised in order to determine the labeling yields and purity of *fac*-[^{99m}Tc(CO)$_3$OH$_2$]+ isomer dendritic complexes. If a purification methodology can be achieved, the labeled metallodendrimers can be biologically tested as potential diagnostic ^{99m}Tc radiopharmaceuticals. In **L5** + [^{68}Ga]GaCl$_3$ radiolabeling studies, labeling must be investigated at various pH ranges, temperatures and at high ligand mass.